Range-Doppler Synthetic Aperture Radar Processing at VHF Frequencies

Jasper M. Horrell, B.Sc.(Hons), M.Sc.(Laser Physics)

May 1999

Thesis Presented for the Degree of DOCTOR OF PHILOSOPHY
in the Department of Electrical Engineering
UNIVERSITY OF CAPE TOWN

Abstract

This thesis focuses on the application of range-Doppler processing at VHF frequencies for wide azimuth beam, airborne, stripmap SAR systems with zero Doppler centroid and modest pulse bandwidths relative to the carrier frequency (simulations less than 30 percent). Such a system is the South African SAR (SASAR) VHF sensor. The theory of such SAR operation is addressed. In general, closed form analytical expressions for range compressed, range-Doppler domain signals do not exist. Thus, in this work, extensive use is made of simulation. Using simulated SAR signals with severe range curvature, the regions of applicability of standard range-Doppler processing, when applied without Doppler frequency dependent secondary range compression, are investigated for a range of processing parameters in the frequency range of 100 MHz to 200 MHz. The effects on the range impulse response of centre frequency, target closest approach range and nominal range resolution are investigated, each for a range of processed azimuth resolutions. Information is presented in the form of plots showing the degradation in the range resolution and in the form of tabular results which also include the range peak- and integrated sidelobe levels and the non-linear phase error in the Fourier domain. An extension to range-Doppler processing, suggested to the candidate by Michael Jin, is demonstrated to provide significantly improved performance over the standard range-Doppler processor for signals with severe range curvature. The basic idea of the extended algorithm, first published by Raney and Vachon in 1989 and applied in the context of a narrow beam, squinted SAR, is to make an initial correction to a reference range through a multiplication with a reference function in the 2-D frequency domain. This is followed by a residual range curvature and azimuth focusing operation in the range-Doppler domain. Airborne motion compensation strategies for flight path reconstruction are discussed. In addition, an ERIM-developed approach for efficiently including an azimuth dependence for wide beam motion compensation is discussed in the context of the SASAR system. An overview of the SASAR VHF project, the experience gained, and the encouraging results from the processing of the data from the first radiating flights, is presented. A full Statement of Originality is given.

Contents

List of Figures

List of Tables

List of Acronyms

- 1-D - One-Dimensional
- 2-D - Two-Dimensional
- A/D - Analogue to Digital
- CARABAS - Coherent All RAdio BAnd Sensing (Swedish SAR)
- COMSIG - South African Symposium on Communications and Signal Processing
- CSIR - Council for Scientific and Industrial Research (South Africa)
- DARPA - Advanced Research Projects Agency (USA)
- DC3 - Dakota aircraft
- DFD - German Remote Sensing Data Centre
- DLR - Deutsche Forschungsanstalt für Luft- und Raumfahrt (Germany)
- ERIM - Environmental Research Institute of Michigan (USA)
- ESAR - Experimental SAR (DLR, Germany)
- EUSAR - European Conference on Synthetic Aperture Radar
- FFT - Fast Fourier Transform
- FIR - Finite Impulse Response (filter)
- FM - Frequency Modulation
- G2 - Ground Processor Version 2 (UCT RRSG)
- GPS - Global Positioning System
- HH - Horizontal polarization transmit and receive
- I - In-phase
- IFFT - Inverse Fast Fourier Transform
- IGARSS - International Geoscience and Remote Sensing Symposium

- IMU - Inertial Measurement Unit
- ISL - Integrated Sidelobe Level
- JPL - Jet Propulsion Laboratory (USA)
- NAWC - Naval Air Warfare Centre (USA)
- PC - Personal Computer
- PRF - Pulse Repetition Frequency
- PSL - Peak Sidelobe Level
- PSP - Principle of Stationary Phase
- PRI - Pulse Repetition Interval
- Q - Quadrature
- R-D - Range-Doppler
- Radar - Radio Detection and Ranging
- RRSG - Radar Remote Sensing Group (UCT)
- SAAF - South African Air Force
- SASAR - South African Synthetic Aperture Radar
- SAR - Synthetic Aperture Radar
- SNR - Signal to Noise Ratio
- SRC - Secondary Range Compression
- STC - Sensitivity Time Control
- UCT - University of Cape Town (South Africa)
- VHF - Very High Frequency (low for radar bands)
- VV - Vertical polarization transmit and receive

List of Symbols

- **A** - Vector from origin to start of reference flight track (Section 5.6)
- **B** - Vector from origin to end of reference flight track (Section 5.6)
- B - Bandwidth [Hz] (Section 2.4)
- B_r - Range bandwidth [Hz] (Section 2.3)
- B_{Dop} - Doppler bandwidth [Hz] (Section 2.5)
- B_{Dop_beam} - Full beam Doppler bandwidth [Hz] (Section 2.5.3)
- B_{Dop_proc} - Processed Doppler bandwidth [Hz] (Section 2.5.3)
- $B_{D\_one\_side}$ - One-sided Doppler bandwidth [Hz] (Section 3.3)
- c - Speed of light [m/s] (Section 2.5)
- d - Real antenna dimension [m] (Section 2.15)
- D_{rec} - Data recording rate [bytes/sec] (Section 2.5)
- f - Frequency [Hz] (Section 2.4)
- f_{ad} - A/D sampling frequency [Hz] (Section 2.3)
- f_0 - Carrier frequency [Hz] (Section 2.3)
- f_D - Doppler frequency [Hz] (Section 2.11)
- f_{Dc} - Doppler centroid frequency [Hz] (Section 2.10)
- f_{Dr} - Doppler rate [Hz/s] (Section 2.10)
- f_{prf} - Pulse repetition frequency [Hz] (Section 2.3)
- f_D - Azimuth (Doppler) frequency [Hz] (Section 2.11)
- f_R - Range frequency [Hz] (Section 2.11)
- f_s - Sampling frequency [Hz] (Section 2.4)
- h - Ellipsoidal height [m] (Section 5.6)

- $\overline{h}$ - Average height above terrain [m] (Section 5.8.1)
- j - $\sqrt{-1}$ (Section 2.5)
- K - Chirp constant [Hz/s] (Section 2.5)
- K_{az_win} - Azimuth window broadening constant (Section 2.6)
- K_{eff} - Effective chirp constant after SRC adjustment [Hz/s] (Section 2.10)
- K_{r_win} - Range window broadening constant (Section 2.6)
- L - Synthetic aperture length [m] (Figure 2.3)
- $n_{az\_samples}$ - Number of azimuth samples (Section 3.3)
- N_{FFT} - Number of complex points used in FFT (Section 2.12.3)
- $N_{r\_samples}$ - Number of range samples (Section 2.5)
- p - Baseband pulse modulation (Section 5.4.2)
- $\mathbf{P}$ - Vector from origin to start of the ground reference track (Section 5.6)
- $\mathbf{R}$ - Vector from start of reference flight track to start of reference ground track (Section 5.6)
- R - Slant range [m] (Section 2.2)
- R_e - Radius of the Earth [m] (Section 5.4.3)
- R_0 - Slant range at closest approach (zero Doppler range) [m] (Figure 2.3)
- R_{foc} - Nominal focusing range [m] (Section 5.8.1)
- R_{grnd} - Nominal ground range to focus position [m] (Section 5.8.1)
- $R_{\max}$ - Maximum (unambiguous) far swath range [m] (Section 2.14)
- R_p^{actual} - Actual range to the focus position for PRI p [m] (Section 5.8.1)
- R_s - Sample range [m] (Section 3.3)
- s_{bb} - Baseband returned signal (Section 5.4.2)
- s_{rx} - Received waveform (Section 5.4.2)

- s_{tx} - Transmitted waveform (Section 5.4.2)
- t - Time [s] (Section 2.2)
- t_0 - Time at which target at closest approach [s] (Section 2.8)
- t_D - Slow-time (azimuth) [s] (Section 2.8)
- t_R - Fast-time (range) [s] (Section 2.5)
- $\mathbf{V}$ - Vector in direction of nominal flight track (Section 5.6)
- v - Ground speed [m/s] (Section 2.5)
- W - Spectrum amplitude weighting function for sidelobe suppression (Section 2.12)
- W_A - Azimuth subpatch size [m] (Figure 5.4)
- W_R - Range subpatch size [m] (Figure 5.4)
- x - Azimuth [m] (Section 2.2)
- x_1, x_2 - Azimuth distances [m] (Figure 3.1)
- $\overline{x}_{accel}$, $\overline{y}_{accel}$, $\overline{z}_{accel}$ - Average x, y, z accelerations [m/sec^2] (Section 5.8.1)
- x_{foc}, y_{foc}, z_{foc} - Focusing position in the swath [m] (Section 5.8.1)
- x_p^{accel}, y_p^{accel}, z_p^{accel} - x, y, z accelerations for PRI p [m/sec^2] (Section 5.8.1)
- α - Angle in azimuth beam [rad] (Figure 2.3)
- β - Angle in azimuth beam [rad] (Figure 2.3)
- δ - Subpatch angle [rad] (Figure 5.4)
- δr_{res} - Range resolution [m] (Section 2.6)
- δr_{grnd_res} - Ground range resolution [m] (Section 2.7)
- δx_{res} - Azimuth resolution [m] (Section 2.6)
- Δh - Height error [m] (Section 5.4.3)
- Δr_{sample} - Slant range sample spacing [m] (Section 2.5)

- Δr_{grnd_sample} - Ground range sample spacing [m] (Section 2.7)
- ΔR - Motion compensation range correction [m] (Section 5.4)
- ΔR_{curv} - Range curvature [m] (Section 2.9)
- $\Delta t_{D\_one\_side}$ - Slow-time (azimuth) extent [s] (Section 3.3)
- Δx_{sample} - Azimuth sample spacing [m] (Section 2.5)
- $\Delta\varphi$ - Motion compensation phase correction [rad] (Section 5.4)
- $\Delta\varphi_e$ - Residual motion compensation phase error [rad] (Section 5.5)
- θ - Look angle [rad] (Figure 5.5)
- $\theta_{3\text{dB}}$ - 3 dB beamwidth [rad] (Section 2.15)
- $\theta_{4\text{dB}}$ - 4 dB beamwidth [rad] (Section 2.15)
- θ_i - Angle of incidence [rad] (Figure 2.4)
- λ - Wavelength [m] (Section 2.5.3)
- τ_p - Pulse length [sec] (Section 2.5)
- ϕ - Half processed azimuth beamwidth [rad] (Figure 2.3)
- φ - Target phase [rad] (Section 2.8)
- ψ - Latitude [rad] (Section 5.6)
- η - Longitude [rad] (Section 5.6)
- ω - Angular frequency [rad/s] (Section 2.2)

Acknowledgements

The candidate would like to express his sincere thanks to his thesis supervisor, Prof. Mike Inggs, for all his guidance and support throughout this work. In addition, the contribution of the late Rolf Lengenfelder for his radar simulation software development, prompted largely by this work, cannot be underestimated and the candidate is fortunate to have had the chance to thank him. The candidate would also like to thank all his colleagues at the UCT Radar Remote Sensing Group, especially Andrew Wilkinson for many informative discussions on a wide range of theoretical issues, and Richard Lord for his interference suppression work. In addition, the candidate would like to thank Alberto Moreira, Richard Bamler, both of DLR, and Michael Jin, of Raytheon (formerly of JPL), for fruitful discussions on aspects of this work. Finally, the candidate thanks Ralf Horn and Stefan Buckreuss of the DLR for supplying the ESAR raw data which prompted the candidate's interest in SAR processing.

Chapter 1

Introduction

Synthetic Aperture Radar (SAR) is a technique (known for nearly 50 years - Wiley [68]) for the mapping of terrain which has several advantages over optical / infrared imaging techniques. SAR is an active microwave technique which allows the possibility of obtaining high resolution imagery from airborne and spaceborne platforms at night, through haze, cloud and rain.

For side-looking real aperture radars, the smaller the azimuth beamwidth, the finer the azimuth resolution (in the direction of the flight track). To achieve a given azimuth resolution for such systems requires a much larger (and thus impractical) antenna at low frequencies than at high frequencies. However, SAR allows the possibility of using longer wavelengths and still achieving good resolution with antenna structures of reasonable size. In addition, for SAR the azimuth resolution can be made independent of range, which is not the case for real aperture radars.

SAR has been shown to be very useful over a wide range of applications: ice monitoring (Drinkwater *et al.* [21]); the detection of earth crustal movement (Zebker and Rosen [69]); geology and mining (Lynne and Taylor [44], Evans [25]); military surveillance; vegetation discrimination (Evans *et al.* [26]); hydrology (McCauley *et al.* [46]); urban mapping; fishing; oil pollution monitoring (Hovland *et al.* [37]); oceanography (Wahl and Skoelv [66]); to name a few.

Many organizations throughout the world have been quick to realize the potential for SAR in a diverse range of applications. This has led to the development of a number of spaceborne and airborne SAR systems. A recent review of SAR sensors, both airborne and spaceborne, is provided by Raney [32] (pp. 98-106). A more dated review is provided by Way and Smith [67].

While many early SAR systems made use of a single frequency band and polarization, there has been a realization that extra information may be obtained from the use of multiple frequencies and multiple polarizations. In particular, there has been a recent trend to add lower frequency sensors to existing systems. Most early systems used L-band or higher (Way and Smith [67]). Antenna size considerations have no doubt been a major factor in the choice of the higher frequencies used by most SAR systems. The lower frequencies require larger antennas and longer synthetic aperture lengths for a given target closest approach range to achieve a given azimuth resolution (Chapter 2, Equation 2.23). The longer synthetic apertures in turn require careful motion compensation and suffer from more severe range curvature effects.

Low frequencies offer particular advantages with regards to penetration through foliage, and buried targets may even be detected in dry regions (Schaber *et al.* [56], Elachi *et al.* [24], Barlin *et al.* [10]). Classic examples of the ground penetration capability are the 'Radar Rivers' as seen in the SIR-A/B images of the extremely arid Eastern Sahara, showing buried features which are not present in optical imagery of the same area (Schaber *et al.* [57]).

Airborne SAR sensors operating below L-band include:

- the P-band (450 MHz) sensor of the German DLR ESAR (Horn [33])
- the DARPA/ERIM/NAWC P-3 ultra-wideband SAR which operates in the 215 MHz to 900 MHz region (Carrara *et al.* [18])
- the CARABAS II VHF SAR system of the Swedish FOA which operates in the 20 MHz to 90 MHz region (Larsson *et al.* [11], Gustavsson *et al.* [28])
- the Russian iMARK VHF SAR sensor which operates around 120 MHz and is operated by the Moscow Scientific Research Institute of Instrument Engineering and the All-Union Scientific Research Institute of Kosmoaerological Methods
- the South African SASAR VHF sensor which operates with a 12 MHz bandwidth centred around 141 MHz (Inggs [38]).

Early SAR systems made use of optical processing in order to focus the imagery. However, digital processors offer high precision and a high degree of flexibility, and are thus the preferred method today. The new applications of SAR have naturally led to considerable effort internationally in recent years in refining existing digital

SAR processing techniques such as the popular range-Doppler algorithm (Munson and Visentin [49], Bamler [7]) and the development of new techniques such as the chirp scaling algorithm (Raney *et al.* [51]), as well as techniques 'borrowed' from other fields such as the range migration algorithm (Cafforio *et al.* [16]).

For a given azimuth resolution, a low frequency, stripmap SAR requires a larger processed azimuth beamwidth than at higher frequencies (Chapter 2, Equation 2.16). However, an airborne SAR system with large processed azimuth beamwidth suffers from two main difficulties (which do not afflict other SAR systems to the same extent):

1. The range curvature is very severe, especially for systems with high resolution. This can make efficient range curvature correction very difficult for certain processing approaches. For example, the standard range-Doppler processor makes use of the range-Doppler domain for implementation of the range curvature correction (the various domains are defined in Chapter 2, Figure 2.2). However, signals with severe range curvature are dispersed in the range-Doppler domain due to the small time-bandwidth product of portions of the signal away from zero Doppler. The correction required for this effect, known as Doppler frequency dependent secondary range compression (SRC), requires the use of a complicated interpolation scheme in the range-Doppler domain (Bamler [7], Smith [59]) and, as a result, most range-Doppler processors do not have the ability to perform this correction.

2. The motion compensation implementation is complicated by the need to include an azimuth dependence into the correction. This translates into having to apply many different corrections to the same point in the data which is difficult to achieve efficiently. A partial solution to this efficiency problem, developed by researchers at ERIM [18], is discussed in Chapter 5.

1.1 Thesis Objectives

The work presented in this thesis stems largely from the candidate's involvement in the system theoretical- and particularly the signal processing side of the SASAR VHF sensor development. The signal processing for the system has been the candidate's responsibility. Of particular interest to the candidate has been the application of range-Doppler processing at VHF frequencies.

Conventional wisdom holds that alternate processing techniques to the standard range-Doppler approach are essential at VHF frequencies. For example, the range migration approach (Cafforio *et al.* [16], Rocca *et al.* [54]) has been used for the processing of the high resolution P3 ultra-wideband SAR (Carrara *et al.* [18]) and a tomographic technique has been developed for the stepped frequency processing of the very low frequency CARABAS system which uses two omnidirectional antennas for left/right discrimination (Larsson *et al.* [11], Hellsten and Andersson [31]).

However, for signals with severe range curvature, the boundaries of the regions where the standard range-Doppler processor's performance moves from being acceptable to unacceptable for a specific application have not been clear.

The main objectives of this thesis are:

- to explore the region of applicability of the standard range-Doppler processing in the 100 MHz to 200 MHz frequency range (without Doppler frequency dependent SRC). Standard quantitative measures of focusing performance are used.
- to demonstrate the improved range curvature correction capability of an extension to range-Doppler processing, based on an idea first published by Raney and Vachon and applied in the different context of a narrow beam SAR with large squint [52].
- to discuss motion compensation strategies for reconstruction of the flight path and correction of the data for wide beam SAR.
- to add to knowledge of VHF SAR operation through discussion of the SASAR VHF system, signal processing, and through presentation of some of the first results from the system.

In this work, emphasis has been placed on low frequency SAR systems with the following characteristics:

- Wide azimuth beam, airborne, stripmap SAR systems with zero Doppler centroid (or the azimuth beamwidth is large enough so that only the portion of the azimuth signal located symmetrically about zero Doppler is processed - no squint correction is required).
- Modest relative pulse bandwidths (ratio of the pulse bandwidth to the centre frequency) with the maximum relative pulse bandwidth simulated in this thesis less

than 30 percent. For the SASAR VHF system, the maximum pulse bandwidth is 12 MHz, centred on 141 MHz (8.5 percent).

1.2 Thesis Structure

The thesis has the following structure:

- Chapter 2 lays the basis for the work described in the remainder of this thesis with the focus on the mathematics and geometry of low frequency, wide beam, airborne, stripmap SAR, particularly as pertaining to range-Doppler processing.

- Chapter 3 investigates the effects of severe range curvature on range-Doppler SAR processing for systems with centre frequencies in the range of $100 - 200$ MHz. The focus is on airborne, strip-map, side-looking SAR systems without range walk (i.e. imaging geometries with a Doppler centroid of zero). The effects on the focusing of a simulated point target are investigated. The main objective of this chapter is to provide an indication to users of range-Doppler processors of the performance which could be expected at VHF frequencies when no Doppler-frequency-dependent SRC is performed. The analysis is analytic as far as tractable mathematics is available, but extensive use of simulated SAR signals has been required. For example, no closed form expressions exist for the range compressed signal in the range-Doppler domain.

- Chapter 4 demonstrates, for signals with severe range curvature, the improved focusing performance of an extended range-Doppler SAR processor over standard range-Doppler processing when performed without Doppler frequency dependent SRC. What makes this work relevant is that it provides a fairly straightforward mechanism for extending the capability of a standard range-Doppler processor to the case of severe range curvature as is typically experienced for high resolution processing at VHF frequencies. In general, the extended processor, as implemented, does require more computation than standard range-Doppler processing. As for Chapter 3, extensive use has been made of simulated SAR signals in evaluating processor focusing performance.

- Chapter 5 presents motion compensation strategies applicable to the wide beam, airborne, stripmap SAR case.

- Chapter 6 presents a short overview of the SASAR VHF project as well as some of the processing results and experience gained from the first flights.

- Chapter 7 gives conclusions and pointers to areas where future work is warranted.

1.3 Statement of Originality

The material presented in this thesis is the candidate's own work. Numerous references are given where material is drawn from others. The candidate's original contributions in each of the remaining major chapters are:

- Chapter 2 (theoretical background) - Although most of the SAR results in this chapter are in no sense novel, the presentation and derivation of many of the equations in this chapter are the candidate's own work and no particular text is followed. References are given where material is drawn from outside sources.

- Chapter 3 (limitations of range-Doppler processing) - All of the material, simulations and processing in this chapter is the candidate's own work. Some of the material appearing in this chapter has been published by the candidate in the Proceedings of EUSAR '98 [34] and COMSIG '98 [36]. In addition, a journal paper, co-authored by Inggs, and detailing some of the results of this chapter, is under preparation (untitled, to be submitted to IEEE Trans. on Aerospace and Electronic Systems).

- Chapter 4 (extension to range-Doppler processing) - The idea for the extended range-Doppler algorithm was suggested to the candidate by Michael Jin in a private discussion [1]. All of the material in this chapter, including the development, coding, simulation and testing of the extended algorithm is the candidate's own work. Some of the material appearing in this chapter has been submitted by the candidate to be published in the Proceedings of IGARSS '99 [35] and a journal paper on the wide beam application of the algorithm, co-authored by Jin, is under preparation (untitled, to be submitted to IEEE Trans. on Aerospace and Electronic Systems). After completion of the extended processor development, the work presented in this chapter, and the submission of the full IGARSS '99 paper [35] (subsequently slightly revised), it was brought to the candidate's attention by Richard Bamler of DLR [2] that an algorithm with the same main

steps had been published by Raney and Vachon [52]. Raney and Vachon, however, while noting that their algorithm would be applicable to the severe range curvature case, applied the approach to the simulation of a narrow beam SAR (3.6 deg) with large squint (45 deg). In addition, the independently developed implementation described here differs from that described in [52]. For example, Raney and Vachon efficiently (but with some approximations) generate the 2-D reference function in the 2-D frequency domain directly from mathematical expressions for the signal from a point scatterer in this domain.

- Chapter 5 (motion compensation) - The work described in this chapter is the candidate's own, and is largely based on the candidate's practical experience in developing and implementing motion compensation algorithms for three systems: the SASAR VHF sensor and the ESAR P-band and C-band sensors. In this chapter, two strategies for reconstruction of the flight path from inertial sensor data are presented: a strategy developed and implemented by the candidate for the processing of the SASAR VHF data; a strategy developed by Buckreuss at the DLR [15] and implemented by the candidate for the processing of the ESAR P- and C-band data. The wide beam motion compensation algorithm discussed in the context of the SASAR system is that developed by Carrara, Tummala and Goodman [18] of ERIM.

- Chapter 6 (SASAR VHF system) - The candidate has been involved with the SASAR system from its inception with a major contribution to the top level system design issues particularly as relating to the SAR processing (including, for example, the choice of operating parameters). In addition, the candidate is responsible for all the SAR processing for the system. With the exception of the interference suppression routines which are the work of Richard Lord, the entire development, coding, implementation, and integration of the SAR processor (with motion compensation) is the candidate's own work (based on the standard range-Doppler algorithm).

Chapter 2

Theory of Wide Beam, Airborne, Stripmap SAR

2.1 Introduction

The theory presented in this chapter supports the main thrust of the work presented in this thesis: range-Doppler processing for wide azimuth beamwidth, airborne VHF signals with zero processed Doppler centroid and with modest relative pulse bandwidths. Discussion of motion compensation, an important element of any airborne SAR system, is deferred to Chapter 5. The theory of spaceborne SAR operation is outside the scope of this work and is not addressed. There are a number of excellent texts and scientific papers covering SAR theory, some of which are referenced in this chapter. For this reason and to maintain the thesis focus, a detailed study of SAR theory and the many different processing techniques and approaches to understanding are not given here. Neither is this chapter intended as an introduction to stripmap SAR for those new to the subject.

A recent, comprehensive technical perspective on SAR fundamentals is provided by Raney [32] (pp. 9-130). Oliver and Quegan provide a theoretical basis for understanding SAR images [50]. Curlander and McDonough [20] provide a comprehensive treatment of SAR systems and signal processing with emphasis on spaceborne systems. Bamler [7] provides an excellent mathematical comparison of several SAR processing algorithms. Ausherman *et al.* [5] describe the signal processing for various SAR imaging modes. Carrara, Goodman and Majewski [17] discuss SAR signal processing algorithms with emphasis on spotlight SAR (no range-Doppler processor treatment).

Other advanced treatments on basic SAR theory are offered by Kirk [40], Sack *et al.* [55], Munson and Visentin [49] and Vant [65]. An earlier text containing a good coverage of basic SAR theory and comparisons with other radar imaging techniques (such as real aperture radar) is given by Ulaby *et al.* [64]. Stimson [61] provides an intuitive introduction to basic SAR theory. Other texts with a treatment of SAR theory are offered by Elachi [22][23] and Skolnik [58].

Although the presentation and derivation of many of the equations in this chapter are the candidate's own work, most of the SAR results presented in this chapter are in no sense novel and references are given where material is drawn from outside sources.

In the sections below, the basic theory and geometry behind low frequency, wide azimuth beam, airborne, stripmap SAR are presented with special emphasis placed on range-Doppler processing. SAR resolution expressions applicable to the wide beam case are derived from bandwidth considerations without making small angle approximations. The equations governing the hyperbolic range- and phase relationships are derived directly from the side-looking geometry. An expression for the range compressed signal from a point target in the range-Doppler domain is presented. The operation of a standard range-Doppler processor is presented. Multilook, ground range projection and unambiguous range are also briefly discussed. In the SAR literature, the equations for azimuth resolution often involve implicit small angle approximations. To conclude and for completeness, the small angle approximations for azimuth resolution and range curvature are derived.

2.2 Assumptions and Notation

The terms "range" and "azimuth" are used extensively in SAR literature and in this thesis. Azimuth distance (denoted by x, Figure 2.1) is as measured along the flight path and range (denoted by R, Figure 2.1) is the straight line distance from the radar antenna to a scatterer. It is important to note that, in general, range and azimuth are not measured in orthogonal directions. This non-orthogonality occurs for any stationary scatterer not at zero Doppler with respect to the strip-mapping radar.

In this thesis, it is useful to be able to refer to the SAR data at various points in the processing chain. The domains referred to in this thesis are defined in Figure 2.2. In this figure and thesis, FFT refers to a (Fast) Fourier Transform.

The following assumptions are applicable to the theoretical results in this chapter:

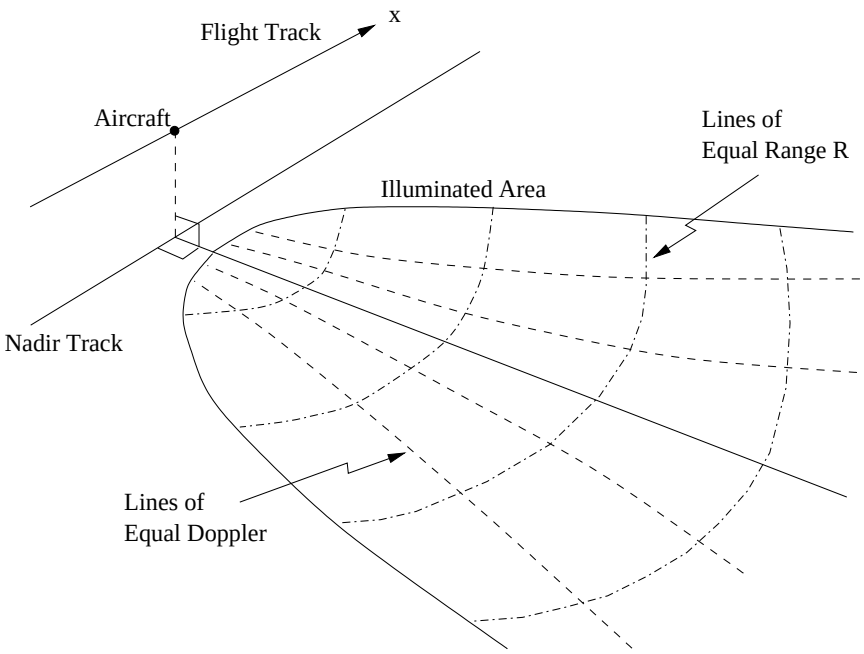

Figure 2.1: The imaging geometry for a wide beam, airborne stripmap SAR.

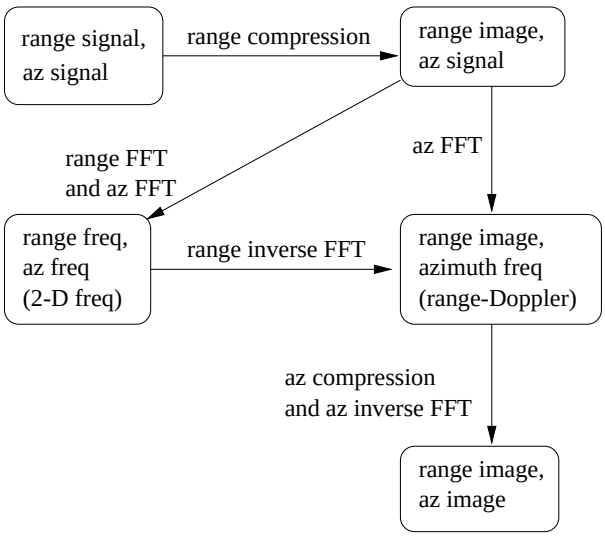

Figure 2.2: The domain definitions for various stages of the signal processing.

- Airborne, strip-mapping SAR with flat earth approximation used.
- Perfect motion compensation (i.e. either the flight path is straight and requires no correction or the correction is assumed to have been performed perfectly for every point in the data).
- Modest relative pulse bandwidths (i.e. not wide-band systems). "Relative pulse bandwidth" is used here as the ratio of the pulse bandwidth to the centre frequency. The relative pulse bandwidths used in this thesis are less than 30 percent.
- Stop-start approximation valid (Barber [9]).
- Stationary scatterers with uniform amplitude and phase response over azimuth angles of interest (Axelsson [6]).
- Azimuth beamwidth sufficiently wide that only the portion of the signal centred symmetrically about zero Doppler is processed in azimuth (i.e. no squint correction required, as discussed in the sections below).
- No small angle approximations have been used unless explicitly stated (see Section 2.15 for small angle approximation expressions)

Throughout this chapter, the widely used convention of representing time domain signals with lower case letters and frequency domain signals with upper case letters is adopted. Thus, if $f(t)$ is a time domain signal, the Fourier Transform of $f(t)$ is denoted by $F(\omega)$. For brevity, the explanation of each symbol in this chapter is performed only in the first equation where that particular symbol appears. A list of symbols appears at the start of the thesis along with a list of acronyms.

2.3 Stripmap SAR Basics

The theory presented in this chapter is applicable to the airborne stripmap SAR geometry with the flat earth approximation. Stripmap is a standard mode of SAR operation, widely used by airborne SAR sensors where a strip (swath) to the side of the aircraft is imaged. The strip may be of any practical length.

The ideal side-looking stripmap SAR geometry is shown for a wide beam, airborne system in Figure 2.1. The radar antenna pattern is oriented towards the ground, orthogonal to the flight track and to one side of the aircraft. As the aircraft moves, a

swath is mapped out on the ground by the antenna footprint. The antenna is pointed to one side of the aircraft and not at the nadir track in order to avoid left/right discrimination complications (and poor ground range resolution close to the nadir point). Systems using omnidirectional antennas such as the Swedish CARABAS system (Gustavsson *et al.* [29]), employ two antennas in order to enable left/right discrimination.

As the aircraft moves along its flight path, pulses with bandwidth B_r and centred at some frequency f_0 are transmitted at the pulse repetition frequency (PRF) f_{prf}. In many systems, the returns from each pulse are quadrature demodulated to baseband, sampled at the A/D frequency $f_{ad} > B_r$ satisfying the Nyquist criterion, and stored as I (in-phase) and Q (quadrature) values. The stored IQ values are later processed digitally to form the radar image.

For SAR, coherent radar operation is required and the IQ values contain both magnitude and phase information. The stored data can be thought of as a two-dimensional array of complex values (with the I value as the real part, and the Q value as the imaginary part). Range is in one dimension of the 2-D array with azimuth in the other dimension.

The radar PRF has important implications on the rate at which data must be recorded. If there is no data rate reduction (through prefiltering or presumming, for example) prior to recording, and n bytes are used for each IQ pair, the data rate D_{rec} for recording is given in bytes per second by

$$D_{rec} = n f_{prf} N_{r\_samples} \tag{2.1}$$

where $N_{r\_samples}$ is the number of range samples to be recorded and f_{prf} is in Hertz. For example, with typical values of a PRF of 1 kHz and 4096 complex range samples, each of 2 bytes, the average data rate is of the order of 8 MBytes per second. Thus, it is easy to see why data handling and processing efficiency are so important for SAR systems.

To reduce processing complexity, the aircraft should fly with a constant ground speed along a straight flight track. Achieving this would ensure that the pulses are regularly spaced on the ground and that subsequent range measurements of all scatterers would be phase coherent, thus no motion compensation would be required. In practice with airborne systems, however, atmospheric winds, turbulence and navigational error are always present to some degree. Uncorrected, these motion errors degrade the SAR's imaging performance. To simplify the motion compensation, the

PRF should be slaved to the ground speed to ensure constant sample spacing along the flight track (Ausherman *et al.* [5]).

Modern SAR systems use sampling in both range and azimuth. Thus before proceeding with SAR bandwidth and resolution discussions, the sampling theorem is introduced in the following section.

2.4 Sampling Theorem

For complex IQ demodulated data, the bandpass version of the Nyquist sampling criterion applies (Raney [32] pg. 19). Expressed mathematically, for a complex signal at some centre frequency f_0 and with bandwidth B, to avoid loss of information due to aliasing, the sampling frequency f_s (complex samples) must be such that:

$$f_s > B \tag{2.2}$$

A parallel version of the Nyquist sampling criterion, sometimes known as the "low-pass" version, applies to real signals. In this case, in order to reconstruct accurately a bandlimited, low-pass waveform from samples of the waveform, the sampling frequency f_s (real samples) must be at least twice the signal bandwidth (Raney [32] pg. 19). The bandwidth in this case refers to the range of positive frequency components.

Applying the Shannon sampling theorem to the case of a complex, bandlimited signal $g(t)$ at baseband (Curlander and McDonough [20] pg. 541): if $|G(\omega)| = 0$ for $|f| > \frac{B}{2}$ where $f = \frac{\omega}{2\pi}$ and provided the sampling frequency $f_s > 2\left(\frac{B}{2}\right)$ then the signal $g(t)$ may be exactly reconstructed from its samples as the infinite sum

$$g(t) = \sum_{n=-\infty}^{\infty} g\left(\frac{n}{f_s}\right) \operatorname{sinc}\left[\pi f_s \left(t - \frac{n}{f_s}\right)\right] \tag{2.3}$$

where $\operatorname{sinc}(\alpha) = \frac{\sin(\alpha)}{\alpha}$. The sampling frequency with $f_s = B$ is known as the bandpass Nyquist frequency. Equation 2.3 is also known as Whittaker's interpolation formula for bandlimited functions. Failure to sample the signal above the Nyquist rate results in aliasing of portions of the signal's frequency spectrum.

For a pulsed system such as SAR, the waveforms are not strictly bandlimited, but may still be closely reconstructed from the finite sum of a reasonable number of samples of the signal, provided the samples are taken above the Nyquist rate.

The bandpass version of Equation 2.2 is what is used with complex SAR signals (after IQ demodulation) and, unless otherwise stated, is what is implied in this thesis

when refering to the Nyquist criterion.

It should be noted here that often the final operation of the SAR processor is to perform detection, i.e. the calculation of the magnitude squared of the focused, complex, data. The square law detector operation in the image domain is equivalent to a convolution operation in the Fourier frequency domain, thus spreading the image spectrum (Raney [32] pg. 71). Thus, before the power detection step, the complex data must be upsampled to twice the (complex) Nyquist sampling rate in order to satisfy Nyquist sampling in the detected image.

In the following section, SAR sampling and bandwidth in range and azimuth are discussed.

2.5 SAR Sampling and Bandwidth

2.5.1 Sampling

For modern stripmap SAR systems, sampling in range occurs at the A/D sampling frequency f_{ad} (after complex demodulation). Thus, to satisfy Nyquist, for a transmitted pulse of bandwidth B_r, we require by Equation 2.2

$$f_{ad} > B_r \tag{2.4}$$

The A/D sampling frequency f_{ad} determines the slant range sample spacing according to

$$\Delta r_{sample} = \frac{c}{2f_{ad}} \tag{2.5}$$

where c is the speed of propagation (light).

The azimuth bandwidth is determined by the Doppler bandwidth B_{Dop} and sampling occurs at the PRF f_{prf}. Thus, to satisfy Nyquist, we require by Equation 2.2 that the PRF satisfy

$$f_{prf} > B_{Dop} \tag{2.6}$$

The azimuth sample spacing is determined by the PRF f_{prf} and ground speed v according to

$$\Delta x_{sample} = \frac{v}{f_{prf}} \tag{2.7}$$

2.5.2 Range Bandwidth

The range bandwidth is determined by the bandwidth of the transmitted pulse (where the receive chain is designed with the same bandwidth). For a monochromatic pulse with length τ_p, the 3 dB bandwidth is given approximately by

$$B_r \sim \frac{1}{\tau_p} \tag{2.8}$$

A pulse modulation commonly used in remote sensing SARs is the linear FM chirp (Curlander and McDonough [20] pg. 133), given by

$$s(t_R) = \exp\left[2\pi j\left(f_0 t_R + \frac{K t_R^2}{2}\right)\right] \qquad |t_R| \leq \frac{\tau_p}{2} \tag{2.9}$$

where t_R is fast-time (range time), f_0 is the carrier frequency, τ_p is the pulse length, K is the chirp constant, and $j = \sqrt{-1}$. The advantage of this mode of operation over short pulse operation is that a longer radar pulse may be used (typically several microseconds) and the pulse energy is spread over the longer period, relaxing the requirement for high peak transmit power. A disadvantage is the added complexity of the pulse synthesizer and compressor. The chirp bandwidth for a linear FM pulse is given by

$$B_r = K\tau_p \tag{2.10}$$

Note that, unlike for the case of the monochromatic pulse, the pulse bandwidth for the phase modulated pulse is not solely dependent on the pulse length τ_p, but also involves the chirp constant K.

A parameter of use in this thesis is the time-bandwidth product. For linear FM chirp signals this is given by

$$B_r\tau_p = K\tau_p^2 \tag{2.11}$$

For signals with reasonable time-bandwidth products (> 100, say, and not restricted to linear FM), the concept of "locking together time and frequency" may be applied (Curlander and McDonough [20] pg. 194). In broad terms, this means that a time segment of the waveform has a one-to-one mapping with a frequency portion of the azimuth spectrum. This is a useful concept for range-Doppler processing where operations such as range curvature correction are performed in the azimuth frequency domain.

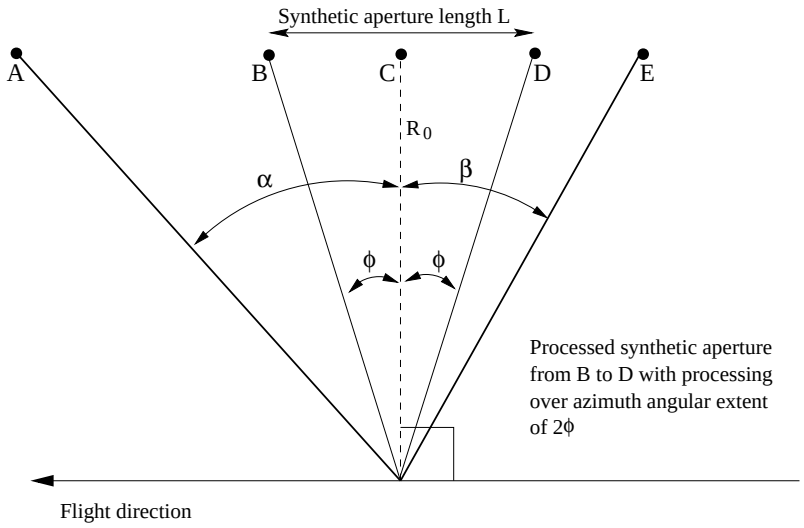

Figure 2.3: The azimuth beamwidth in the slant range direction for a wide beam SAR. Point A is the leading edge of the beam and E the trailing edge. The processed azimuth beamwidth is between B and D with zero Doppler frequency at C.

2.5.3 Azimuth Bandwidth

Figure 2.3 shows the azimuth beamwidth of a wide beam SAR in the slant range direction. As drawn, the beam is squinted forward (angle $\alpha > \beta$). The definition of the azimuth beamwidth, used in this thesis, is as being delineated by the 3 dB points of the one-way antenna power gain in the azimuth slant range projection.

Unless the PRF is chosen to be greater than the Doppler bandwidth of an omnidirectional antenna, some aliasing of the signal will always be present in azimuth which results in azimuth ambiguities in the focused image. This is due to the energy transmitted and received through the sidelobes of the antenna pattern which, in general, experience larger Doppler shifts than the main beam for a side-looking system. A discussion on azimuth- and range ambiguities is given by Curlander and McDonough [20] (pp. 296-305). The discussion given by these authors includes an expression which may be used as a measure of the azimuth ambiguity to signal ratio. The PRF should thus be chosen with care to be sufficient to keep azimuth signal aliasing effects at acceptable levels for the application.

For the work presented in this thesis, the assumption is made that the azimuth beamwidth is sufficiently wide that only a portion of the signal symmetrical about

zero Doppler is required to be processed in azimuth. This has the very important implication that *no correction is required in processing for the beam squint.* This concept is shown in Figure 2.3, where the processed portion of the beam, from B to D, has zero Doppler centroid (at C), even though the Doppler centroid of the actual beam is not zero (unless $\alpha = \beta$).

For the data collection, the range of Doppler frequencies received at the radar is determined by the actual azimuth beamwidth. From Figure 2.3, the spread of Doppler frequencies is given by

$$B_{Dop\_beam} = \frac{2v}{\lambda} (\sin\alpha + \sin\beta) \tag{2.12}$$

where v is the ground speed and λ is the wavelength of the carrier. Thus, to sample above the Nyquist rate, we must have $f_{prf} > B_{Dop\_beam}$. As the definition of the azimuth beamwidth is implicit in this expression, to reduce azimuth aliasing levels, it is prudent to sample at a rate well above B_{Dop_beam}. This is not difficult to achieve in practice for low frequency systems and modest ground speeds (even with large azimuth beamwidths). For example, for a system at 141 MHz, a ground speed of 100 m/s, and with a 180 degree azimuth beamwidth, B_{Dop_beam} is only 188 Hz.

The processed azimuth beamwidth (from B to D in Figure 2.3), centred about zero Doppler and with a beamwidth of 2ϕ, has a corresponding Doppler bandwidth of

$$B_{Dop\_proc} = \frac{4v}{\lambda} \sin\phi \tag{2.13}$$

In this section, expressions for the range and azimuth bandwidths have been presented. In the following section, the resolution in range and azimuth are presented, based on bandwidth considerations.

2.6 Resolution

Resolution is defined in terms of the minimum distance at which two closely spaced scatterers of equal strength may be resolved. In practice, resolution is often measured as the width of a single point target reponse - the impulse response width (Raney [32] pg. 30). If the resolution is measured as the impulse response width at the 3 dB (half power) points, the resolution measurement is consistent with the resolution definition for two point targets of equal magnitude in the focused image, and spaced by the minimum resolvable distance. In this thesis, the resolution measurements results presented refer to the 3 dB impulse response width.

For any system, the best resolution attainable is proportional to the inverse bandwidth (Raney [32] pg. 29). Note that the inverse bandwidth has units of time (for bandwidth with units of inverse time) and so the scaling constants required to obtain the resolution distance must involve units of speed. The resolution is, in addition, proportional to a window constant which is dependent on the type of weighting used to suppress sidelobes during either range or azimuth compression. From Harris [30], for a rectangular weighting, the window constant is 0.89 and for a Hamming weighting (Equation 2.33), the constant is 1.30.

In range, the appropriate scaling constant involves $\frac{c}{2}$ where c is the speed of light. The factor of one half takes the two-way propagation into account. Thus, with a window constant K_{r_win}, the slant range resolution is given by

$$\delta r_{res} = \frac{c}{2B_r} K_{r\_win} \tag{2.14}$$

In azimuth, the approriate scaling factor involves the ground speed v of the radar platform and the azimuth window constant used during processing K_{az_win}. Thus the azimuth resolution is given by

$$\delta x_{res} = \frac{v}{B_{Dop\_proc}} K_{az\_win} \tag{2.15}$$

Equation 2.15 may be rewritten by substituting the expression for the processed Doppler bandwidth from Equation 2.13 as

$$\delta x_{res} = \frac{\lambda}{4 \sin \phi} K_{az\_win} \tag{2.16}$$

Note that the azimuth resolution for a SAR is independent of ground speed and target range and that the best theoretical azimuth resolution (for full processing of a 180 degree azimuth beam) can be easily shown from Equation 2.16 to be $\frac{\lambda}{4}$ (assuming the window constant is unity). There are, however, further constaints limiting resolution, such as the pulse power constraint, the requirement that the measured backscattered signal suffer from no range ambiguities, and the requirement that the target and antenna amplitude and phase response be known over the full 180 degrees (Brown [13]).

From the slant range geometry of Figure 2.3, for a target with closest approach range R_0, the processed synthetic aperture length L of angular extent 2ϕ is given (for a signal with zero Doppler centroid) by

$$L = 2R_0 \tan \phi \tag{2.17}$$

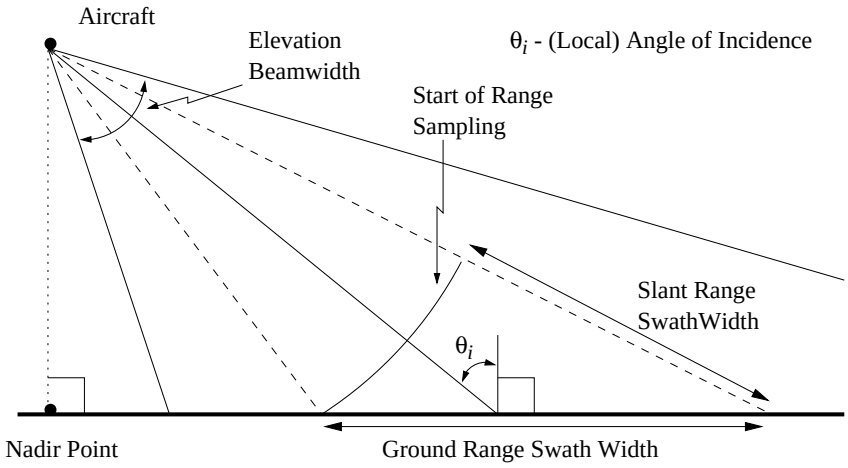

Figure 2.4: The side-looking SAR geometry with the aircraft flying into the page.

In addition, it may be shown from the same geometry that the sine term in Equation 2.16 may be expressed as

$$\sin\phi = \left(\frac{4R_0^2}{L^2} + 1\right)^{-\frac{1}{2}} \tag{2.18}$$

The increase in processed Doppler bandwidth and processed synthetic aperture length required for azimuth multilook is described in Section 2.13.

In the following section, the relationship between ground- and slant range resolution is explored.

2.7 Ground Range Projection

A parameter of greater interest to the user than the slant range resolution is the ground range resolution. A consequence of the strip-mapping geometry is that the ground range resolution is variable across the swath and larger than the constant slant range resolution. The geometry resulting in the relationships between the slant- and ground range is shown in Figure 2.4.

The ground range resolution (for flat terrain) is given by

$$\delta r_{grnd\_res} = \frac{\delta r_{res}}{\sin\theta_i} \tag{2.19}$$

where θ_i is the angle of incidence as depicted in Figure 2.4. Thus, for the near range, where the angles of incidence are smallest, the ground range resolution is poorest, while

the ground- and slant resolutions at the far range are almost identical for large angles of incidence. An identical relationship exists between the slant range sample spacing and the ground range sample spacing:

$$\Delta r_{grnd\_sample} = \frac{c}{2f_{ad}\sin\theta_i} \tag{2.20}$$

Now that the fundamental relationships of SAR operation regarding sampling, bandwidth and resolution have been discussed, aspects pertaining more closely to the specifics of stripmap SAR signal processing are introduced in the sections below. In the following section, the stripmap range and phase variation are considered.

2.8 Hyperbolic Range and Phase Variation

The radar-target range $R(t_D)$ is an important parameter for SAR operation where t_D is slow-time (azimuth time). Using the side-looking imaging geometry, the determination of this parameter is simple for ideal straight flight at constant ground speed v. If the target zero-Doppler range R_0 (closest approach range) occurs at time t_0, then the target range at some time t_D is (by Pythagoras)

$$R(t_D) = \sqrt{R_0^2 + (t_D - t_0)^2 v^2} \tag{2.21}$$

The magnitude of a simulated range compressed, wide beam SAR signal displaying the hyperbolic range variation is shown in Figure 2.5 (Chapter 3, Simulation A).

From Curlander and McDonough [20] (pg. 146), the phase of the received signal is proportional to the radar-target range and is given by

$$\varphi(t_D) = -\frac{4\pi}{\lambda} R(t_D) \tag{2.22}$$

Therefore, since the range relationship with azimuth position is hyperbolic, the phase of the received signal also unwraps according to a hyperbolic relationship with azimuth time.

The hyperbolic range variation leads to the concept of range migration which is discussed in the following section.

2.9 Range Migration

In the literature, there is no consistent use of the terms “range migration”, “range walk”, and “range curvature” (Raney [32] pg. 90). In this thesis, range curvature and

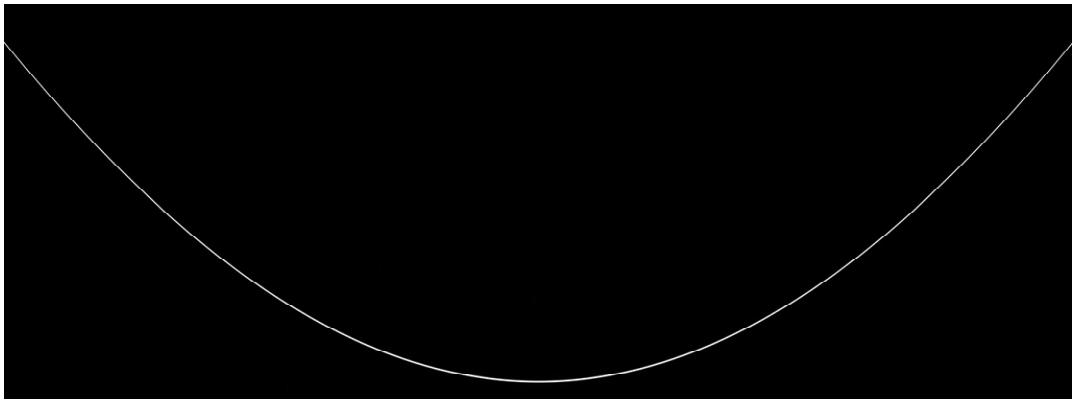

Figure 2.5: The magnitude of a range compressed SAR simulation signal in the slant range image, azimuth signal domain. The slant range resolution is 9.74 m. The full image azimuth extent is 27.979 km (horizontal) and slant range extent is 3.600 km (range increases vertically). The simulation is over a 50 degree azimuth extent for a target at 30 km closest approach range.

range walk, taken together, are termed range migration. Range walk is defined here as the difference in range to a target where it enters and leaves the beam (i.e. the linear component of the range migration). Range curvature is defined here as the non-linear component (i.e. quadratic and higher order components) of the range migration. Range curvature and range walk are shown in Figure 2.6.

For an azimuth symmetrical beam oriented orthogonal to the flight track, the range to a target entering the beam is the same as when the target leaves the beam and there is no range walk. If, however, the beam has a non-zero squint angle, the range walk may become significant. The effect of squint is to change the symmetrical shape of the range hyperbola of Figure 2.5 by extending one arm and shortening the other. For the reason given in Section 2.5.3, range walk correction is not addressed in this thesis.

Range Curvature

The range curvature can be particularly severe for longer wavelengths at a given resolution and target range. This may be shown as follows by considering the relationship between range curvature, resolution and wavelength:

From Equations 2.16 and 2.18, it may be shown for a target at a given zero Doppler range R_0, that the synthetic aperture length L required to achieve a given azimuth

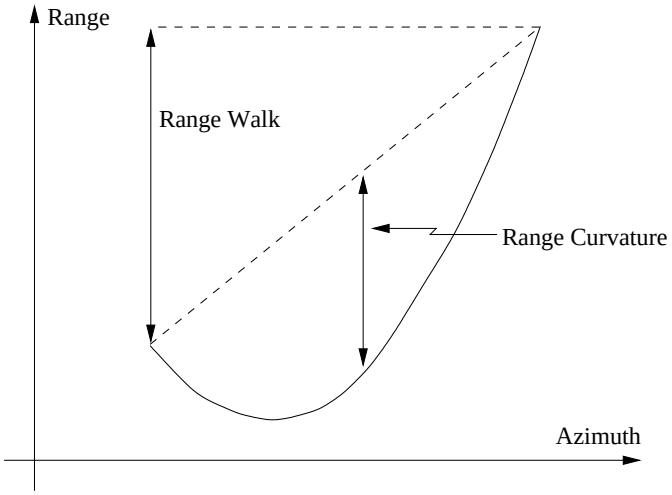

Figure 2.6: Range curvature and range walk (arbitrary units).

resolution δx_{res} increases with wavelength according to

$$L = R_0 \left(\frac{4\delta x_{res}^2}{\lambda^2 K_{az\_win}^2} - \frac{1}{4} \right)^{-\frac{1}{2}} \tag{2.23}$$

Note that this equation involves no small angle approximations and that $\frac{\delta x_{res}}{K_{az\_win}} > \frac{\lambda}{4}$ (from Equation 2.16).

From the side-looking imaging geometry and Equation 2.23, the range curvature at the edge of the synthetic aperture is given by

$$\Delta R_{curv} = \sqrt{R_0^2 + \left(\frac{L}{2}\right)^2} - R_0 \tag{2.24}$$

$$= R_0 \sqrt{1 + \left(\frac{16\delta x_{res}^2}{\lambda^2 K_{az\_win}^2} - 1 \right)^{-1}} - R_0 \tag{2.25}$$

Equation 2.25 gives the desired relationship between range curvature, wavelength, azimuth resolution and closest approach range. A plot using this equation is presented later in this chapter (Figure 2.10).

The discussion on range migration leads on to the concept of secondary range compression.

2.10 Secondary Range Compression

The azimuth Fourier transform through portions of the point target response at constant range with small time-bandwidth products results in the signal being dispersed

(spread out) in the range-Doppler domain. This effect is noticeable for range compressed signals with large range walk or large range curvature. A technique known as secondary range compression (SRC) was developed by Jin and Wu [48] in order to handle cases of severe range walk with narrow beamwidth systems.

For many cases, the parameters used during SRC usually need not be updated with range and, as a result, this process may be combined with the range compression operation without impacting overall processor efficiency. This is useful for pulse compression systems where the pulse compression is performed in software. The SRC is achieved by adjustment of the chirp rate used in the range compression operation according to (Curlander and McDonough [20] pg. 205)

$$K_{eff} = K\left[1 - \left(\frac{K}{f_{Dr}}\right)\left(\frac{\lambda f_{Dc}}{c}\right)^2\right]^{-1} \tag{2.26}$$

where K is the chirp constant of Equation 2.9, f_{Dr} is the Doppler rate, and f_{Dc} is the Doppler centroid. Curlander and McDonough [20] (pg. 205) state that for the technique of adjusting the range chirp constant, rather than updating the SRC parameters with range, to result in less than 10 percent broadening of the impulse response, the proportional change in chirp constant over range is required to be small enough so that

$$\left|\frac{\Delta K}{K}\right|(B_r\tau_p) < 2 \tag{2.27}$$

where the weighting of the (primary) range matched filter (in order to reduce sidelobes) has been taken into account.

The SRC operation may be thought of as a correction for range broadening in the image resulting from the lack of orthogonality between the azimuth and range coordinates for signals with non-zero Doppler (Raney *et al.* [51]). This naturally leads to the requirement of including a Doppler frequency dependent term in the SRC operation rather than applying a blanket correction matched to the Doppler centroid. Doppler frequency dependent SRC is required for signals with severe range curvature. Unfortunately, this cannot be performed efficiently in the standard range-Doppler algorithm (Bamler [7]), but is possible in some other processing algorithms (such as the chirp scaling approach). In Chapter 3, the requirement for Doppler frequency dependent SRC is explored further and in Chapter 4, an extension to standard range-Doppler processing is demonstrated to reduce the requirement for the Doppler frequency dependent SRC.

2.11 Range-Doppler Domain Signal

Before proceeding with a discussion of the range-Doppler algorithm where operations are performed in the range-Doppler domain, it is instructive to examine a mathematical expression for a SAR signal in the range-Doppler domain. Unfortunately, due to the target range migration, a closed form analytic expression for such a signal does not exist (Bamler [8]). In [53], Raney derives an approximate expression for a SAR signal in the range-Doppler domain for the case of large time-bandwidth pulse modulation in range.

In this section, Bamler's approximate expression [8] for a range compressed signal in the range-Doppler domain is presented. Bamler's derivation is based on the same major steps as published by Raney [53]. The symbol definitions used in this section are given by (consistent with any previous definitions):

- t_R, f_R - fast-time (range time) and range frequency (Hz)
- t_D, f_D - slow-time (azimuth time) and azimuth (Doppler) frequency (Hz)
- R - scatterer slant range
- R_0, t_0 - scatterer zero Doppler coordinates (slant range and time at closest approach)
- f_0, λ - carrier frequency (Hz) and corresponding wavelength (m)
- v - ground speed (m/s)
- c - speed of light (m/s).

The starting point is an analytical expression for the range compressed response from a point target after complex demodulation, given by (Bamler [8]):

$$s(t_R, t_D) = k \cdot A_\phi(.) \cdot g\left(t_R - \frac{2}{c}R(t_D)\right) \cdot \exp\left(-j\frac{4\pi}{\lambda}R(t_D)\right) \tag{2.28}$$

where:

- k is a constant which includes the elevation beam pattern
- $A_\phi(.)$ is the scaling effect due to azimuth antenna pattern and due to the radar equation (Skolnik [58] pg. 521).

- $g()$ is the pulse envelope of the range compressed pulse
- $R(t_D) = \sqrt{R_0^2 + v^2 \left(t_D - t_0\right)^2}$ (from Pythagoras)

Using Equation 2.28, the main steps used by Bamler [8] in the derivation of the range-Doppler domain signal are (with additional notes from Bamler [2]):

- Fourier transform in range to the range frequency, azimuth signal domain by making use of the Fourier shift theorem (Bracewell [12] pg. 104).
- Fourier transform in azimuth to the 2-D frequency domain using the Principle of Stationary Phase (PSP) (Raney [53]). PSP is valid for both range compressed and range uncompressed signals). This leads to an equation of the form (where $g(t_R) \leftrightarrow G(f_R)$) given by Equation 2.29.

$$S\left(f_R, f_D\right) = kA_\phi\left(.\right) \cdot G\left(f_R\right) \cdot \exp\left(j2\pi R_0 \left[\frac{f_R + f_0}{c/2} - \sqrt{\left(\frac{f_R + f_0}{c/2}\right)^2 - \left(\frac{f_D}{v}\right)^2}\right]\right) \tag{2.29}$$

- The next step is, for every azimuth frequency, to expand the range frequency dependence f_R of the phase of the complex exponential term of Equation 2.29 in the 2-D frequency domain in a Taylor series $\left(\Phi \approx \Phi_0 + \Phi_1 f_R + \Phi_2 f_R^2\right)$. The zeroth order term Φ_0 is the azimuth compression filter phase. The first order term Φ_1 is a linear phase in range frequency which corresponds to the signal range migration. The second order term Φ_2 corresponds to a range dispersion in the range-Doppler domain (the SRC term).
- Finally, inverse Fourier transform in range to end up in the range-Doppler domain. The zeroth order term transforms to the azimuth frequency dependent phase. The first order term transforms to the range migration in the range-Doppler domain. There is no analytical expression for the transformation of the second order term since PSP cannot be used as the quadratic phase of this term is weak. In Bamler's expression, the effect of the SRC phase term in the range-Doppler domain is accurately presented as a range convolution of the range migration curve with the inverse Fourier transform of a quadratic phase.

Neglecting the constant k, the expression of the signal from a point scatterer in the range-Doppler domain is given by Bamler as [8]

$$S(t_R, f_D) = A_\phi(.) \cdot g\left(t_R - \frac{2}{c}\Delta R(f_D)\right) \cdot \exp\left(j\Phi_0(f_D)\right) \otimes SRC(t_R, f_D) \qquad (2.30)$$

where

- $\otimes$ denotes a fast-time (range time) convolution.
- $R(f_D) = R_0\left(1 - \left(\frac{f_D\lambda}{2v}\right)^2\right)^{-\frac{1}{2}}$ and $\Delta R(f_D) = R(f_D) - R_0$ (the range migration in the range-Doppler domain, derived later as Equation 2.38).
- $\Phi_0(f_D) = \frac{4\pi}{\lambda}R_0\left[1 - \sqrt{1 - \left(\frac{f_D\lambda}{2v}\right)^2}\right]$ (the zeroth order term of the Taylor series phase expansion).
- $SRC(t_R, f_D)$ is the inverse range Fourier transform of the quadratic phase term $\exp\left(j\Phi_2(f_D) \cdot f_R^2\right)$.
- $\Phi_2(f_D) = \frac{2\pi\lambda}{c^2}R(f_D)\left[\left(\frac{R(f_D)}{R_0}\right)^2 - 1\right]$ (the second order term of the Taylor series phase expansion).

Equation 2.30 is the desired expression for the range-Doppler domain signal. The range convolution of the SRC term with the range migration curve causes a dispersion of the range-Doppler domain signal. In the analysis presented, the dispersion is seen as being in the range direction (an alternate and consistent viewpoint).

As there is no closed form analytical expression of Equation 2.30, numerical evaluation would be required on a case by case basis. For this reason, use has been made in this thesis of simulated SAR signals in the investigation of the range curvature limitations of standard range-Doppler processing (Chapter 3) and in the demonstration of the extended algorithm (Chapter 4).

In the preceding sections, theoretical issues relating to SAR operation and the form of the SAR signal have been discussed. Now that the collection geometry and form of the SAR signal has been addressed, it is appropriate to discuss range-Doppler image formation processing in the following section.

2.12 Range-Doppler Processing

The basic idea behind standard range-Doppler processing is simple: manipulate the data such that use may be made of one-dimensional convolution operations with one-

dimensional range and azimuth matched filters (also known as the range and azimuth reference functions) in order to focus the image.

For efficiency, both the range and azimuth convolutions are performed through a multiplication in the Fourier frequency domain. Expressed mathematically, for some complex signal $s(t)$, the matched filter $m(t)$ is given by

$$m(t) = s^*(-t) \tag{2.31}$$

(where the * denotes the complex conjugate) and the convolution operation (denoted $\otimes$) of $s(t)$ with $m(t)$ is achieved in the Fourier frequency domain as

$$s(t) \otimes m(t) \Longleftrightarrow S(\omega) \cdot M(\omega) \tag{2.32}$$

Often, a spectrum amplitude weighting $W(\omega)$ is applied for sidelobe suppression. Two amplitude weightings were used in this thesis (for the range and azimuth reference functions). These were the rectangular window and the Hamming window. The Hamming window, a special case of the Hanning window, is given in the discrete case by (Harris [30])

$$W(i) = 0.54 - 0.46\cos\left(\frac{2\pi i}{N-1}\right) \tag{2.33}$$

$$= 0.08 + 0.92\sin^2\left(\frac{\pi i}{N-1}\right) \tag{2.34}$$

where N is the total number of points spanning the weighted region ($i = 0, 1, ..., N-1$). As mentioned in Section 2.6, the use of an amplitude weighting to reduce sidelobes does result in some broadening of the main lobe and hence loss of geometric resolution. Harris [30] gives the peak sidelobe levels (PSL) and broadening factors for a range of windows. For a rectangular window, the PSL is -13 dB and for a Hamming window, the PSL is -42 dB. The broadening factors for these two windows are 0.89 and 1.30, respectively.

In Chapters 3 and 4, range compression was applied in the simulator, prior to the A/D. A Hamming weighting was used, but applied to the signal domain reference function (rather than to the spectrum). Due to the time-frequency locking of the large time-bandwidth product linear FM chirps used, this approach is equivalent to applying the Hamming window in the frequency domain and the broadening factor remains 1.30 with a PSL of -42 dB.

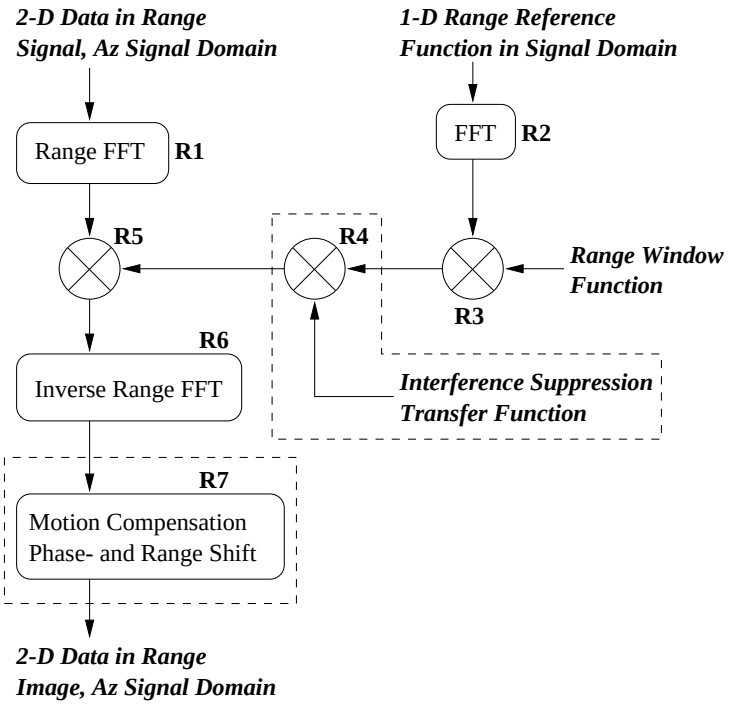

Figure 2.7: The range compression stage of the range-Doppler processor. Steps R4 and R7 do not form part of the core range compression stage, but were required for the SASAR processing.

2.12.1 Range Compression

The main functionality of the range compression stage of the range-Doppler processor used as the "standard" processor in this thesis (including the SASAR images of Chapter 6), is shown in Figure 2.7.

The range reference function is simply implemented as the time-reversed, complex conjugate of the transmitted pulse (Equation 2.31). A commonly used transmitted pulse modulation for SAR is the linear FM chirp of Equation 2.9. Unlike the azimuth reference function case, the range reference function does not usually require updating.

From Curlander and McDonough [20] (pg. 146), for signals with reasonably large time-bandwidth products (say > 100), the point target response function for a target at range R has a (approximately) rectangular amplitude spectrum and the time response of the range compressed signal is given by

$$g(t_R) = B \exp\left(-j\frac{4\pi R}{\lambda}\right) \operatorname{sinc}\left[\pi B\left(t_R - \frac{2R}{c}\right)\right] \tag{2.35}$$

where λ is the transmitted pulse wavelength (assuming IQ demodulation such that

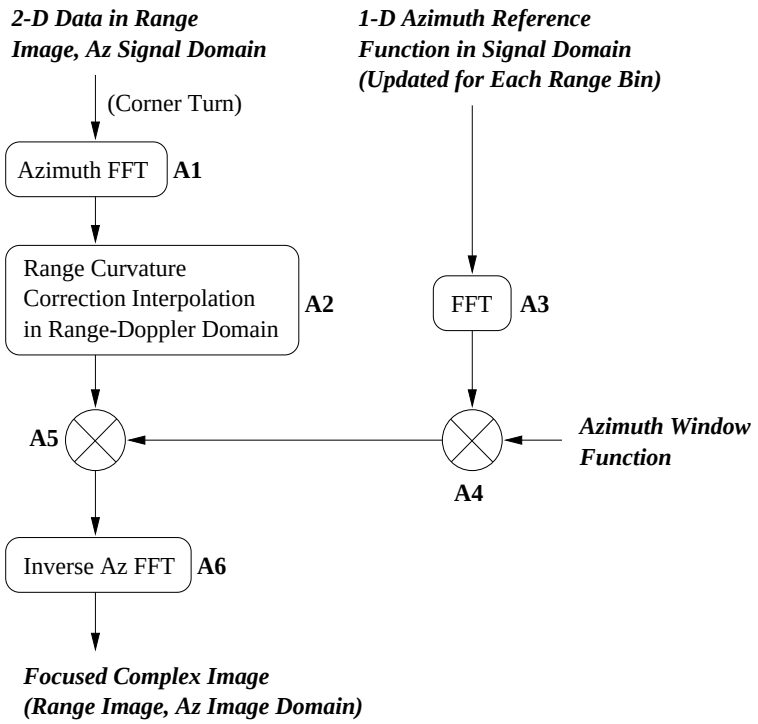

Figure 2.8: The azimuth compression stage of the "standard" range-Doppler processor.

the centre frequency is zero at baseband). Cook and Bernfeld [19] show that, even for linear FM signals with smaller time-bandwidth products ($\tau_p B > 20$), the range compressed signal will still have the $\frac{\sin(\alpha)}{\alpha}$ form, provided the appropriate matched filter is used for the signal. In this case, the resolution result (Equation 2.14) is still valid even though the amplitude spectrum is no longer rectangular.

Equation 2.35 has very important implications for SAR operation. Note how, even though the carrier frequency has been removed from the signal on reception, the phase of the range compressed response (in the argument of the exponential) is dependent on the wavelength of the transmitted signal (and the target range). This phase term is crucial in the SAR azimuth focusing operation discussed below.

2.12.2 Azimuth Compression

The main functionality of the azimuth compression stage of the range-Doppler processor used as the "standard" processor in this thesis (and for the SASAR images of Chapter 6), is shown in Figure 2.8 (Steps A1 - A6). Note that this processor does not implement Doppler frequency dependent secondary range compression (SRC).

The azimuth compression operation is not as simple as for range compression. Due to range migration effects, the signal in azimuth is two-dimensional. In addition, the azimuth matched filter must be updated with range.

For the range-Doppler processing of this thesis, the one-dimensional azimuth reference function multiplied in the azimuth frequency domain with each range curvature straightened azimuth line, was calculated directly from the knowledge of the radar-target hyperbolic range of Equation 2.21 (no approximations used). The length of the azimuth reference function required for each range R_0 was calculated from Equation 2.17 with the phase calculated as time-reversed, complex conjugate of that given by Equation 2.22. In addition, note that for the results presented in Chapters 3 and 4 the azimuth reference function was updated for every range bin.

2.12.3 Range Curvature Correction

Range migration correction is required for accurate SAR processing. The need to perform this correction acurately in an efficient manner has been an important consideration leading to the development of a number of SAR processing algorithms, including the chirp scaling (Raney *et al.* [51]) and the range migration algorithm (Cafforio *et al.* [16]). The range-Doppler algorithm approach for the range curvature correction in the range-Doppler domain is discussed in the sections below.

As discussed in Section 2.10, for SAR systems with severe range curvature (e.g. the wide azimuth beam case), the signal in the range-Doppler domain is dispersed. This results in inaccuracies in the range-Doppler domain range curvature correction, leading to the requirement for Doppler frequency dependent SRC.

"Moderate range curvature" refers here to the case when the range curvature is not so severe that Doppler frequency dependent SRC is required for the application. "Severe range curvature" refers here to the case when Doppler frequency dependent SRC is required for the application. Chapter 3 explores the boundaries of the VHF region where Doppler frequency dependent SRC becomes important.

Moderate Range Curvature Case

Munson and Visentin [49] state that if the total range migration (range walk and range curvature together) exceeds the range resolution, then correction is required. A more stringent criterion is given by Raney [32] (pg. 90) who states that half the range

resolution is acceptable unless highly accurate focusing performance is required.

For range-Doppler processing, range curvature correction is efficiently carried out in the range-Doppler domain as shown by Step A2 in Figure 2.8 (Vant [65], Munson and Visentin [49]). This is possible since the responses from targets at the same range but different azimuth positions map into the same Doppler spectral region. In addition, for signals with sufficiently large time-bandwidth products, the curvature in the range-Doppler domain is isometric to the curvature in the range compressed signal domain (Munson and Visentin [49]). Thus, it is possible to straighten an entire azimuth line at once in the azimuth frequency domain. This has obvious efficiency advantages over a time domain correction where it would be necessary to track the range curvature for each azimuth point. The time domain approach is certainly possible and accurate, but, due to efficiency considerations, is almost never performed in practice for any reasonably sized image.

The range curvature correction in the azimuth frequency domain naturally assumes along track coherence of the signal prior to the azimuth FFT. Thus, motion compensation must be performed before the range curvature correction operation.

The curvature in the range-Doppler domain can be derived from the geometry and Doppler considerations. For an unsquinted beam, the half azimuth beamwidth ϕ may be found from the Doppler frequency f_D (absolute value assumed in this section) at the beam edge using Equation 2.12

$$\phi = \arcsin\left(\frac{\lambda f_D}{2v}\right) \tag{2.36}$$

From considerations of the imaging geometry of Figure 2.3, the range curvature at the edge of the processed beam is given by

$$\Delta R_{curv} = R_0\left(\frac{1}{\cos\phi} - 1\right) \tag{2.37}$$

where R_0 is the target range at closest approach. Thus, combining Equations 2.36 and 2.37, we obtain (after some manipulation)

$$\Delta R_{curv} = R_0\left(1 - \left(\frac{\lambda f_D}{2v}\right)^2\right)^{-\frac{1}{2}} - R_0 \tag{2.38}$$

Now, f_D can be related to the kth point from the zero frequency point in the range-Doppler domain (after the azimuth FFT) according to

$$f_D = k\frac{f_{prf}}{N_{FFT}} \tag{2.39}$$

where N_{FFT} is the number of complex points used in the FFT. Thus, the range curvature correction to be applied in the range-Doppler domain can be expressed as

$$\Delta R_{curv} = R_0 \left(1 - \left(\frac{\lambda k f_{prf}}{2 v N_{FFT}} \right)^2 \right)^{-\frac{1}{2}} - R_0 \tag{2.40}$$

A similar expression is given by Bamler [7]. Note that, this expression has been derived using the Doppler frequency at the edge of the processed beam. However, as any part of the processed beam could equally well have been used in the derivation, Equation 2.40 is thus valid for any Doppler frequency (or frequency point k) within the processed beam.

In practice, accuracy and efficiency considerations dictate the length of the interpolation kernel used for the range curvature correction. For example, for the most accurate correction in the range-Doppler domain, full interpolation (according to Equation 2.3) using many samples should be performed. For efficiency, interpolation is usually only carried out using a 4- or 8-point interpolator. This does result in some loss of accuracy, especially in the complex image (Raney *et al.* [51]). In this thesis, an 8-point Shannon interpolator (Curlander and McDonough [20] pg. 561) was used for both the range curvature correction of the standard range-Doppler processor and for the residual range curvature correction of the extended range-Doppler processor. In addition, note that the curvature correction interpolation was always performed, whether the range curvature exceeded half the range resolution or not.

Severe Range Curvature Case

For the accurate range-Doppler processing of signals with severe range curvature, Doppler frequency dependent SRC is required (discussed further in Chapter 3). However, this is difficult in practice with a range-Doppler processor (Bamler [7]). In Chapter 4, an extension to standard range-Doppler processing is discussed and demonstrated to cater for the severe range curvature case much more accurately than the standard range-Doppler processor.

In the remainder of this chapter, several miscellaneous topics are briefly addressed. These include speckle reduction, the unambiguous range and the SAR-related small angle approximations.

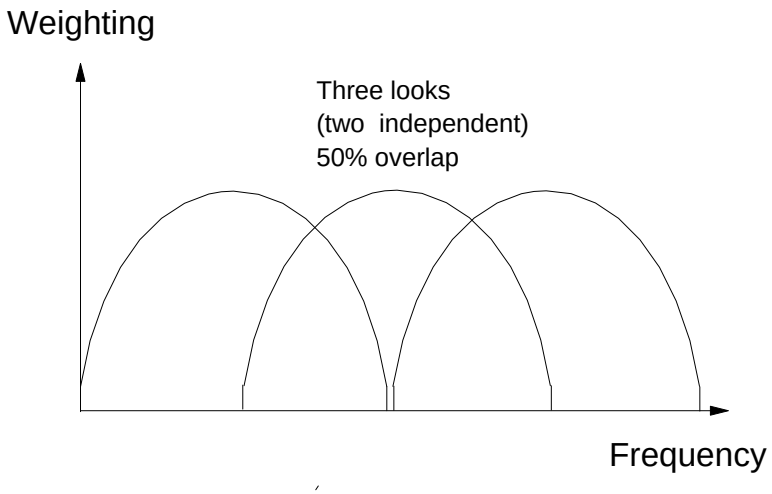

Figure 2.9: Multilook through splitting up of the azimuth frequency spectrum in the range-Doppler domain (immediately before the inverse azimuth FFT).

2.13 Multilook

The preceding expressions in this chapter for the bandwidth, resolution and synthetic aperture length are applicable for single look imagery. In practice in range-Doppler processing, speckle reduction is often implemented by splitting up the azimuth spectrum into "looks" in the range-Doppler domain (as defined in Figure 2.2) and adding the images from each look incoherently (after power detection on each). The weighting of the azimuth spectrum is depicted in Figure 2.9 for 3 overlapping looks (2 independent, non-overlapping).

Where multilook processing is applied in this way, for a given geometric resolution, the total processed Doppler bandwidth must be larger for the multilook case than for the single look case by a factor equal to the number of independent looks. Note that, to avoid misregistration of the looks (with an accompanying degradation of the geometric resolution), coherence is still required over the full synthetic aperture. Thus, motion compensation is required to be accurate over at least the full synthetic aperture length to avoid loss of geometric resolution.

2.14 Unambiguous Range

If the backscattered energy from a particular transmitted pulse arrives back at the radar during the reception period of another pulse, a range ambiguity is said to exist. This is a problem affecting spaceborne SAR systems in particular where several pulses may be in flight at a particular time due to the long slant range to the start of the swath. For such systems, an upper limit on the PRF may be imposed to ensure that no range ambiguities arise from the mainlobe illumination. However, it is still possible to receive ambiguous returns from the antenna sidelobes. If this effect is to be reduced, the upper bound on the PRF must be lowered further.

For airborne SAR systems, range ambiguities are less of a concern as the two-way times for a return from the illuminated swath are generally small in comparison to the pulse repetition intervals (PRIs) used. Typically, only a single pulse is in flight at any particular time and the airborne discussion focuses on the maximum range which may be imaged rather than the maximum unambiguous swath width concept which is applicable for spaceborne systems. For airborne systems, the requirement is that the trailing edge of the backscattered pulse from a point target at the maximum range must be received before transmission of the next pulse. Using this criterion, the maximum range is given by

$$R_{\max} = \frac{c}{2f_{prf}} - \tau_p c \tag{2.41}$$

where the second term in this equation involving the pulse duration is generally small in comparison to the first term and, as a result, may usually be neglected. Note that any backscattered signal interfering with the reception of a successive pulse will in fact originate from ranges greater than $R_{\max}$ as there is, in addition, some dead time between the start of transmission of the successive pulse pulse and the start of sampling.

2.15 Small Angle Approximations

In the equations of the preceding sections, no small angle approximations have been used and it is important to note that *no small angle approximations are used in any of the SAR simulation and processing presented in this thesis.* The processors calculate the full hyperbolic phase and range curvature correction terms for azimuth processing.

In this section, the small angle approximations are included for completeness. This

is useful in that the small angle expressions are common in the literature and, once clearly identified, are less likely to be confused with the exact expressions which should be used for wide beam SAR systems.

2.15.1 Antenna Beamwidth Approximation

For narrow beamwidth antennas where the antenna length d is large relative to the wavelength λ, the 3 dB beamwidth is given by $\frac{k\lambda}{d}$ where k is a constant in the range of approximately 0.9 to 1.3 depending on the current distribution across the aperture (Skolnik [58] pp. 228-235). For example, for a rectangular array, k is 1.2 for a cosine current distribution (with a peak sidelobe ratio of -23 dB). For a uniform current distribution across the aperture (which results in a peak sidelobe ratio of -13 dB), the 3 dB beamwidth (in radians) is given by

$$\theta_{3\text{dB}} \approx 0.88\frac{\lambda}{d} \tag{2.42}$$

Equation 2.42 is often used in a form where measurement of the beamwidth is taken at the -4 dB points and the factor of 0.88 becomes unity for a uniform current distribution. In this case, the beamwidth of the array is

$$\theta_{4\text{dB}} \approx \frac{\lambda}{d} \tag{2.43}$$

Note that Equations 2.42 and 2.43 are only applicable where $d \gg \lambda$ (narrow beam systems).

2.15.2 Azimuth Resolution Approximation

The accurate expression for the azimuth resolution (with zero Doppler centroid) was given in Equation 2.16 as

$$\delta x_{res} = \frac{\lambda}{4\sin\phi}K_{az\_win} \tag{2.44}$$

where ϕ is half the azimuth angle of the processed azimuth extent. If $4R_0^2 \gg L^2$ (small angle approximation), Equation 2.18 reduces to $\sin\phi \approx \frac{L}{2R_0}$ and the azimuth resolution relation of Equation 2.16 becomes

$$\delta x_{res} \approx \frac{\lambda R_0}{2L}K_{az\_win} \tag{2.45}$$

This result is the "standard" SAR resolution approximation relation that appears in much of the SAR literature (usually excluding the window constant K_{az_win}). Now

$L = 2R_0 \tan\phi$ and therefore the SAR resolution approximation result may be written as

$$\delta x_{res} \approx \frac{\lambda}{4\tan\phi} K_{az\_win} \tag{2.46}$$

It is important to stress that Equations 2.45 and 2.46 are only good approximations for small processed azimuth beamwidths. Indeed, a comparison of Equations 2.44 and 2.46 shows that the result of Equation 2.46 is only a good approximation to the azimuth resolution if $\tan\phi \approx \sin\phi$. Note also that the resolution equations apply to power detection (magnitude squared) in the processed image.

For systems with small azimuth beamwidths, combining the results of Equations 2.43 and 2.45 shows that the finest azimuth resolution attainable is approximately given by (with window constant of unity)

$$\delta x_{res} \approx \frac{d}{2} \tag{2.47}$$

2.15.3 Range Curvature Approximation

The accurate expression for the range curvature at the edge of the processed synthetic aperture is given by Equation 2.25 as

$$\Delta R_{curv} = R_0 \sqrt{1 + \left(\frac{16\delta x_{res}^2}{\lambda^2 K_{az\_win}^2} - 1 \right)^{-1}} - R_0 \tag{2.48}$$

For small processed azimuth beamwidths, $\sin^2\phi \ll 1$ and, from Equation 2.44, this implies that $16\delta x_{res}^2 \gg \lambda^2 K_{az\_win}^2$. Thus, in this case, terms in Equation 2.48 may be simplified as

$$\sqrt{1 + \frac{\lambda^2 K_{az\_win}^2}{16\delta x_{res}^2 - \lambda^2 K_{az\_win}^2}} \approx 1 + \frac{1}{2}\left(\frac{\lambda^2 K_{az\_win}^2}{16\delta x_{res}^2} \right) \tag{2.49}$$

and the range curvature may therefore be approximated by

$$\Delta R_{curv} \approx \frac{R_0 \lambda^2 K_{az\_win}^2}{32\delta x_{res}^2} \tag{2.50}$$

Thus, for systems with small processed beamwidths, Equation 2.50 shows that for a given azimuth resolution δx_{res}, the amount of range curvature correction needed increases linearly with range and approximately according to the square of the wavelength. Figure 2.10 shows the range curvature small angle approximation of Equation 2.50 (lower curve) and the exact expression of Equation 2.48 (upper curve) for the region where these expressions differ (high resolution relative to the wavelength).

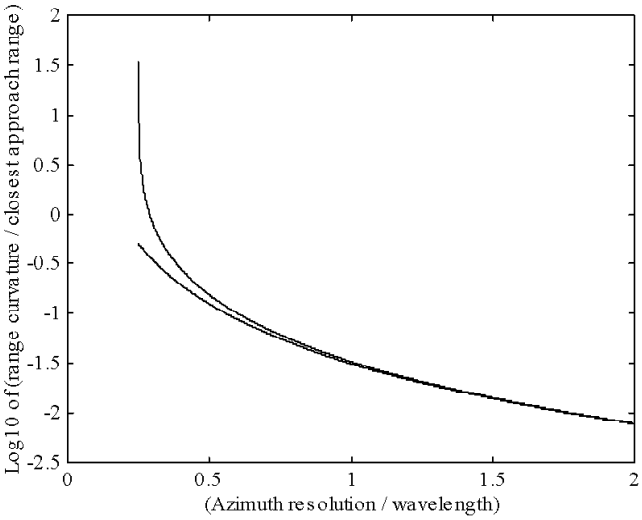

Figure 2.10: Range curvature at edge of synthetic aperture. The upper curve is the exact expression and the lower curve is the small angle approximation. Both axes are dimensionless with the azimuth window broadening constant taken as unity.

2.16 Summary

In this chapter, the basic theory and geometry behind low frequency, wide azimuth beam, airborne, stripmap SAR has been presented with special emphasis placed on range-Doppler processing. SAR resolution expressions applicable to the wide beam case have been derived from the bandwidth definition of resolution. The equations governing the hyperbolic range- and phase relationships have been drived directly from the side-looking geometry. Bamler's expression for the range compressed signal from a point target in the range-Doppler domain has been presented. The operation of a standard range-Doppler processor has been presented. The requirement that Doppler frequency dependent SRC be performed for the severe range curvature case has been noted. Multilook, ground range projection and unambiguous range have also been briefly discussed. To conclude and for completeness, the small angle approximations for azimuth resolution and range curvature have been derived.

In the following chapter, the limits of standard range-Doppler processing without Doppler frequency dependent SRC are explored for the severe range curvature signals which are characteristic of imaging at VHF frequencies.

Chapter 3

Range Curvature Limitation of Range-Doppler Processing

3.1 Introduction

In addition to the popular range-Doppler approach, a number of accurate algorithms for stripmap synthetic aperture radar (SAR) processing have been proposed in recent years. These include the chirp scaling algorithm (Raney *et al.* [51]) and the range migration algorithm (Rocca *et al.* [54], Cafforio *et al.* [16]). Both these techniques make use of the two-dimensional frequency domain, often denoted as the $\omega - k$ domain. The range migration algorithm in particular is well suited to dealing with large range curvature. Although some work has been published on regions of applicability of processing algorithms (Bamler [7], Carrara [17] pp. 473-486), considerably more could be done in this area.

The standard range-Doppler algorithm suffers from a defocusing and distortion of the impulse response in the presence of severe range walk and/or curvature. The limitation is related to the range migration correction in the range-Doppler domain after an azimuth Fourier transform of signals with small time-bandwidth products. This is discussed further in Section 3.3. Jin and Wu [48] introduced the concept of secondary range compression (SRC) in the narrow beam context for handling cases of severe range walk. This may be efficiently implemented for the central image range and for the Doppler centroid frequency through a modification of the range chirp rate during the range compression stage of the algorithm. For imaging geometries with large range walk and small range curvature, the range chirp modification may be sufficient.

However, for the large range curvature case of a wide beam, airborne system, the Doppler frequency dependence of the SRC must be taken into account.

For a side-looking system with zero Doppler centroid, the expression for the azimuth resolution δx_{res} is (Chapter 2.16):

$$\delta x_{res} = \frac{\lambda}{4 \sin \phi} K_{az\_win} \tag{3.1}$$

where λ is the transmitted wavelength, ϕ is half the azimuth integration angle, and K_{az_win} is the azimuth window broadening factor. Thus, from Equation 3.1, it is clear that larger azimuth integration angles are required at lower frequencies than at higher frequencies to achieve a given azimuth resolution.

Following from Equation 3.1, for a strip-map SAR system, the range curvature ΔR_{curv} at the edge of the synthetic aperture is given by (Equation 2.25):

$$\Delta R_{curv} = R_0 \sqrt{1 + \left(\frac{16 \delta x_{res}^2}{\lambda^2 K_{az\_win}^2} - 1 \right)^{-1}} - R_0 \tag{3.2}$$

where R_0 is the target slant range at its zero Doppler position (closest approach position). Equation 3.2 implies that the range curvature is more severe at longer wavelengths than at shorter wavelengths for a given azimuth resolution δx_{res} and closest approach range R_0. Thus, Doppler frequency (and range) dependent SRC requires special consideration for low frequency systems.

For range-Doppler processors, Doppler frequency dependent SRC requires the use of a complicated interpolation scheme in the range-Doppler domain (Bamler [7], Smith [59]). Due to the difficulty in implementing Doppler-frequency-dependent SRC, most range-Doppler processors do not perform this correction.

This chapter investigates the effects of severe range curvature on range-Doppler SAR processing for systems with centre frequencies in the range of $100 - 200$ MHz. The focus is on airborne, strip-map, side-looking SAR systems without range walk (i.e. imaging geometries with a Doppler centroid of zero). The effects on the focusing of a simulated point target are investigated for a range of system and processing parameters. The main objective of the chapter is to explore the performance of standard range-Doppler processing at VHF frequencies when no Doppler-frequency-dependent secondary range compression (SRC) is performed. The contribution of this chapter is the investigation into the boundaries of the region where Doppler frequency dependent SRC becomes important for range-Doppler processing.

All of the material, simulations and processing in this chapter is the candidate's own work. Some of the material appearing in this chapter has been published by the candidate in the Proceedings of EUSAR '98 [34] and COMSIG '98 [36].

3.2 Assumptions

The assumptions and notation used in this chapter are:

- side-looking (Doppler centroid zero), airborne (flat earth geometry), stripmap SAR with perfect motion compensation
- stop-start approximation valid - motion only between pulses (Barber [9])
- centre frequencies in the range $100 - 200$ MHz
- relatively narrow band signals (maximum range chirp 40 MHz) which are range compressed on receive (before A/D)
- adequate sampling in range and azimuth for Nyquist criteria
- stationary point target with uniform amplitude and phase response over azimuth angles (Axelsson [6]) and no antenna weighting effects (targets visible over simulation extent)
- all plots and analysis are slant range rather than ground range and all processing and analysis is for single look imagery

3.3 Range Curvature Geometry

Shown schematically in Figure 3.1 is one half of the region of range-compressed signal support in the slant range image, azimuth signal domain (Figure 2.2) for a side-looking SAR and a point target at a closest approach range R_0. Note that the term "signal support" should, in this context, be taken to mean the region bounded by the 3 dB points of the range-compressed signal. The schematic does not accurately convey the full extent of the range curvature for a wide beam VHF SAR system, but is useful to demonstrate the concept leading to Equations 3.3 and 3.4. A more realistic portrayal of the extent of the range curvature at VHF frequencies is shown by the simulation of the range-compressed VHF signal in Figure 3.3.

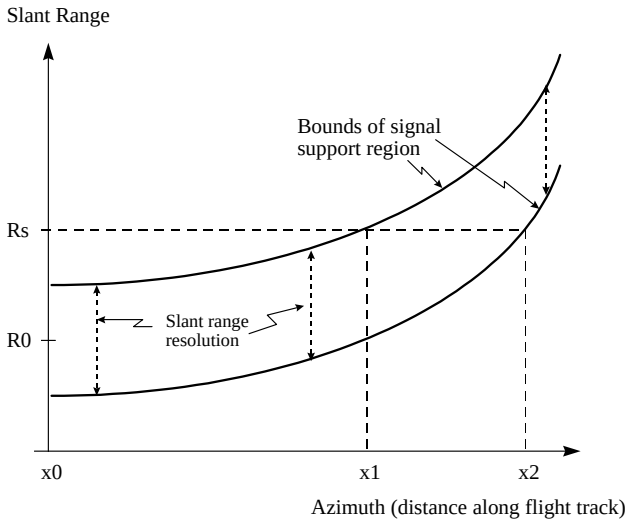

Figure 3.1: Schematic of part of range compressed signal support (slant range image, azimuth signal domain) with slant range vertical and azimuth distance horizontal. The target closest approach range is shown as R_0. A slant range sample at range R_s cuts through a region of range-compressed signal support given by the azimuth distance $(x_2 - x_1)$.

A slant range sample corresponding to a range R_s is shown in Figure 3.1 by the dashed horizontal line. The azimuth positions at which the range sample at range R_s intersects the region of signal support are denoted by x_2 and x_1.

Of interest for the SRC is the time-bandwidth product (TBP) of the signal in azimuth at each range sample. By calculating the Doppler frequency at x_2 and x_1 and subtracting the two frequencies, one obtains an estimate of the Doppler bandwidth for that portion of the signal. Note that this analysis assumes a flat phase across the range peak (between the 3 dB points) of the range compressed signal. This is true at baseband for a properly designed range matched filter (Curlander and McDonough [20] pp. 182-187) and has been observed in the simulations presented later. Effects such as the drop-off in signal power with the fourth power of the target range (as well as antenna effects) are not considered in this mathematical analysis. From the geometry

of Figure 3.1, it is possible to write down expressions for x_2 and x_1:

$$x_2(R_s) = \begin{cases} 0 & \text{if } R_s \leq \left(R_0 - \frac{\delta r_{res}}{2}\right) \\ \\ \sqrt{\left(R_s + \frac{\delta r_{res}}{2}\right)^2 - R_0^2} & \text{otherwise} \end{cases} \tag{3.3}$$

$$x_1(R_s) = \begin{cases} 0 & \text{if } R_s \leq \left(R_0 + \frac{\delta r_{res}}{2}\right) \\ \\ \sqrt{\left(R_s - \frac{\delta r_{res}}{2}\right)^2 - R_0^2} & \text{otherwise} \end{cases} \tag{3.4}$$

where δr_{res} is the slant range resolution (measured between 3dB points) after range compression. The number of azimuth samples of one side of the signal from a single point target for a particular range bin is linearly related to $x_2 - x_1$ and is given by

$$n_{az\_samples} = (x_2 - x_1)\frac{f_{prf}}{v} \tag{3.5}$$

where f_{prf} is the pulse repetition frequency (PRF) and v is the aircraft ground speed.

Considering one side of the symmetric signal hyperbola as depicted in Figure 3.1, it may be shown with some trigonometry that the one-sided Doppler bandwidth is given by

$$B_{D\_one\_side}(R_s) = \frac{2v}{\lambda}\left(\frac{x_2(R_s)}{\sqrt{R_s^2 + x_2^2(R_s)}} - \frac{x_1(R_s)}{\sqrt{R_s^2 + x_1^2(R_s)}}\right) \tag{3.6}$$

where v is the aircraft ground speed and λ is the wavelength of the transmitted signal. The time extent of the one-sided signal for a range sample corresponding to range R_s is simply given by

$$\Delta t_{D\_one\_side}(R_s) = \frac{x_2(R_s) - x_1(R_s)}{v} \tag{3.7}$$

We define the one-sided TBP in this context as the product of the signal Doppler bandwidth (Equation 3.6) and the signal time extent (Equation 3.7).

Figure 3.2 shows log base 10 plots of the one-sided azimuth TBP for three range resolutions, 14.61 m, 9.74 m and 4.87 m, a target with a closest approach R_0 of 30 km and an azimuth beamwidth of 50 deg. These parameters are the same as used in Simulations A, B and C of Table 3.1 in Section 3.4. The maximum one-sided TBP for the three simulations occurs at a sample range of $R_0 + (\delta r_{res}/2)$ and is 27.49, 18.32 and 9.16 for the three simulations (in order of decreasing range resolution). Note that

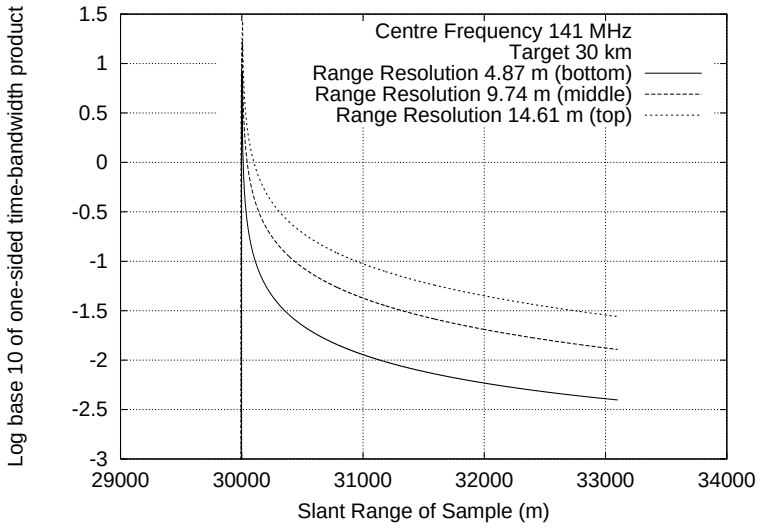

Figure 3.2: Log 10 of the one-sided azimuth time-bandwidth product for three range resolutions versus sample range (Simulations A, B and C).

the maximum values are multiples of 9.16 just as the three resolutions are multiples of 4.87 m.

From Figure 3.2, the severe reduction in TBP with increasing slant range is evident. It is clear that the TBP of signals sampled at ranges much larger than R_0 will be small for systems with similar parameters to those simulated here. Also note that, as expected, the one-sided TBP is smaller for finer range resolution. From basic Fourier theory, a linear FM signal with small TBP will be spread out (dispersed) over a number of frequencies in the Fourier domain (Cook and Bernfeld [19] pp. 136-140). This results in inaccuracies in the range-Doppler processing, notable as a distortion of the range impulse response in the processed image, leading to the requirement for SRC. In the words of Jin and Wu [48]: "This broadening along range is directly related to the spectrum broadening along azimuth which is due to the small time-bandwidth product of the response over constant range." Thus, one would expect the range-Doppler domain signal to be fairly tightly constrained for range samples close to R_0, but to be increasingly dispersed for range samples corresponding to ranges further away.

An approximate expression for the range compressed signal in the range-Doppler domain which includes the dispersion term was given in Chapter 2 (Equation 2.30).

3.4 Simulation Parameters for Focusing Degradation Analysis

As closed form analytical expressions are not available for all the range-Doppler processing stages (notably the range-compressed signal in the range-Doppler domain), the approach taken here has been to investigate the focusing degradation resulting from severe range curvature through a range of simulations. The simulations performed were of low frequency, side-looking, stripmap SAR systems and the effects of centre frequency, range resolution, and target closest approach range were investigated. Although it was not practical to perform an exhaustive set of simulations of all the combinations of system parameters, the results presented may be used as a guideline for certain systems to assist in the decision as to whether Doppler frequency dependent SRC is required for a particular application.

The simulated data were generated using Rolf's Simulator [41], developed at UCT. The simulator models the radar returns from multiple point scatterers. The signal from multiple targets is calculated as the complex superposition of the signals from the individual targets. No multi-path effects are included. The simulation signals are generated at baseband (i.e. after IQ demodulation), but with correct phase for the particular target range and with amplitude according to the radar equation. The stop-start approximation is used in the current simulator version. A wide range of transmitted pulse modulations are possible. Antenna weighting effects are included as well as and target directivity and radar cross section effects.

Output may either be the raw radar return or range-compressed output. For range-compressed output, the range matched filter is calculated as the time-reversed, complex conjugate of the transmitted pulse. For efficiency, this is convolved with the simulated radar return through a multiplication operation in the Fourier frequency domain. Output data may be chosen to be quantized to a specified number of bits.

There is a large degree of flexibility built into the simulator which allows simulation of a wide range of radars from search radars to SARs. For example, multiple moving platforms with user-specified trajectories may be simulated and antenna beams may be set up to be fixed in angle or to rotate.

The simulator has an excellent graphical user interface which allows the user to view the simulation geomerty with coordinate systems and the signals over time. This feature greatly assists in reducing setup time as well as the potential for errors.

The simulator has been well used and tested by a number of researchers over a lengthy period at UCT. Note that the error introduced by the use of the stop-start approximation in the simulator was checked and is completely negligible for the VHF simulations performed.

The SAR processor used in this chapter was the airborne, range-Doppler G2 Processor developed by the candidate at UCT. The G2 Processor was used here as the "standard" range-Doppler processor with basic functionality described in Section 2.12. Note that the G2 Processor does not perform Doppler frequency dependent SRC.

The assumptions and approximations stated in Section 3.2 are applicable here. In addition, the following general simulation and processing parameters were used throughout:

- Hamming window function applied during range compression, rectangular window during azimuth compression. Hamming corresponds to a window broadening factor of 1.30, rectangular corresponds to a window broadening factor of 0.89 [30] (Harris).
- 8-point Shannon interpolation was used during the range curvature correction operation in the range-Doppler domain.
- Azimuth matched filter updated for every range bin processed.
- A/D sampling to 8-bit I and Q was performed after range compression. The simulation data were scaled to ensure full use of the 8-bit dynamic range, while not overflowing.
- Linear FM transmitted pulse with 10 usec duration (rectangular envelope).
- Pulse repetition frequency 250 Hz and aircraft ground speed 250 m/s (hence ground spacing of 1 m in azimuth for pulses).

The discriminating parameters for the simulations performed are listed in Table 3.1. An azimuth simulation extent of 50 degrees implies a simulation over ± 25 degrees. The listed theoretical range resolution δr_{res} is calculated by Equation 2.14 as:

$$\delta r_{res} = \frac{c}{2B_r} K_{r\_win} \tag{3.8}$$

where c is the speed of light ($2.997 \cdot 10^8$ m/s), B_r is the bandwidth of the transmitted pulse, and K_{r_win} is the broadening factor of the window function used during range compression (1.30 for the Hamming window). To assist in reading Table 3.1:

Simulation Identifier	**A**	**B**	**C**	**D**	**E**	**F**
Centre Frequency (MHz)	141.0	141.0	141.0	141.0	100.0	200.0
Azimuth Simulation Extent (deg)	50.0	50.0	50.0	50.0	73.0	35.0
Doppler Bandwidth (Hz)	198.8	198.8	198.8	198.8	198.5	200.7
Target Range Closest Approach (km)	30.0	30.0	30.0	15.0	30.0	30.0
Transmitted Pulse Bandwidth (Hz)	20.00	40.00	13.33	20.00	20.00	20.00
Theoretical Range Resolution (m)	9.74	4.87	14.61	9.74	9.74	9.74
A/D Sample Rate (MHz)	22.00	44.00	14.67	22.00	22.00	22.00
Slant Range Bin Size (m)	6.81	3.41	10.22	6.81	6.81	6.81
Azimuth Samples	27979	27979	27979	13989	44397	18917
Range Samples	528	1057	352	316	1145	264
Maximum Range Curvature (m)	3101	3101	3101	1551	7320	1456
Start Range Sampling (m)	29850	29850	29850	14850	29850	29850
End Range Sampling (m)	33450	33450	33450	17000	37650	31650

Table 3.1: Simulation parameters

- simulations A, E, and F were used to evaluate the effect of centre frequency
- simulations A, B, and C were used to evaluate the effect of pulse bandwidth (hence nominal range resolution)
- simulations A and D were used to evaluate the effect of target closest approach range

Figure 3.3 shows, for Simulation A of Table 3.1, the magnitude of the range compressed SAR simulation signal in the slant range image, azimuth signal domain. Note the severe range curvature (corresponding to 318 slant range resolution cells).

Figure 3.4 shows, for Simulation A, the magnitude of the simulated point target response in the range-Doppler domain. Note that zero Doppler is displayed at the centre of the horizontal coordinate. The dispersion at Doppler frequencies away from zero is clearly visible, leading to the requirement for secondary range compression.

Figure 3.5 shows, for Simulation A, the magnitude of the simulated signal in the range-Doppler domain after the range curvature correction operation by the G2 processor. An 8-point Shannon interpolation was used during the range-Doppler domain range curvature correction operation. The dispersion at Doppler frequencies away from zero is still clearly visible.

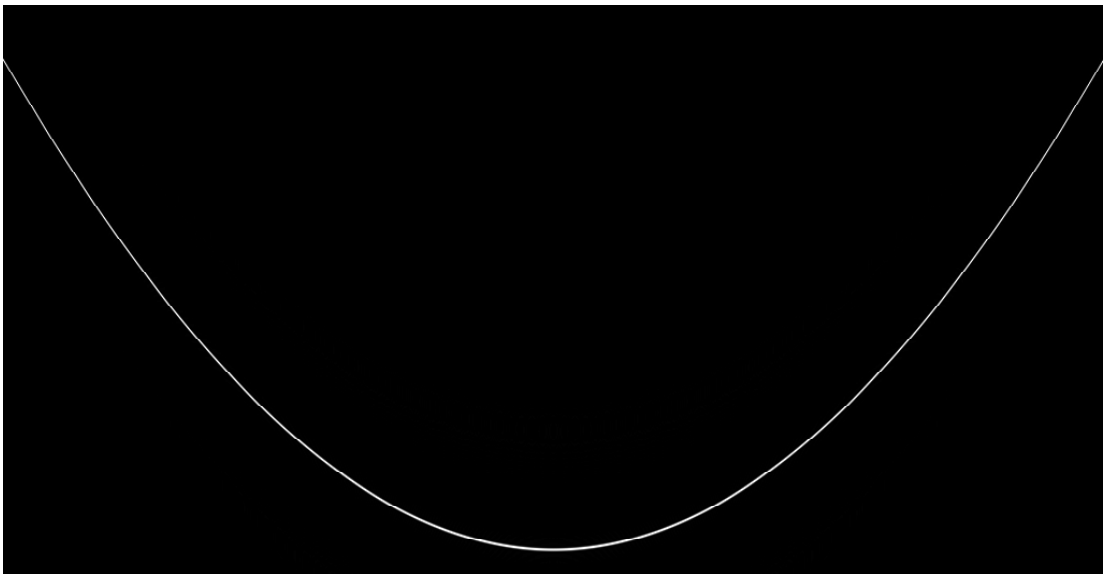

Figure 3.3: The magnitude of the range-compressed SAR simulation signal in the slant range image, azimuth signal domain (Simulation A). The range resolution is 9.74 m, the image azimuth extent is 27.979 km (horizontal) and slant range extent is 3.600 km (increases vertically).

Figure 3.6 shows, for Simulation A, a plot of the magnitude of the range samples at the target closest approach range after the range curvature correction operation in the range-Doppler domain. Note the severe taper due to the dispersion.

3.5 Performance Measures

In the characterization of focusing performance, there is no single performance parameter which will define acceptable performance for all applications. For example, the phase fidelity would be crucial for interferometric applications while the peak- or integrated sidelobe levels might be more important when making use of the power image.

Figures 3.7 to 3.10 show, for Simulation A, the magnitude of the focused target in the image domain after focusing in azimuth to 20.5 m, 10.1 m, 4.4 m, and 3.1 m, respectively (i.e. making use of increasing amounts of the available azimuth bandwidth). The azimuth- and slant range extent of the images is 150 m with azimuth displayed horizontally and slant range increasing vertically.

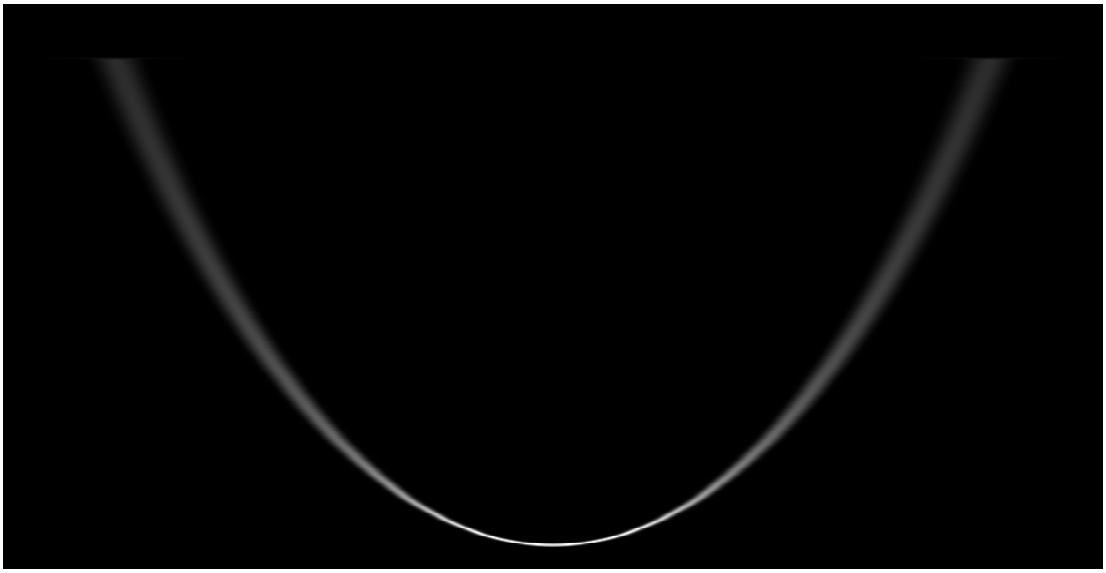

Figure 3.4: The magnitude of the simulation signal after the azimuth Fourier transform with zero Doppler frequency centred (Simulation A). The full azimuth sampling bandwidth of 250 Hz is represented by the horizontal dimension and slant range increases vertically (528 samples full image extent). The dispersion in azimuth at Doppler frequencies away from zero is clear.

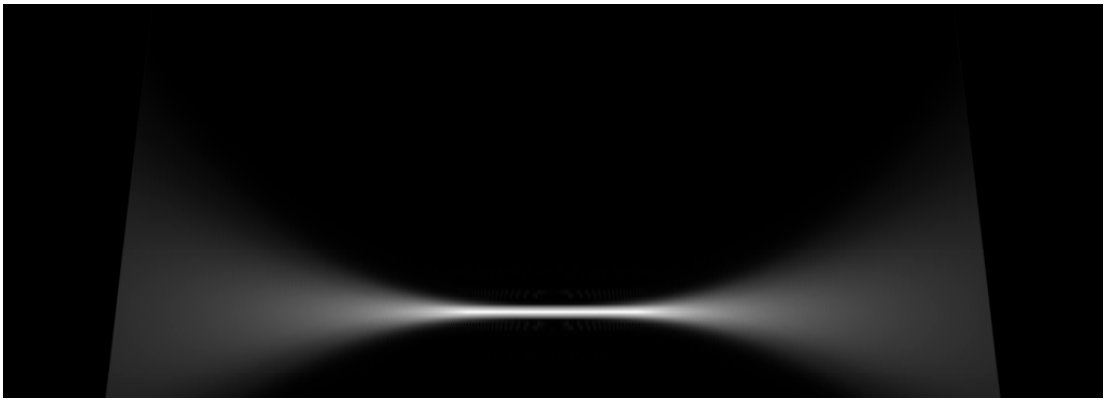

Figure 3.5: The magnitude of the signal in the range-Doppler domain after the range curvature correction operation (Simulation A). Only the first 100 of the 528 slant range bins are displayed (range increases vertically). The full 250 Hz sampling bandwidth is represented by the horizontal extent of the image.

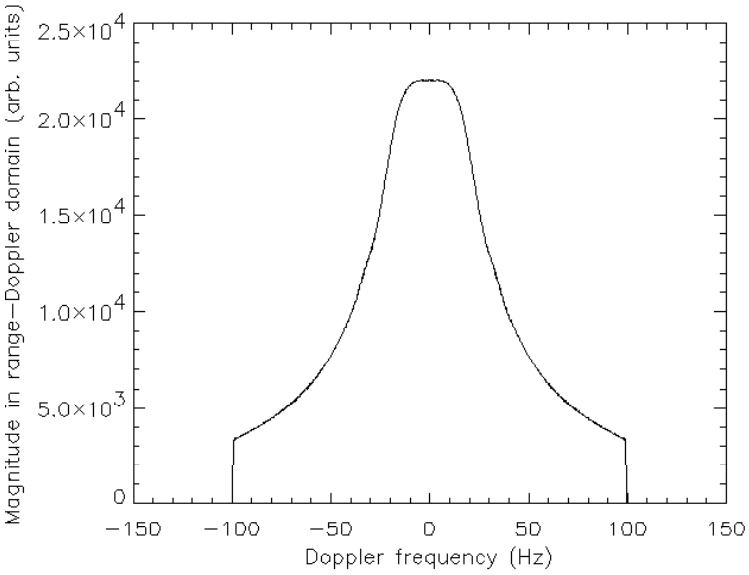

Figure 3.6: The magnitude of the signal for the range samples at the target closest approach range in the range-Doppler domain after range curvature correction (Simulation A).

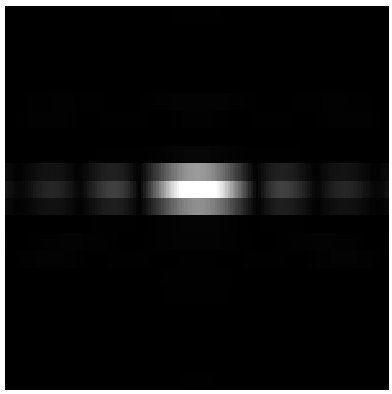

Figure 3.7: Magnitude of the focused target in the image domain focused to 20.5 m in azimuth (Simulation A).

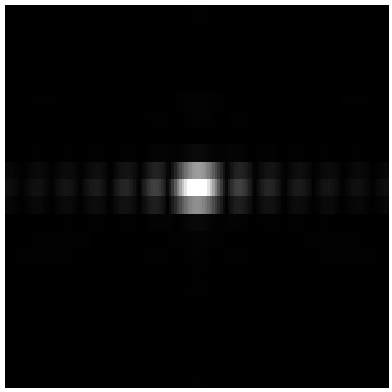

Figure 3.8: Magnitude of the focused target in the image domain focused to 10.1 m in azimuth (Simulation A).

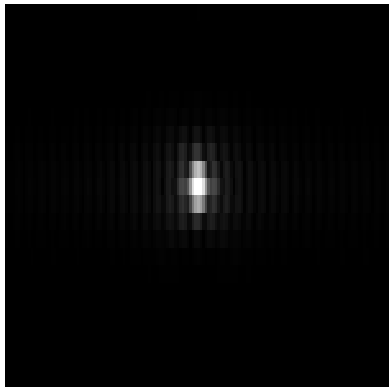

Figure 3.9: Magnitude of the focused target in the image domain focused to 4.4 m in azimuth (Simulation A).

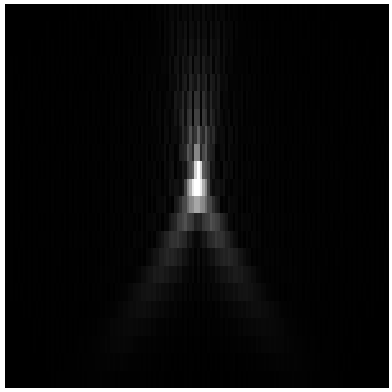

Figure 3.10: Magnitude of the focused target in the image domain focused to 3.1 m in azimuth (Simulation A).

As expected, at finer azimuth resolutions, there is noticeable degradation of the point target response. This is due to the lack of Doppler frequency dependent SRC in the processor. The diagonal features visible for the target focused to 3.1 m resolution (Figure 3.10) are attributed to dispersed target energy in the range-Doppler domain after the range curvature correction operation, as shown in Figure 3.5. This spill-over energy is no longer confined to the appropriate range sample and, as a result, is focused using an azimuth matched filter that is matched to a different range. This mismatch for the near slant range results in the spreading double peak structure which is evident in Figure 3.10.

The azimuth sidelobes due to the rectangular azimuth weighting function applied to the azimuth matched filter in Figures 3.7 to 3.10 are especially visible at the lower azimuth resolutions. For the image at 3.1 m azimuth resolution (Figure 3.10) there is considerable sidelobe suppression in a line in azimuth through the peak of the target. The reason for this is the dispersion of the energy in the range-Doppler domain. As was shown in Figure 3.6, the lack of SRC results in tapering of the target energy in the range-Doppler domain. This taper results in a form of sidelobe suppression.

For purposes of comparison with Figure 3.10, Figure 3.11 shows the focused target in the image domain for Simulation A focused in azimuth to 3.1 m where a Hamming weighting has been applied to the azimuth matched filter. Note that the Hamming window does not entirely remove the diagonal features. This is as expected, since the origin of these features is attributed to the range misfocus of the dispersed target signal resulting from the lack of SRC, rather than being produced by the same mechanism that results in sidelobes in the focused image.

3.5.1 Non-linear Phase Error in Fourier Domain

A sensitive measure of focusing performance is the residual quadratic- and higher order phase of the Fourier transformed impulse response. The technique adopted for this phase analysis, suggested to the candidate by Bamler [3], is also described by Carrara *et al.* [17] (pp. 325-328). The basic steps performed for the phase analysis of this chapter are given below and tables of the results of the analysis for each of the simulations may be found in Section 3.5.3.

- Extract a line of complex data through the peak of the focused target in the slant range image, azimuth image domain.

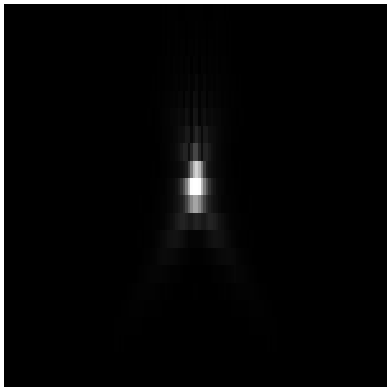

Figure 3.11: Magnitude of the focused target in the image domain focused to 3.1 m in azimuth (Simulation A). A Hamming window has been applied to the azimuth matched filter in the signal domain.

- Zero pad the data at start and end to ten times its original size.
- Take the FFT of the zero-padded data.
- Cyclic shift the peak of the spectrum to the centre of the array.
- Extract the data lying on the peak of the spectrum whose magnitude is within 40 % of the maximum magnitude of the spectrum. The 40 % figure was chosen so as to obtain data which spanned most of the frequency domain peak.
- Calculate the phases ($-\pi$ to π) for the extracted data.
- Remove the first linear phase term.
- Unwrap the phase.
- Remove the residual linear phase term.

Plots of the signal at several stages of the phase analysis algorithm described above are presented here. Figure 3.12 shows, for Simulation A, the magnitude of the focused target range profile in the slant range image, azimuth image domain after focusing to 3.1 m in azimuth. Note the degradation from a symmetric, smooth profile, as the dispersion in the range-Doppler domain has not been corrected by an SRC procedure. As a comparison, Figure 3.13 shows the magnitude of the target range profile in the same domain, but focused to 20.5 m in azimuth. The peak sidelobe visible in the

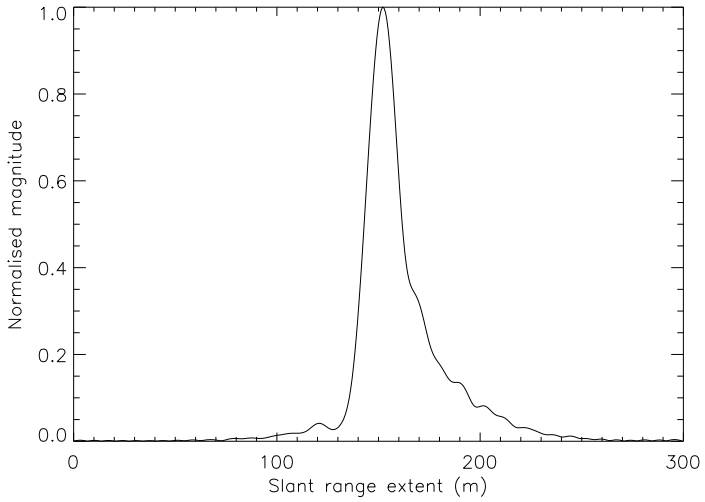

Figure 3.12: Magnitude of the focused target range profile in the image domain after azimuth focusing to 3.1 m (Simulation A).

magnitude plot has been measured to be at a level of −35.85 dB below the mainlobe peak.

Figure 3.14 shows, for Simulation A processed to 3.1 m in azimuth, the magnitude of the signal in the range frequency domain after shifting the spectrum, so that the peak is centred in the array.

Figure 3.15 shows, for Simulation A processed to 3.1 m in azimuth, the phase across the peak in the range frequency domain. Note that the phase still requires unwrapping and removal of the linear component.

Figure 3.16 shows, for Simulation A, the Fourier domain phase across the target peak in range after azimuth focusing to 3.1 m. The phase has been unwrapped and the linear component removed (Section 3.5.1). Note that the maximum residual phase error is of the order of 55 degrees. A perfectly focused target would have only a linear or flat-phase component (Carrara *et al.* [17] pg. 325). For comparison, Figure 3.17 shows for Simulation A the Fourier domain phase across the target peak in range after azimuth focusing to 20.5 m. Note that the maximum residual phase error is much reduced in this case (of the order of 2.4 deg).

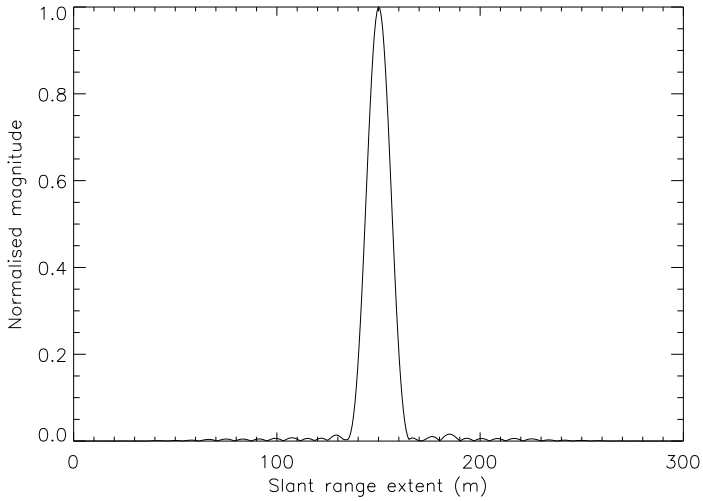

Figure 3.13: The magnitude of the focused target range profile in the image domain after focusing in azimuth to 20.5 m (Simulation A).

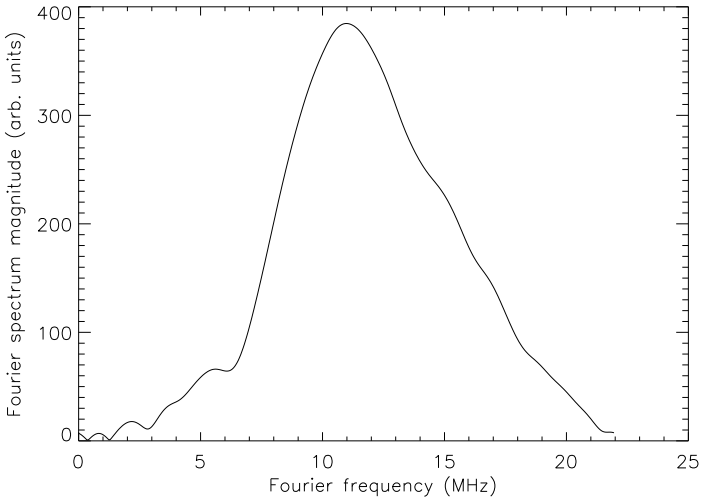

Figure 3.14: The magnitude of the range Fourier transform versus Fourier frequency extent of the focused target with the peak centred. The plot is for Simulation A processed to 3.1 m in azimuth.

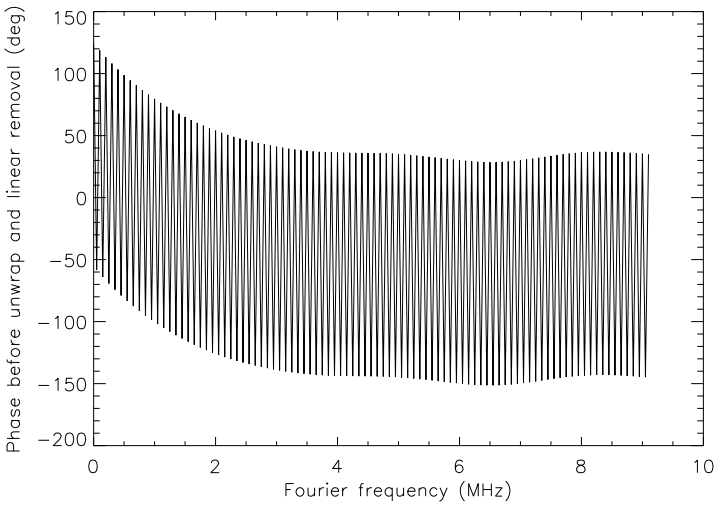

Figure 3.15: The phase across the peak of the range Fourier transform versus Fourier frequency extent through the peak of the focused target. The plot is for Simulation A processed to 3.1 m in azimuth.

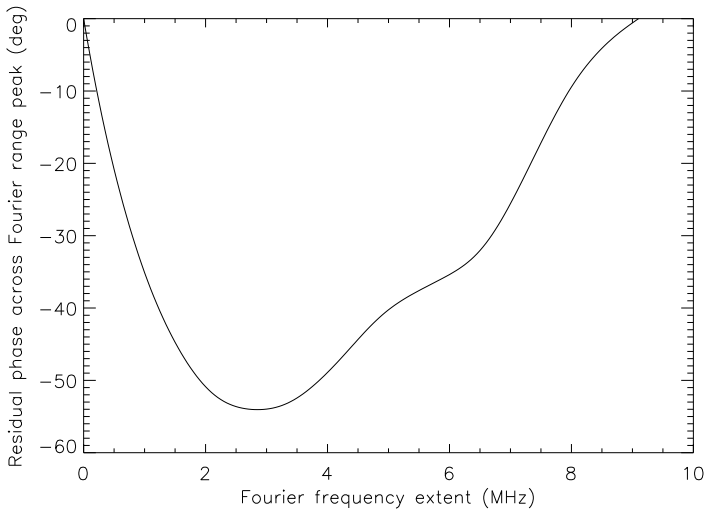

Figure 3.16: The residual quadratic- and higher order phase across the peak of the range Fourier spectrum in the range frequency, azimuth image domain (Simulation A processed to 3.1 m in azimuth).

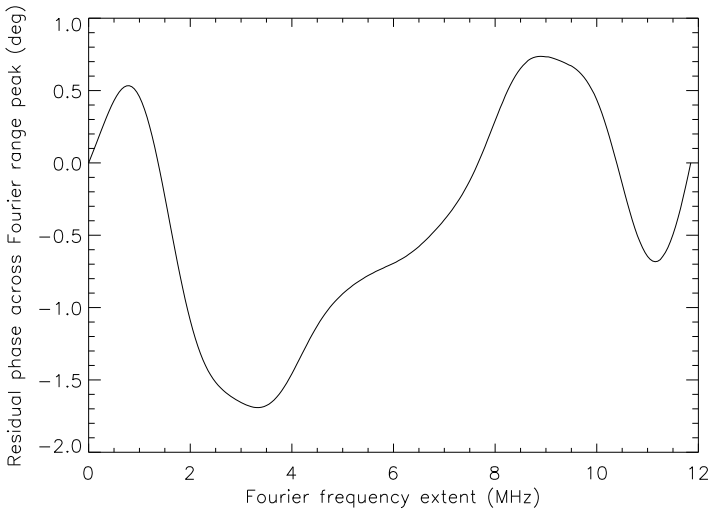

Figure 3.17: The residual quadratic- and higher order phase across the peak of the range Fourier spectrum in the range frequency, azimuth image domain (Simulation A processed to 20.5 m in azimuth).

3.5.2 Peak Analysis in Image Domain

More conventional than the analysis of the phase error in the Fourier domain as described in Section 3.5.1, is the analysis of the impulse response in the image domain. This yields performance measures such as the 3 dB resolution, the peak sidelobe level (PSL) and the integrated sidelobe level (ISL). This type of analysis was performed on the simulation results in addition to the phase analysis already described. The basic steps performed for the image domain analysis of this chapter are given below.

- Extract a line of complex data through the peak of the focused target in the slant range image, azimuth image domain. 44 range samples were used as these more than adequately covered the peak and sidelobe area.

- Upsample the data by a factor of 10 using the FFT method. The method used here was to Fourier transform the data, cyclically shift the spectrum so that the point with minimum magnitude lies at the end, zero pad the data at the end, and inverse Fourier transform.

- Calculate the power from the complex data. Note that square law detection requires that the complex data be upsampled by at least a factor of two (above

the complex sampling Nyquist rate) to avoid loss in information. Note that, in this case, the complex data has already been upsampled in the previous step by a factor of ten. Thus there is no need for further upsampling prior to the power calculation.

- Locate the main peak in the power data and measure the 3 dB resolution.
- Locate the extent of the main peak region. The main peak was defined here by the region bounded by the points at which the gradient of the peak changed sign.
- Search in the region away from the main peak for the peak sidelobe value.
- Calculate the integrated sidelobe level (ISL). This was defined here as the ratio of the integrated energy in the sidelobe region to the integrated energy contained in the main peak region. For improved accuracy, a further interpolation (using a Shannon interpolator) to one hundredth of a sample was performed on the power values during the measurement of the resolution, peak- and integrated sidelobe levels. Note here that the one-dimensional range ISL has been calculated. Although not performed in this work, calculation of the two-dimensional ISL might prove to be a useful focusing performance parameter.

Analysis of Range Resolution Degradation

As already discussed, no single performance measure is ideally suited to all applications. However, in the literature, the broadening of the range impulse response is cited as the reason for the SRC requirement (Jin and Wu [48]). In this section, graphs are presented of the (3 dB) range resolution degradation for the various simulations of Table 3.1 and processed to a number of (3 dB) azimuth resolutions. The results are presented in the form of measured values compared to the theoretical limit of resolution, where the measurements are not of real radar data, but rather from the processing of the simulated SAR data. Note that, like the range resolution, the azimuth resolution obtained is worse than the nominal theoretical value (from Equation 2.15) due to the tapering of the azimuth spectrum (Figure 3.6). The graphical method of presentation selected here has been to plot the range impulse degradation against the measured (rather than theoretical) azimuth resolution as this provides information about the actual resolutions in each dimension. Full tabular results are presented in

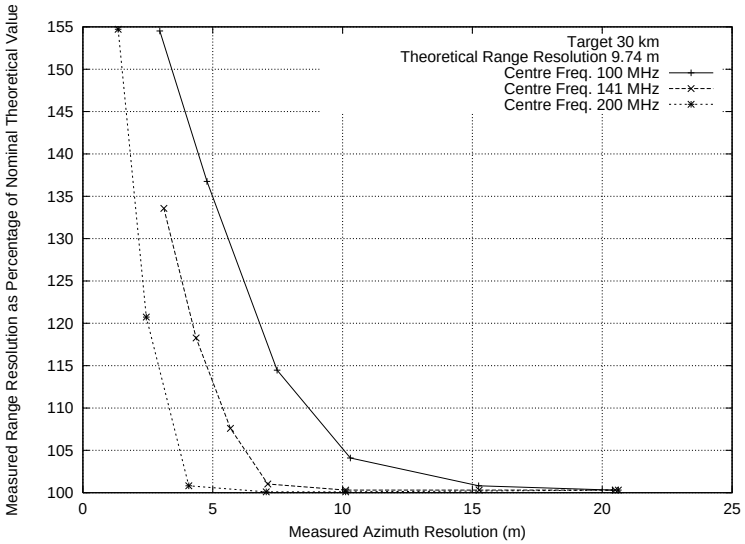

Figure 3.18: The measured range resolution of the processed simulated data as a percentage of the nominal theoretical value for radar centre frequencies of 100 MHz, 141 MHz, and 200 MHz (Simulations E, A, and F, respectively).

the following section. In all cases, the measured range resolution is compared to the range nominal theoretical value as defined by Equation 3.8 and given in Table 3.1.

Figure 3.18 shows the centre frequency dependence of the degradation of the range resolution for the focused target for three radar centre frequencies (100 MHz, 141 MHz and 200 MHz). The simulations plotted here are E, A, and F from Table 3.1. The target is at 30 km closest approach range. As expected from the previous discussion in the chapter, there is greater range resolution degradation with processing to finer azimuth resolution. Also, the range broadening effect is more severe at lower centre frequencies for given azimuth resolution and target closest approach range as there is greater range curvature at lower frequencies due to the longer synthetic apertures required.

Figure 3.19 shows the measured range resolution degradation for three theoretical range resolutions (4.87 m, 9.74 m, and 14.61 m corresponding to Simulations B, A, and C, respectively). Note that, as expected from Figure 3.2, the range resolution degradation is more severe for finer range resolutions. Note also that for the 4.87 m range resolution simulation, the value for the finest processed azimuth resolution does not follow the same trend of the other values in the curve. This is attributed to the severe degradation at fine azimuth resolutions of the focused impulse response (similar

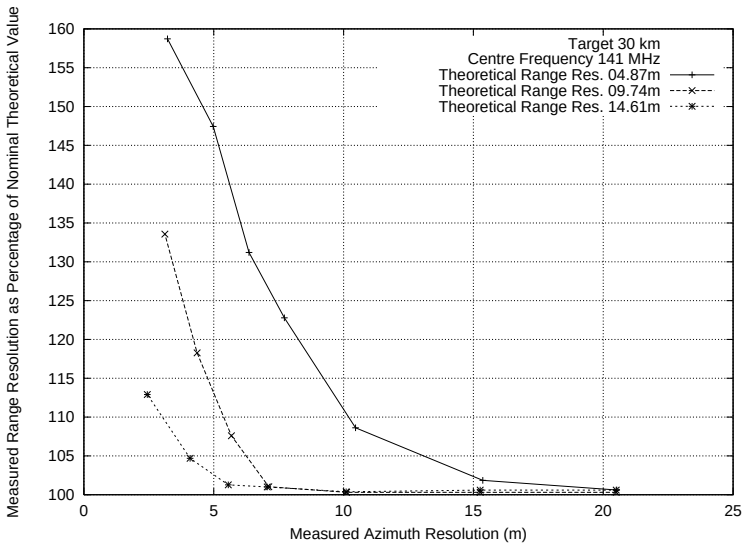

Figure 3.19: The measured range resolution of the processed simulated data as a percentage of the nominal theoretical value for three theoretical range resolutions (as marked). The centre frequency is 141 MHz and the target is at closest approach range 30 km (Simulations B, A, and C).

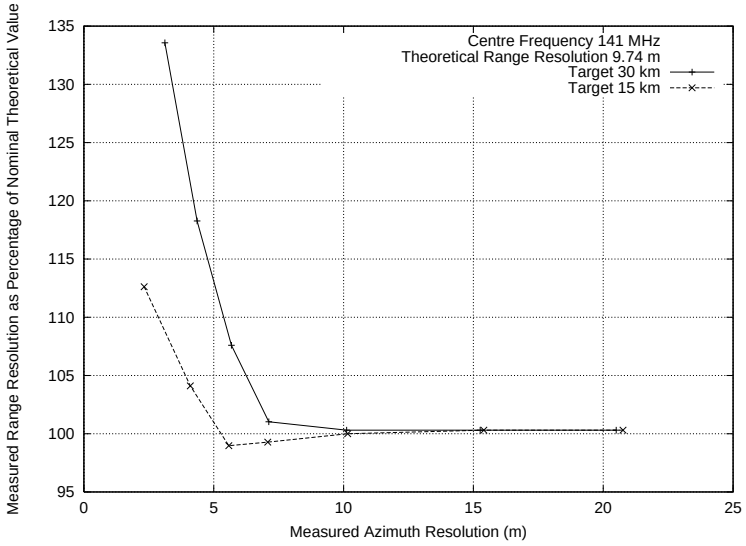

Figure 3.20: The measured range resolution of the processed simulated data as a percentage of the nominal theoretical value for radar centre frequency of 141 MHz and two target closest approach ranges, as marked (Simulations A and D).

to that displayed in Figure 3.10) which makes the range resolution measurement less meaningful.

Figure 3.20 shows the range resolution degradation for two target ranges (30 km and 15 km, corresponding to Simulations A and D, respectively). Note that the effect is more severe for the target at a greater range. This is to be expected as the range curvature is more severe for targets further away. Despite a recheck of the figures, it remains unclear why the two data points between 5 and 10 m azimuth resolution for the 15 km target should be slightly better than the theoretical values. This could be related to the target peak position straddling azimuth samples, but requires further analysis.

3.5.3 Tabular Results

Table 3.2 gives the results of the analysis of the range profiles after focusing to several (measured) azimuth resolutions. In the table: **A**20.00 denotes, for simulation A, processing in azimuth to a nominal theoretical value of 20.00 m (as given by Equation 2.15 with $K_{az\_win} = 0.89$ for the rectangular weighting used in azimuth); "Az" and "Rng" are the measured azimuth- and range resolutions (in metres), respectively, "PSL" and "ISL" are the range peak- and integrated sidelobe levels (in dB), respectively, and "Ph" is the maximum residual phase error (quadratic- and higher order) across the peak of the range spectrum after a range Fourier transform through the focused target peak (in degrees). The accuracy of the measurements presented in the tables is indicated by the number of significant figures used.

The broad trend in the increasing degradation of the range impulse reponse with finer azimuth resolution processing is clear from Table 3.2. This is witnessed by the increasing values of the range resolution, the range sidelobe levels and the range Fourier phase error. Note, in addition, from the shape of Figure 3.17 as well as the first two entries in the table for Simulation F that the maximum residual phase error does not fully characterize the residual phase error. However, the maximum phase error is a useful measure of the bounds of the phase error. Also clear from Table 3.2 is the degradation in azimuth resolution as compared with the nominal theoretical value for increasing processed Doppler bandwidths.

It is clear from the shape of Figure 3.10 that none of the quantitative performance measures presented here fully describes the degradation observed in this extreme case.

Sim	Az	Rng	PSL	ISL	Ph	Sim	Az	Rng	PSL	ISL	Ph
A20.00	20.50	9.77	-35.85	-33.64	2.4	**B**20.00	20.52	4.90	-36.08	-34.60	7.0
A15.00	15.26	9.77	-36.13	-33.49	3.3	**B**15.00	15.36	4.96	-37.11	-35.81	11.5
A10.00	10.12	9.77	-36.63	-33.97	6	**B**10.00	10.46	5.29	-41.20	-40.61	24
A7.00	7.12	9.84	-37.47	-35.15	12	**B**7.00	7.72	5.98	-46.74	-46.19	41
A5.50	5.68	10.48	-38.10	-37.39	19	**B**5.50	6.36	6.39	-47.42	-49.13	51
A4.00	4.36	11.52	-39.31	-39.73	31	**B**4.00	4.98	7.18	-33.96	-35.55	56
A2.05	3.12	13.01	-21.75	-21.39	55	**B**1.11	3.22	7.73	-10.35	-8.28	245
C20.00	20.50	14.70	-34.22	-30.61	4.1	**D**20.00	20.76	9.77	-32.66	-31.14	3.5
C15.00	15.26	14.70	-34.63	-30.90	4.1	**D**15.00	15.40	9.77	-36.17	-33.59	2.5
C10.00	10.10	14.67	-36.07	-31.24	3.9	**D**10.00	10.16	9.74	-35.97	-33.47	3.3
C7.00	7.06	14.76	-35.79	-31.94	5.6	**D**7.00	7.08	9.67	-36.67	-33.98	6.5
C5.50	5.56	14.80	-36.04	-33.03	8	**D**5.50	5.58	9.64	-37.21	-34.55	10
C4.00	4.09	15.30	-35.92	-34.79	18	**D**4.00	4.10	10.14	-37.36	-36.83	19
C1.11	2.44	16.50	-24.64	-26.50	42	**D**2.05	2.32	10.97	-23.14	-25.52	51
E20.00	20.40	9.77	-35.97	-33.47	4.7	**F**20.00	20.62	9.77	-32.55	-31.09	3.4
E15.00	15.24	9.82	-36.18	-33.99	8	**F**10.00	10.12	9.75	-35.76	-33.40	2.8
E10.00	10.30	10.21	-38.07	-36.60	17	**F**7.00	7.06	9.75	-36.38	-33.72	4.7
E7.00	7.48	11.15	-39.96	-40.63	34	**F**4.00	4.08	9.82	-37.48	-34.71	12
E4.00	4.78	13.32	-43.69	-45.51	51	**F**2.05	2.44	11.76	-44.17	-41.14	28
E2.05	2.96	15.05	-16.79	-15.93	65	**F**1.11	1.36	15.07	-18.90	-20.66	130

Table 3.2: Simulation results (refer to main text)

A plot of the 2-D Fourier phase error could be a useful tool here or the image itself may be the most appropriate form of presentation for a particular application.

3.6 Summary

In this chapter, investigation has been made into the processing limits of the range-Doppler algorithm when applied without Doppler-frequency-dependent secondary range compression. The investigation has focused on airborne, stripmap SAR systems operating in the $100 - 200$ MHz region where the Doppler centroid of the beam is zero. To the best of the candidate's knowledge, no similar work has been performed or published by any other researcher. The initial work on SRC by Jin and Wu [48] [1] focused on the scenario with the range walk much more severe than the range curvature (i.e. the narrow beam, squinted case).

In addition to centre frequency, investigation has been performed into the effects of target range and the range compressed pulse resolution. Although the results presented in no way cover the full range of possible target range, radar centre frequency and range resolution parameters, the information presented may be used as a guideline for certain systems to assist in the decision as to whether Doppler frequency dependent SRC is required for a particular application. This decision will depend on the particular system specification.

There is no one measure which will define "acceptable" focusing performance for all applications. The major emphasis in the graphical presentation of the simulation results here has been on the degradation in the range resolution as this has been the reason cited as the reason for the SRC requirement in the literature. A more sensitive performance measure than the range resolution has been found to be the quadratic and higher order phase error across the peak of the Fourier transform of the focused range profile. Range peak- and integrated sidelobe levels and azimuth resolution degradation have also been measured.

Another objective for the chapter has been to provide a more intuitive understanding of the requirement for secondary range compression in range-Doppler processing with severe range curvature than is currently available in the largely mathematical literature on the subject (Jin and Wu [48], Curlander and McDonough [20] pp. 199-207). It is hoped that this has been achieved through the novel presentation of the subject and the choice of imagery presented.

In the following chaper, an extension to range-Doppler processing is discussed and demonstrated to cater for accurate processing of signals with severe range curvature.

Chapter 4

An Extension to Range-Doppler SAR Processing to Accommodate Severe Range Curvature

4.1 Introduction

In Chapter 3, the requirement for Doppler frequency dependent SRC for range-Doppler processing of signals with severe range curvature has been discussed. Also noted was that the implementation of such a correction for range-Doppler processors is difficult to achieve (Bamler [7]).

Apart from range-Doppler processing, other approaches receiving popular interest are the chirp scaling algorithm (Raney *et al.* [51]) and the range migration algorithm (Cafforio and Rocca *et al.* [16][54]). Difficulties with the use of these are: the chirp scaling approach requires range chirped data and becomes less accurate when applied to low frequency, high resolution processing of large scenes (Carrara *et al.* [17] pp. 485); the range migration approach, although well suited to low frequency processing, makes use of the Stolt interpolation which is difficult to implement accurately in practice (Bamler [7]).

The primary objective of this chapter is to demonstrate that an extended range-Doppler processor is capable of much more accurate processing of signals with severe range curvature than a standard range-Doppler processor not implementing Doppler

frequency dependent SRC.

What makes this work relevant is that it provides a fairly straightforward mechanism for extending the capability of an existing range-Doppler processor to the case of severe range curvature as is typically experienced for high resolution processing at VHF frequencies. The basic idea of the extension, first published by Raney and Vachon [52], is to make an initial correction in the 2-D frequency domain to a reference range, followed by a residual correction in the range-Doppler domain.

The extended algorithm is very flexible in that it is applicable to both airborne and spaceborne data, range compressed and range uncompresed signals, and to cases of both severe range walk and severe range curvature (also noted by Raney and Vachon [52]). In general, the extended algorithm, as implemented here, requires more computation than the standard range-Doppler algorithm, but many elements may be pre-computed and re-used.

As in Chapter 3, the simulations presented in this chapter are for an airborne, VHF (limited to the 141 MHz case here), strip-map, wide beam, side-looking SAR system without range walk (i.e. imaging geometries with zero Doppler centroid). As in Chapter 3, the emphasis of the quantitative analysis is on the range impulse response (range resolution, peak sidelobe level, integrated sidelobe level, and quadratic and higher order phase error across range Fourier spectrum peak) although attention is also given to the azimuth resolution. Outside the scope of this thesis is the important future extension of the work to include comparisons with other benchmark algorithms such as the chirp scaling approach and the range migration approach when applied to signals with severe range curvature.

The idea for the extended range-Doppler algorithm was suggested to the candidate by Michael Jin in a private discussion [1]. All of the material in this chapter, including the development, coding, simulation and testing of the extended algorithm is the candidate's own work. Some of the material appearing in this chapter will be published in the Proceedings of IGARSS '99 [35].

After completion of the extended processor development, the work presented in this chapter, and the submission of the full IGARSS '99 paper [35] (subsequently slightly revised), it was brought to the candidate's attention by Richard Bamler of DLR [2] that an algorithm with the same main steps had been published by Raney and Vachon [52].

Raney and Vachon, however, while noting that their algorithm would be applicable to the severe range curvature case, applied the approach to the simulation of a narrow beam SAR (3.6 deg) with large squint (45 deg). In addition, the independently developed implementation described here differs from that described by Raney and Vachon. For example, Raney and Vachon efficiently (but with some approximations) generate the 2-D reference function in the 2-D frequency domain directly from mathematical expressions for the signal from a point scatterer in this domain.

4.2 Simulation and Processing Assumptions and Parameters

The extended range-Doppler algorithm is demonstrated in this chapter through the processing of simulated data from a VHF (141 MHz centre frequency) airborne SAR sensor. The simulation assumptions and parameters are introduced at this point so as better to allow use of the simulated signals in demonstrating the operation of the extended algorithm. A mathematical treatment is provided by Raney and Vachon [52]. The simulation parameters were chosen to allow for processing within a reasonable time on the available processing hardware[1] and to be very close to those of Simulation A of Chapter 3 for comparison purposes. The input to the processors was chosen to be already range compressed as this resulted in more manageable aray sizes. Larger simulations with more targets widely separated in range and azimuth were not practical given the available processing hardware.

The simulation and processing setup, assumptions and notation are:

- side-looking (Doppler centroid zero), airborne (flat earth geometry), strip-mapping SAR with perfect motion compensation
- stop-start approximation valid - motion only between pulses (Barber [9])
- adequate sampling in range and azimuth for Nyquist criterion
- all plots and analysis are slant range rather than ground range and all analysis applied to single look imagery
- all imagery has been scaled for display purposes so that the maximum value corresponds to the image format maximum (255 for 8-bit images)

[1] Dual Intel Pentium Pro 200 MHz with 512 MB RAM running under SMP.

- stationary point targets with uniform amplitude and phase response over azimuth angles (Axelsson [6]) and no antenna weighting effects (targets visible over simulation extent)
- stationary point targets at 30 km and 31 km closest approach range with uniform amplitude and phase response over azimuth angles
- range compression prior to A/D (note, however, that the extended and standard processors can both cater for range uncompressed input signals)
- 20 MHz range chirp with Hamming weighting during range compression (resulting theoretical range resolution 9.74 m)
- simulation azimuth extent 28911 m, PRF 250 Hz, ground speed 250 m/sec (Doppler bandwidth of 199 Hz and maximum range curvature of 3205 m for 31 km target)
- A/D sampling at 22 MHz (6.81 m slant range sample spacing) using 8-bit I and Q (4 byte I and Q floating point used throughout processors)
- 646 range samples (covers slant range 29850 m - 34250 m)
- single look processing to 1.78 m nominal (theoretical) azimuth resolution, making use of 125 Hz of available Doppler bandwidth with rectangular azimuth weighting in both processors (Equation 2.15)
- 8-pt Shannon interpolation kernels used in range curvature correction in both processors
- reference function updated every range bin for range-Doppler domain azimuth processing in both processors

For purposes of comparison, the simulated data was processed using three methods:

1. standard range-Doppler processor
2. extended range-Doppler processor with 30 km reference range
3. extended range-Doppler processor with 25 km reference range. These results give more of an indication of the range sensitivity of the extended processor when applied to scenes with larger range extent.

The simulated data was generated using Rolf's Simulator (Lengenfelder [41]), developed at UCT. The SAR processors used were the (airborne, range-Doppler) G2 Processor (used as the "standard range-Doppler processor") and the extended range-Doppler processor, both developed by the candidate at UCT.

4.2.1 Standard Range-Doppler Processor Functionality

Although the G2 Processor has much functionality built in, such as the ability to perform range compression, interference suppression, motion compensation, and multilook, only the following functionality was required for these tests:

1. Corner turn the simulated data file (I and Q byte format and already range compressed).

2. Read in an azimuth line of the corner turned data, removing the DC offsets (set to 127 in the simulator) and store in 4-byte IEEE floating point I and Q format.

3. Zero pad the data and perform an azimuth Fourier transform of the azimuth line.

4. Perform range curvature correction of the data in range-Doppler domain using 8-pt Shannon interpolator.

5. Create a one-dimensional azimuth reference function with rectangular weighting in the signal domain matched to the range of the azimuth line being processed. The reference function is generated as the time-reversed, complex conjugate of the phase response of a point target at the range of interest. The reference function length was chosen for each range so as to process to the theoretical 1.78 m azimuth resolution (125 Hz Doppler bandwidth with rectangular weighting).

6. Zero pad azimuth reference function and perform Fourier transform.

7. Multiply curvature corrected range line with reference function in range-Doppler domain.

8. Perform inverse azimuth Fourier transform of azimuth line to form an azimuth line of the focused image.

9. Repeat steps 2 - 8 for the next azimuth line until all azimuth lines processed.

4.3 Extended Range-Doppler Algorithm

4.3.1 Overview

Figure 4.1 shows the basic steps (labelled A to H) of the extended algorithm. On the right of some of the steps, the magnitude of the data and reference function at various stages in the processing are shown schematically. The algorithm differs fundamentally from the standard range-Doppler algorithm in that an initial convolution is performed with a 2-D reference function matched to a point target signal response at some reference range. The choice of which reference range to choose influences the focusing performance over the image with the most accurate focusing at the reference range. Thus, a reasonable choice is to make the mid range in the image the reference range. For efficiency, the initial convolution is performed in the 2-D frequency domain (Step E). This step effectively removes from all scatterers in the scene the range curvature and Doppler phase history of a scatterer at the reference range. In addition, through an appropriate choice of the reference function, range compression (with range sidelobe weighting) may be performed at the same time, as may correction for severe range walk, if required.

After this step and a subsequent inverse range FFT, only a residual range curvature correction interpolation and a residual azimuth focusing phase correction remains to be performed in the range-Doppler domain (Step G). As the residual range curvature is, in general, much smaller than the initial range curvature, the requirement for Doppler-frequency-dependent SRC is alleviated. The processing performed in Step G is similar to that performed for conventional range-Doppler processing, except that the processor only corrects for the residual values. The corner turn between Steps G and H could equally well have been done between Steps F and G. Where this is performed will naturally affect the practical implementation of Step G. The position of this corner turn operation in Figure 4.1 is as implemented by the candidate.

The description and simulation analysis performed in this chapter refers to single look processing. The extended range-Doppler processor may, however, accommodate multilook processing through dividing up the azimuth bandwidth in Step G in the same way as may be performed for the standard range-Doppler algorithm.

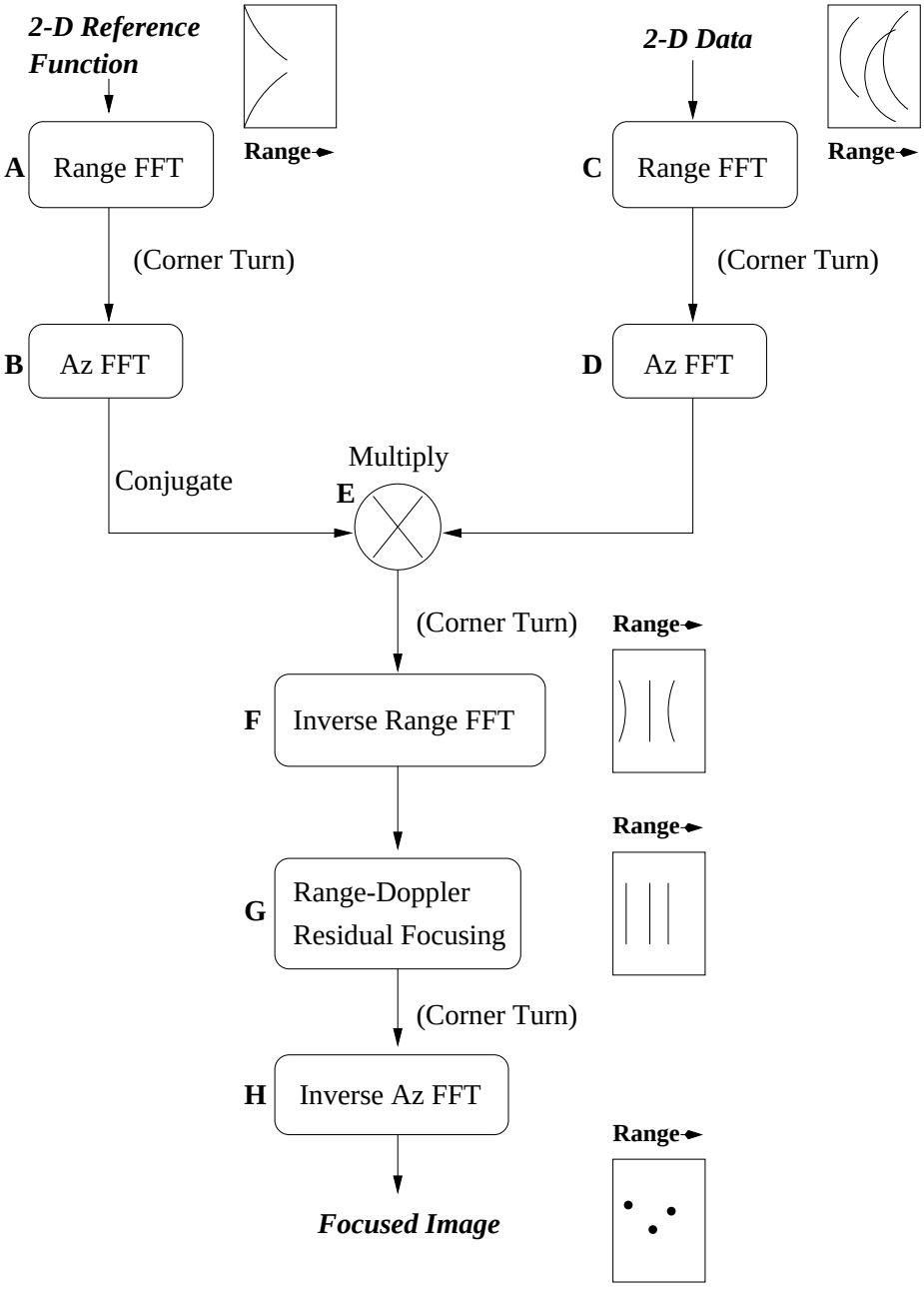

Figure 4.1: The extended range-Doppler algorithm.

4.3.2 Implementation and Detailed Steps

2-D Reference Function Generation

Figure 4.2 shows the 2-D reference function matched to a 30 km closest approach target range in the signal domain. The reference function has been cyclically shifted in range and azimuth so that the zero Doppler point lies at the origin. Practically, this cyclic shift allows for easier processor implementation as the convolution with this reference function maintains the data position in the arrays. The reference function is the input to Step A.

For the work reported here, the 2-D reference function was generated using the same radar simulator as was used to generate the data, but with only one point target at the reference range. Thus, the reference function included a voltage scaling according to R^2 from the radar equation (Skolnik [58] pg. 521). For the 30 km target, the voltage scaling reduction introduced by this effect due to the range curvature at the edge of the processed synthetic aperture was small (7 percent for the 30 km reference function). Range compression of the reference function was performed in the simulator (according to Equations 2.31 and 2.32) using a rectangular window, since a Hamming window had already been applied in the generation of the range-compressed data for range sidelobe suppression. As in the case of the data generation, the reference function was quantized to 8-bit I and Q at the simulator output. The range compressed signal for some azimuth time at the output of the simulator is of the form given by Equation 2.28 where the voltage scaling is incorporated into the constants.

Note that using the same radar simulation software to produce the pseudo data and the 2-D reference function is not an ideal approach as there is the potential for the cancellation of errors. However, there are some mitigating arguments. Firstly, the reference function generated with the simulator performs only part of the focusing operation. The other part is performed in the extended processor residual correction stages. Errors in the simulated data and reference function generation would not result in correct focusing for points away from the reference range. The simulator output has, in addition been the subject of close scrutiny over a lengthy period at the University of Cape Town and the candidate is confident that the output signals are correct (to within the stop-start approximation). The same simulator has been successfully used by other researchers with other processing algorithms.

It proved practically convenient to create the reference function array to be the

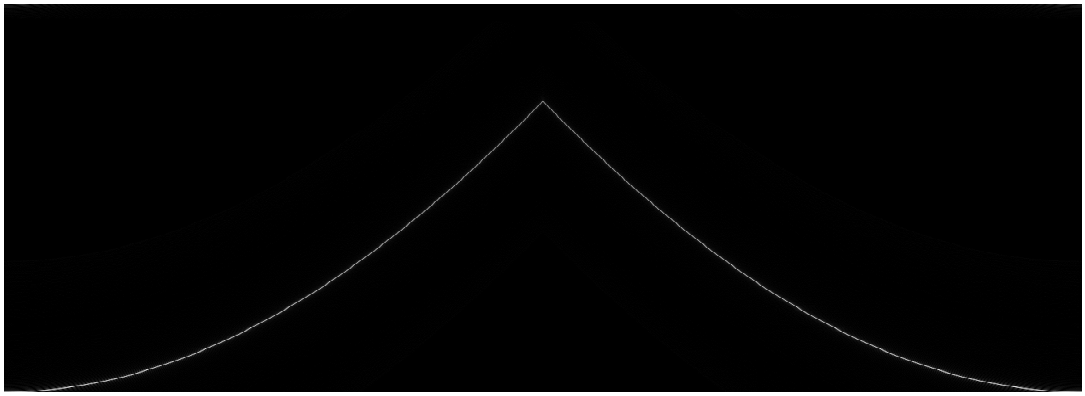

Figure 4.2: The magnitude of the 30 km reference function, cyclically shifted so that the zero Doppler point lies at the origin. Azimuth extent (horizontal) is 29811 m and range extent (vertical) is 4400 m.

same size as the data arrays for these simulations, but when processing extended scenes, more efficient for this method of reference function generation would be to only create an initial reference function with size sufficient for the longest sythetic aperture required in the image. It should also be noted that, for efficiency, reference functions used as input to Step E should be precomputed and stored for any particular system and viewing geometry, removing the requirement for regeneration with each scene.

Prior to the range FFT of Step A, the reference function in the signal domain was zero-padded out to 1024 samples (from 646). This allowed for use of more efficient FFT routines and reduces wrap-around effects in the processed image. For the same reasons, the output from Step A was zero padded in azimuth to 32768 samples prior to the azimuth FFT of Step B.

Figure 4.3 shows the magnitude of the 30 km reference function spectrum in the 2-D frequency domain (after Step B) and zero-centred for display purposes. The azimuth (Doppler) frequency extent (horizontal) is 250 Hz and the range frequency extent (vertical) is 22 MHz. The trapezoidal shape is due to the higher range frequency components displaying larger Doppler frequency extent.

More efficient than the approach described above of signal domain generation of the 2-D reference function is to generate the 2-D reference function in the 2-D frequency domain directly from analytical expressions. This is the approach adopted by Raney and Vachon [52]. The mathematical expression for the 2-D reference function

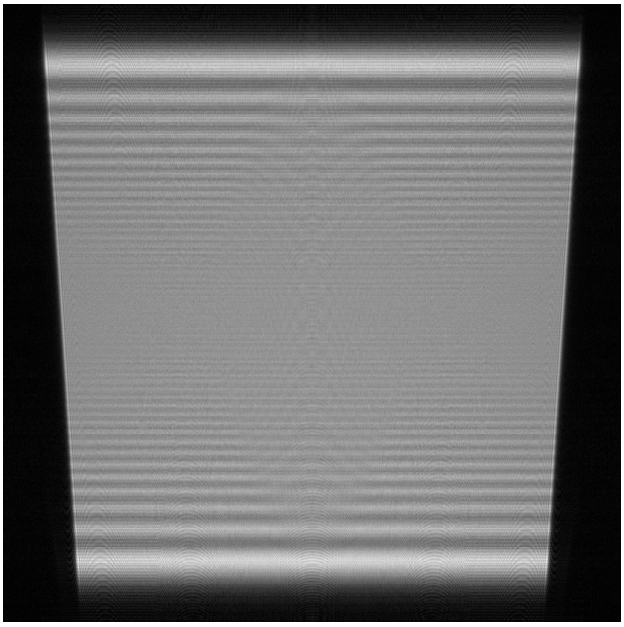

Figure 4.3: The magnitude of the 30 km reference function in the 2-D frequency domain (as input to Step E), zero-centred in both dimensions. Full image azimuth frequency extent (horizontal) is 250 Hz, full range frequency extent (vertical) is 22 MHz.

in the 2-D frequency domain would be a conjugated form of Equation 2.29. The only approximation used in the derivation of this expression is the Principle of Stationary Phase.

Processing of Data

Figure 4.4 shows the magnitude of the simulated raw data in the signal domain for the targets at 30 km and 31 km closest approach slant range. The raw data is the input to Step C.

Figure 4.5 shows the magnitude of the data in the 2-D frequency domain (after Step D) and zero-centred for display purposes. The dimensions are as for Figure 4.3. Note that, due to the presence of two targets rather than one, the 2-D spectrum of the data shows a more complicated structure than that of the reference function. In addition, note the range spectrum weighting in Figure 4.5 due to the Hamming window applied during the range compression stage of the data in the simulator. This differs from the reference function spectrum of Figure 4.3 where a rectangular weighting was applied during the range compression.

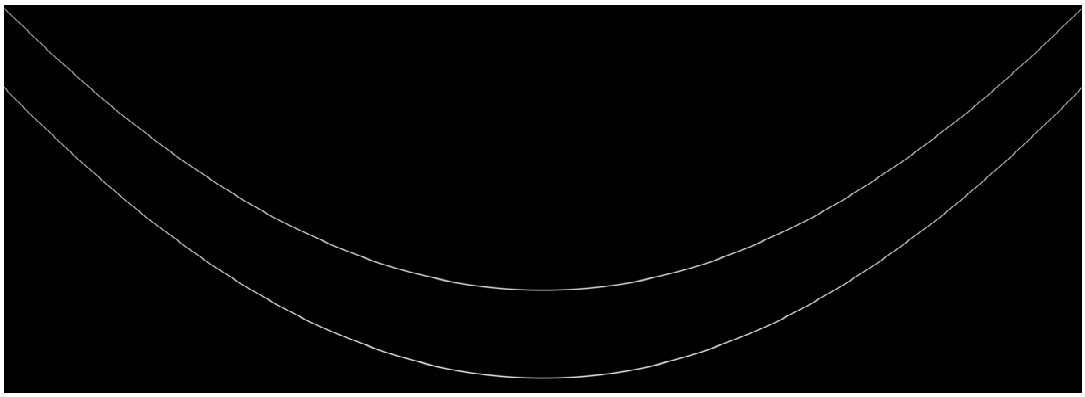

Figure 4.4: The magnitude of the range compressed simulated target returns in the range image, azimuth signal domain. Azimuth extent (horizontal) is 28911 m, range extent (increasing vertical) is 4400 m.

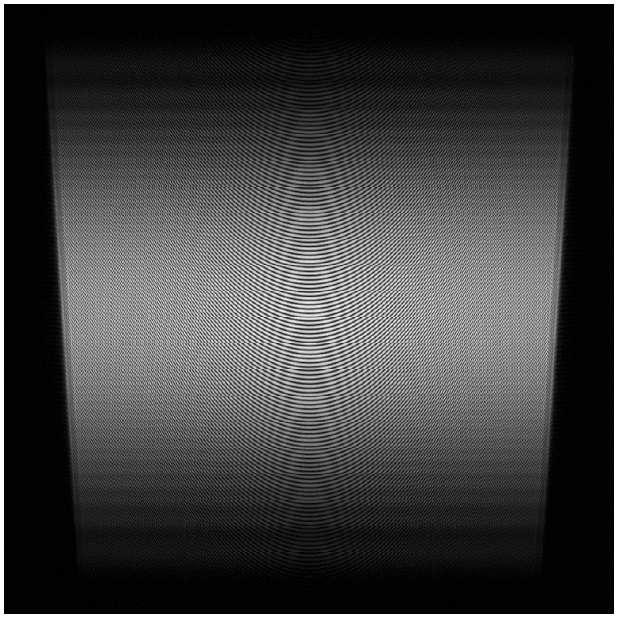

Figure 4.5: The magnitude of the simulated data for the two targets in the 2-D frequency domain (as input to Step E), zero-centred in both dimensions. Full azimuth frequency extent (horizontal) is 250 Hz, full range frequency extent (vertical) is 22 MHz.

The convolution of the initial reference function and data is performed through a multiply operation in the 2-D frequency domain for efficiency. This is shown as Step E in Figure 4.1. Note that it is required for the convolution operation that the reference function, as generated here, be conjugated prior to the multiply.

Figure 4.6 (see caption) shows the magnitude of the signals from the two targets in the range-Doppler domain for three processing methods, immediately prior to the range curvature correction and azimuth focusing (after Step F for extended algorithm). Clearly visible is the severe dispersion for the standard range-Doppler processing which results in degraded image quality. Note also, that the 30 km target with the 30 km reference range requires no further range curvature correction or phase correction for azimuth focusing.

Figure 4.7 shows, for the extended range-Doppler processor, the magnitude of the data in the range-Doppler domain after the residual range curvature correction. This figure shows the importance of selecting a value for the reference range so as to minimize errors at the extremes of the image. As expected, a small dispersive effect is still visible for the 25 km reference range, but this dispersion is a large (visual) improvement over the dispersion for standard range-Doppler processing. The azimuth frequency extent of the signals in Figure 4.7 is limited by the residual focusing of Step G to the 125 Hz required for the azimuth resolution requirements.

Focused Images

After Step G, the only remaining operation required to form the complex image is an inverse azimuth FFT. Figure 4.8 shows the magnitude of the two focused targets for standard range-Doppler processing, the extended algorithm with 25 km reference range and the extended algorithm with 30 km reference range. The improvement with the extended algorithm over standard range-Doppler processing is easily observable. A much smaller improvement with the 30 km reference range over the 25 km reference range is also visible on close inspection. This is shown more clearly in Figure 4.9 which is a zoomed-in region of Figure 4.8 around the 30 km target for the three processing methods.

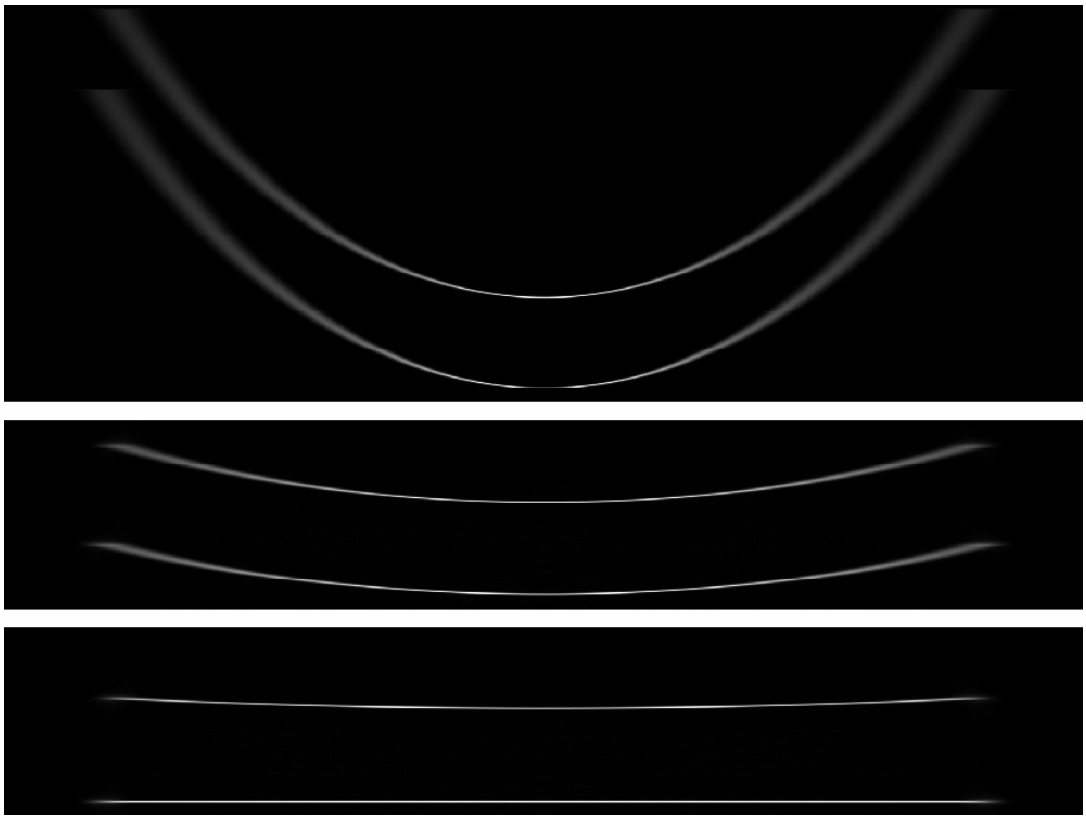

Figure 4.6: The data in the range-Doppler domain (zero-centred) prior to range curvature correction and azimuth focusing for three processing methods (after Step F for extended algorithm). Top is the standard range-Doppler processing, middle is with the extended algorithm after correcting to a 25 km reference range, and bottom is the extended algorithm with 30 km reference range. The targets are at 30 km and 31 km closest approach range (increasing vertical) and the full azimuth frequency extent displayed is 250 Hz (horizontal).

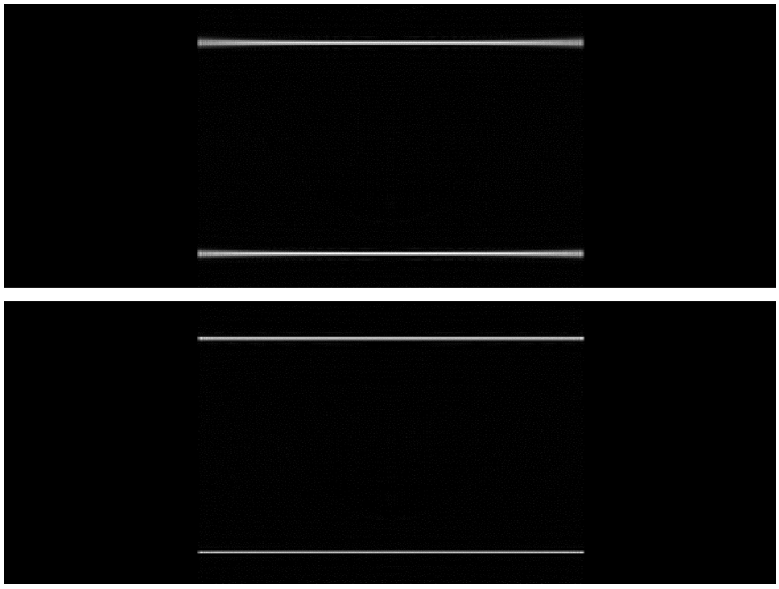

Figure 4.7: The data in the range-Doppler domain (zero-centred) after residual range curvature correction (Step G). Top is for the 25 km reference range and bottom for the 30 km reference range. Slant range increases vertically with the targets 1 km apart and the full 250 Hz sampling bandwidth is displayed horizontally.

4.4 Focusing Performance Comparisons

Table 4.1 shows the measured results of processing the simulated point target data using the extended range-Doppler algorithm and also the standard approach. "Ex 30" denotes processing with the extended algorithm using a reference range of 30 km, "Std R-D" denotes standard range-Doppler processing, "Res" is the 3dB resolution, "PSL" the peak sidelobe level, and "ISL" the integrated sidelobe level. "Phase Error" is the residual quadratic- and higher order maximum phase error across the range Fourier peak, a sensitive measure of focusing performance (Carrara *et al.* [17] pp. 323-328).

Analysis was performed in the range and azimuth dimensions through the peak of each target. From the shape of the distorted targets of Figures 4.8 and 4.9, it is clear that the one-dimensional measures of focusing performance given in Table 4.1 do not give the full picture. However, these (with the exception of the phase error) are fairly standard measures which appear often in the literature and do provide some basis for comparison. There is scope for future work here in developing more representative focusing performance indicators (a point already raised in Chapter 3).

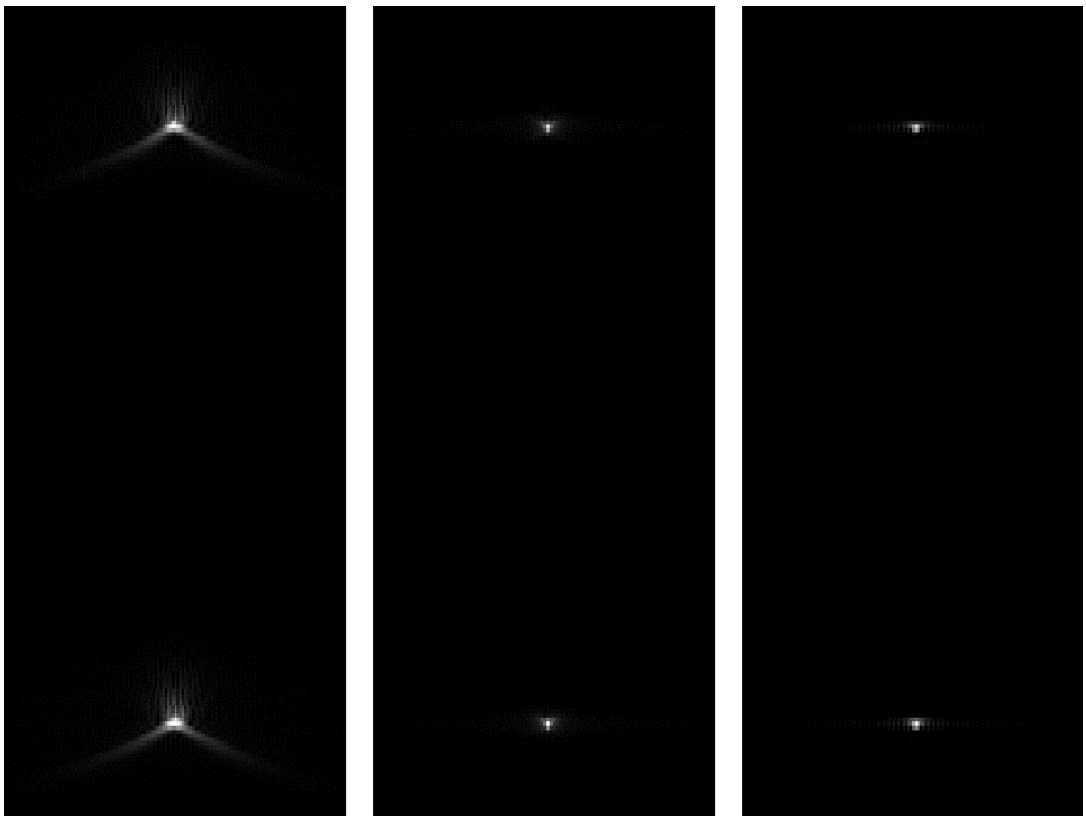

Figure 4.8: The focused targets at 30 km and 31 km slant range for three processing methods. Left is for standard range-Doppler processing, middle for the extended algorithm with 25 km reference range, and right for extended algorithm with 30 km reference range. Slant range extent 1364 m (increases vertically) and azimuth extent (horizontal) is 140 m.

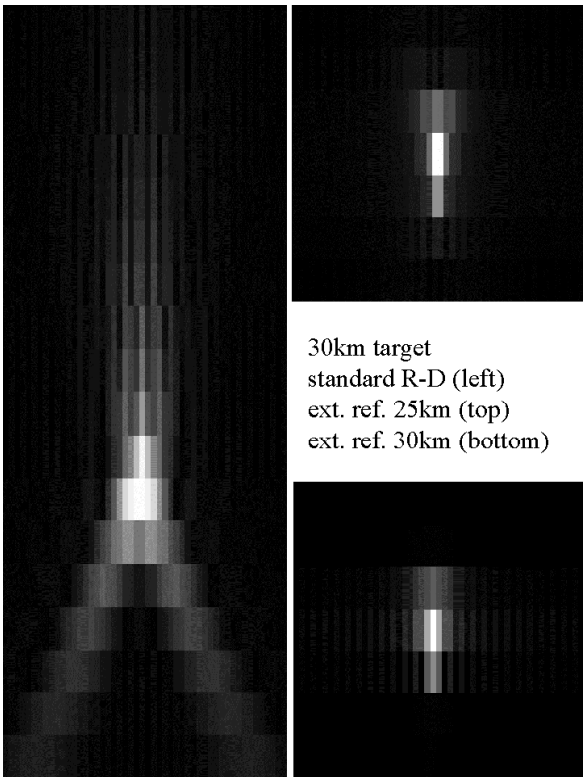

Figure 4.9: The focused 30 km target for standard range-Doppler processing and the extended algorithm with two reference ranges (as marked). Images are all to the same scale (small images 50 m on a side) with azimuth horizontal and slant range increasing vertically.

Proc.	Tgt Rng	Az Res.	Rng Res.	Rng PSL	Rng ISL	Phase Error
Ex 30	30 km	1.86 m	9.14 m	-38.72 dB	-34.62 dB	4.5 deg
Ex 30	31 km	1.89 m	9.10 m	-36.52 dB	-33.09 dB	2.5 deg
Ex 25	30 km	1.91 m	9.89 m	-29.15 dB	-30.12 dB	24 deg
Ex 25	31 km	1.96 m	10.29 m	-28.39 dB	-29.88 dB	27 deg
Std R-D	30 km	6.09 m	11.28 m	-12.38 dB	-11.10 dB	65 deg
Std R-D	31 km	5.51 m	12.75 m	-15.07 dB	-13.92 dB	63 deg

Table 4.1: Measured processing results (refer to main text)

For the resolution and sidelobe measurements the complex output from the processors was upsampled by inserting zeros in the middle of the smallest (close to zero) portion of the Fourier spectrum. For the analysis, 300 azimuth bins (then upsampled by a factor of 400) and 47 range bins (then upsampled by a factor of 200) were extracted for each target. The PSL and ISL figures were calculated by assuming that the main peak extent was defined by the points at which the gradient of the main peak changed sign.

For the phase analysis, the complex data was upsampled by a factor of 10 by zero padding prior to the FFT. The phase analysis measurements were taken across the region of the peak of the range spectrum limited by 40% of the maximum magnitude (40% was chosen to cover most of the peak spectrum). Upsampling of the complex output image was performed prior to all the measurements by zero padding at an appropriate part of the Fourier spectrum in each dimension.

Table 4.1 shows that there is a significant loss in both range and azimuth resolution and large increase in sidelobe levels with the conventional range-Doppler processing over the extended algorithm due to the severe dispersion of the signal in the range-Doppler domain. The degradation in processing performance is also reflected in the maximum phase error figures. As expected, the 25 km reference range processing with the extended processor does not give quite as good processing performance as when using the 30 km reference range for these targets.

The 30 km target processed with the 30 km reference range extended processor displays a slightly worse figure for the range resolution (9.14 m) than for the target at 31 km with the same reference range (9.10 m). This is attributed to rounding error in determining the peak extent of the upsampled data (267 as opposed to 268 samples). In addition, the slightly worse maximum phase error of 4.5 degrees over 2.5 degrees is

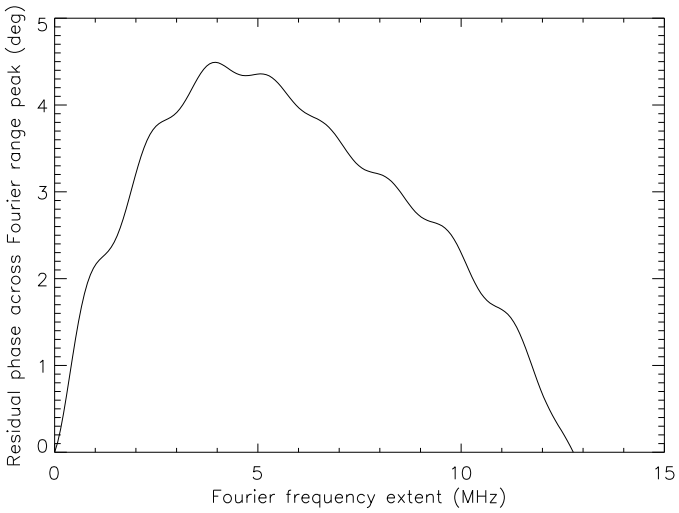

Figure 4.10: The quadratic- and higher order range Fourier phase error for the extended processor with 30 km reference range and 30 km target.

merely an indication that the *maximum* phase error does not convey all the information contained in the shape of the phase error curve. The range Fourier phase error curves for the above-mentioned cases are shown in Figure 4.10 (30 km target) and Figure 4.11 (31 km target), and for the standard range-Doppler processing of the 31 km target in Figure 4.12.

Also of interest is that the range resolution measured for the 30 km reference function is slightly *better* than the nominal theoretical value of 9.74 m (20 MHz chirp with Hamming window function - Equation 2.14). This is attributed to a slight modification of the range weighting applied when convolving with the initial 2-D reference function. The non-zero phase error of 4.5 deg for the 30 km target with the 30 km reference function is attributed to quantization and interpolation effects in the processing.

It is clear from the tabular results that the extended algorithm provides significantly improved processing performance over standard range-Doppler processing for this simulated radar data. The improvement reflected by the figures in Table 4.1 is also easily observed in the processed images. Figure 4.13 shows the range profiles of the 31 km target after processing with the extended algorithm with a reference range of 30 km and after processing with the standard range-Doppler approach.

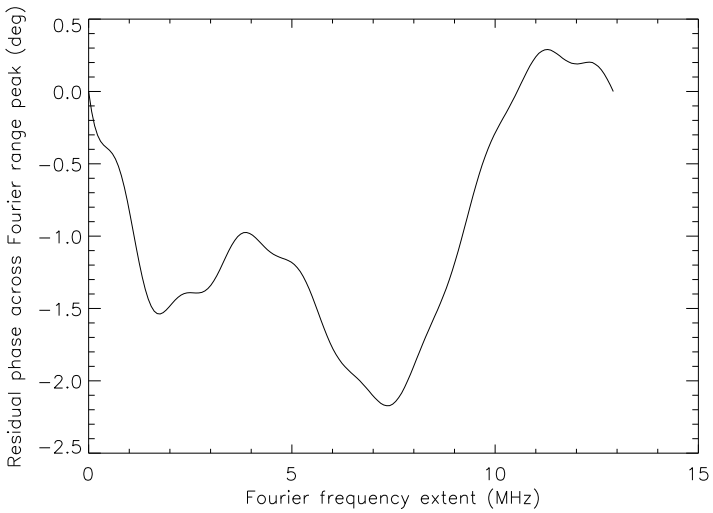

Figure 4.11: The quadratic- and higher order range Fourier phase error for the extended processor with 30 km reference range and 31 km target.

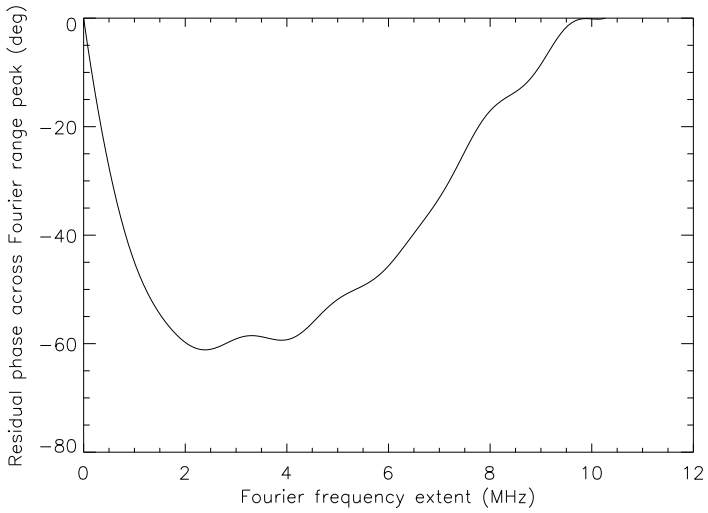

Figure 4.12: The quadratic- and higher order range Fourier phase error for the standard range-Doppler processor and 31 km target.

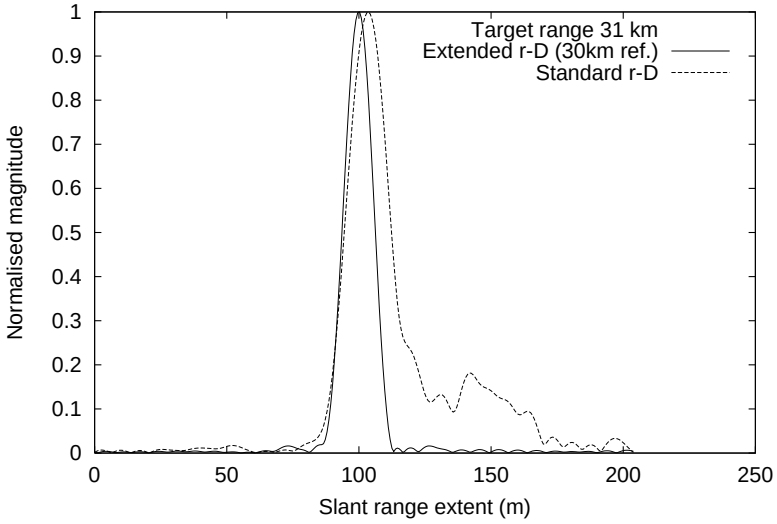

Figure 4.13: The magnitude of the range profile after processing the 31 km target with the extended algorithm (30 km reference) and the standard range-Doppler algorithm.

4.5 Computational Requirements

A comparison of the computational requirements of the extended algorithm over conventional range-Doppler processing is discussed in the sections below. The establishment of meaningful comparative timing measures for the two algorithms remains an area of future work.

4.5.1 Input Data Range Compressed

In the simulations described in this chapter where the input data had already been range compressed, the extended algorithm involves significantly more computation than the conventional range-Doppler processing as described in Section 4.2.1. If we assume that the computation involved in the inverse FFT step (Step F) of the extended algorithm is of similar order as the computation required for the azimuth FFT with the standard algorithm, it is possible to make some comments about relative processing loads.

In this case, the extra steps required by the extended algorithm were to perform three extra corner turn operations (between Steps A and B, C and D, and E and F), a range- and azimuth Fourier transform on the zero-padded 2-D reference function, a range- and azimuth Fourier transform on the data, and a multiply operation (Step E).

This sounds like a lot of extra work for the processor, but the situation is not as bad as it appears at first glance.

To improve efficiency, the reference functions for both the standard- and extended processors should be precomputed and stored. This eliminates one of the corner turns and Steps A and B from the extended processor's load. In addition, the corner turn operations should be eliminated if there is sufficient processing RAM available (not the case for the candidate with these tests), but this would require more care with reducing levels of pointer arithmetic.

Thus, for the case of range compressed input data, the best case comparison scenario for the extended processor over standard range-Doppler processing is where the reference functions are precomputed and sufficient RAM is available to avoid explicit corner turn operations. In that case, in addition to the operations performed by the standard processor, the extended processor requires only a range FFT, an azimuth FFT and a 2-D multiply operation.

4.5.2 Input Data Range Uncompressed

For the case of the input data requiring range compression, the computational requirements for the extended- and standard range-Doppler processors are much closer than for the case where the input data are already range compressed. We consider the case where the following assumptions are true (not unrealistic for many systems and processing hardware):

- the data are range uncompressed
- the reference functions are precomputed and stored
- the explicit corner turn operations are avoided by using a processor with large amounts of RAM and pointer arithmetic is kept to a minimum

In this case, the extended processor and standard processor require about the same amount of computation. The reason for this is that for standard processing an extra range FFT, multiply and range inverse FFT are required for the range compression step. However, no extra computation is required for the extended processor as the range compression step may be incorporated into the initial 2-D reference function.

In the case that the processor does not have sufficient RAM, but that the data are range uncompressed and the reference functions are precomputed, the extra load

required by the extended processor over the standard processor would only be two explicit corner turn operations.

4.6 Additional Considerations

4.6.1 Sidelobe Suppression

In the simulations presented here, the input data to the processors was already range compressed with Hamming weighting applied to the range reference function to reduce range sidelobes. The 2-D reference function was constructed as the range compressed return of a point target at the reference range where a rectangular weighting was applied during the reference function range compression. A rectangular weighting was applied to this 2-D reference so as not to apply the Hamming weighting twice to the data in range.

In azimuth, it is best to use a rectangular weighting for the 2-D reference function as any sidelobe reduction weighting may be applied later in the residual azimuth reference function of Step G. Also, the 2-D reference function needs to be as long in azimuth as the longest synthetic aperture length required for the azimuth resolution. Thus, to apply one azimuth weighting to the 2-D function and then to use different azimuth lengths of the corrected signal would give inconsistent results for different ranges.

For the processing results of this chapter, the 2-D function was generated with the radar simulator. The simulator includes a fourth power range dependence thus, in effect, some azimuth weighting is applied to the 2-D reference function. However, this effect is not large at the simulated target ranges for the range curvature processed - the voltage magnitude at the edges of the processed synthetic aperture is 93 percent of the closest approach value for the two targets. Note that, as already mentioned, for the results presented in this chapter, a rectangular weighting was applied to the residual azimuth reference functions in Step G (as well as in the standard range-Doppler processor).

4.6.2 Multilook

The standard range-Doppler azimuth compression stage is really equivalent to the residual focusing stage of the extended algorithm (Step G), except that the reference range for the standard algorithm is zero. Note, however, that the candidate did imple-

ment Step G slightly differently than for the standard algorithm in that the current extended implementation (Step G) accepts the data range line by range line rather than azimuth line by azimuth line.

The standard range-Doppler processing options during azimuth compression are still available during the residual focusing stage (Step G). For example, multilook speckle reduction through splitting up of the azimuth frequency spectrum is efficiently implemented during Step G, as for conventional range-Doppler processing.

4.6.3 Implementation with Multiple 2-D Reference Functions

It is conceivable that for some wide swath, high resolution, low frequency applications, even the improved accuracy of the extended range-Doppler processor would prove insufficient across the whole swath. In that case, to improve accuracy, it would be necessary to make use of several initial 2-D reference functions matched to different ranges across the swath. The extreme case, though very computationally intensive and hence not a practical solution with current processing hardware, would be to update the 2-D reference function for every range bin.

The practical implementation of a scheme using more than one 2-D reference function would naturally complicate the processor design and may lead to some undesirable phase discontinuity effects across the update boundaries (this requires further investigation). The simplest method of implementing multiple 2-D reference functions would be as follows:

- Decide on how many updates are required.
- Process each block of range bins fully with a reference range matched to the mid range of each block. Note that use would have to be made of overlapping range blocks of input data due to the range curvature.
- Combine all the output images (one from each range block) into one large, full swath image.

4.6.4 Implementation for Squinted SAR Geometries

The work presented in this chapter (and thesis in general) has focused on airborne SAR geometries with zero Doppler centroid (no beam squint). However, Raney and

Vachon [52] applied the same basic algorithm to the case of a narrow beam SAR (3.6 deg) with severe squint (45 deg).

Implementation with a squinted signal is achieved through a selection of the 2-D reference function to match the squinted SAR signal (at mid range). As currently implemented for this thesis, the residual focusing stage in the range-Doppler domain (Step G) requires knowledge of the value of the reference range. If, in addition, the squint angle (or Doppler centroid) were passed to this processing module, the residual correction for a squinted geometry could be calculated.

4.6.5 Application to Scenes Without Large Range Curvature Variation

Although this has not been investigated in detail by the candidate, it is conceivable that there are certain SAR geometries where the range curvature does not vary significantly relative to the range resolution across the swath, where, once the initial reference function has removed the range curvature for the reference range, no further range curvature correction is required for the full scene. In this case, the task of the residual range-Doppler correction routine (Step G) is greatly simplified in that no range curvature interpolation is required at all. In this case, all that is required of Step G is the residual phase correction multiplication in order to focus the image in azimuth.

4.7 Summary

In this chapter, an extension to the range-Doppler algorithm is shown to improve focusing performance in the presence of severe range curvature. Such severe range curvature is typically experienced in high resolution SAR azimuth processing at low frequencies, though is not limited to low frequencies.

The idea for the extension was suggested to the candidate by Jin, one of the introducers of secondary range compression (Jin and Wu [48]), in a private discussion [1]. After completion of the extended processor development and the work presented in this chapter, the candidate became aware of the contents of a publication by Raney and Vachon [52] in which the main steps of the extended processor had been described. Raney and Vachon, however, while noting that their algorithm would be applicable to the severe range curvature case, applied the approach to the case of a narrow beam

SAR with large squint. In addition, the implementation described in [52] differs in some respects from that described in this chapter (e.g. the method of generating the reference function in the 2-D frequency domain).

The algorithm implemented by the candidate has been successfully tested using simulated data from an airborne, stripmap SAR system operating at 141 MHz with a zero Doppler centroid of the beam. The tests show a clear processing performance improvement with the new range-Doppler extension over standard range-Doppler processing.

The extended algorithm is very flexible in that it is applicable to both airborne and spaceborne data, range compressed and range uncompresed signals, and to cases of both severe range walk and severe range curvature (also noted by Raney and Vachon [52]).

The extended algorithm, as described here, has a straightforward implementation to those familiar with range-Doppler processing, but does involve more computational steps than the standard approach when applied to range compressed signals. If, however, the input data are range uncompressed, the initial 2-D reference function is precomputed, large amounts of RAM are available, and pointer arithmetic minimized, the extended algorithm requires about the same computational load as the standard range-Doppler approach.

Future work with the extended range-Doppler algorithm should include a quantitative and mathematical comparison of processing accuracy and computational complexity with other approaches such as the range migration and chirp scaling algorithms when applied to the severe range curvature case. In addition, work is required in the development of more representative 2-D focusing performance measures.

Chapter 5

Motion Compensation

5.1 Introduction

In any airborne system, motion compensation is an important step in the processing and must be performed accurately if the processed image is not to suffer from distortion effects. Motion compensation for airborne systems is not a straightforward subject, as there are both practical- and theoretical difficulties to be considered. Some early theoretical work on the effects of phase errors on SAR imagery was performed by Brown [13]. In addition, Carrara *et al.* [17] (pp. 203-243) discuss the effects of high and low frequency phase errros for airborne SAR. For this reason, a theoretical treatment of phase errors is not presented here. Instead, the focus in this chapter is on the practical implementation issues and the associated mathematics applicable to the wide beam, airborne stripmap case. For reasons discussed in Chapter 2, motion compensation for beam squint (i.e. range walk correction) is not addressed here. Motion compensation for airborne interferometric SAR with small processed azimuth beamwidths is described by Madsen [45] and Stevens [60]. In this chapter, the motion compensation discussion focuses on two aspects:

1. the accurate reconstruction of the actual flight path from the inertial- and navigational measurements taken on board the aircraft.

2. the implementation of the correction required given knowledge of the flight path.

Almost all discussion of motion compensation in the literature is restricted to the narrow beam SAR case. For a wide beam system, the azimuth dependence of the motion compensation becomes significant and must be addressed. A technique for

dealing with the wide beam case, developed by researchers at ERIM, is discussed in Section 5.5.1. In addition, for comparison and completeness, the more conventional narrow beam implementation is discussed in Section 5.4.

The work described in this chapter is the candidate's own, and is largely based on the candidate's practical experience in developing and implementing motion compensation algorithms for three systems: the SASAR VHF sensor and the ESAR P-band and C-band sensors. In this chapter, two strategies for reconstruction of the flight path from inertial sensor data are presented. In Section 5.6, a strategy developed and implemented by the candidate for the processing of the SASAR VHF data is discussed. In Section 5.8, a strategy, developed by Buckreuss at the DLR [15] and implemented by the candidate for the processing of the ESAR P- and C-band data, is discussed. The motion compensation algorithm of Carrara, Tummala and Goodman [18] for wide beam, stripmap SAR, based on spotlight SAR processing techniques, is discussed in Section 5.5.1.

5.2 Assumptions

The following assumptions are made in this chapter:

- Airborne, stripmap SAR with flat earth approximation used.
- Modest relative pulse bandwidths (i.e. not wide-band systems). "Relative pulse bandwidth" is the ratio of the pulse bandwidth to the centre frequency.
- Stop-start approximation valid (Barber [9]).
- Stationary scatterers with uniform amplitude and phase response over azimuth angles (Axelsson [6]).
- The inertial sensor data have already been corrected for the lever arm distance to the phase centre of the antenna (or the correction required is negligible).
- Azimuth beamwidth sufficiently wide that only the portion of the azimuth signal symmetrical about zero Doppler is processed in azimuth (i.e. no range walk or squint correction required) and the elevation beamwidth sufficiently wide that the full processed swath width is always illuminated.

- Motion compensation is performed on range compressed signals before azimuth compression (Figure 2.7). Real-time motion compensation is not addressed.

- To simplify the motion compensation implementation, the PRF should be slaved to the component of the ground speed in the direction of the nominal flight track (as shown in Figure 5.1). This ensures that the ground spacing of the pulses in the direction of the nominal flight track is constant. The SASAR VHF sensor was designed to include this feature, but slaving of the PRF was not enabled for the data collected thus far. In the analysis of this chapter, slaving of the PRF to the ground speed is not assumed.

Taken together, the wide beam and lever arm assumptions imply that the correction for angular orientation effects is not discussed in this chapter. Note that, for all reasonable platform flight orientations, the angular orientation for the SASAR VHF sensor does not require any correction.

5.3 Motion Compensation Requirement

For side-looking, airborne, stripmap SAR systems, the ideal flight path is a straight line at constant height, parallel to the desired swath to be imaged. The term "nominal flight path" is used here to describe the ideal, straight flight path. In practice, the nominal flight path is never achieved. Deviations from the ideal path are caused by a number of factors including atmospheric turbulence, high altitude winds, navigational error and aircraft vibration.

For accurate SAR azimuth focusing, the target phase is the most important parameter. The requirement here is that the positional deviations be corrected to within a small fraction of the wavelength. Quite what this figure should be is dependent on the application at hand. For example, Carrara *et al.* [18] state that for the imaging requirements of the P3 ultra-wideband SAR, the acceptable positional motion error is $\lambda/16$ for low frequency motion and $\lambda/128$ for high frequency motion. For other applications, the requirements may not be quite as stringent. For example, Raney [32] (pg. 19) states that the positional error should be better than about $\lambda/10$.

Due to the wavelength dependence on the motion compensation requirement, high frequency motion errors such as aircraft vibration of a given small amplitude are more likely to degrade focusing performance for high frequency SAR systems than for low

frequency SAR systems. Thus, in this regard, operation at long wavelengths is an advantage.

Next, we consider long term drift effects: Equation 2.23 of Chapter 2 shows that, for a target at a given zero Doppler range R_0, the synthetic aperture length L required to achieve a given azimuth resolution δx_{res} increases with wavelength according to

$$L = R_0 \left(\frac{4\delta x_{res}^2}{\lambda^2 K_{az\_win}^2} - \frac{1}{4} \right)^{-\frac{1}{2}} \tag{5.1}$$

where λ is the wavelength, and K_{az_win} is the azimuth window broadening factor. An analysis of Equation 5.1, shows that, unless processing over a very large azimuth angular extent, the synthetic aperture length is linearly dependent on the wavelength to a reasonable approximation (for a given R_0, δx_{res} and K_{az_win}). Any practical accelerometer-based inertial measurement unit (IMU) will suffer to some degree from long term drifts of the instruments. For SAR systems, these long term drifts become important over the integration times over the synthetic aperture.

Any bias in an accelerometer will, after double integration, map to a quadratic instrument positional error. Thus, as the synthetic aperture length and motion compensation requirement ($\lambda/10$, say) are (approximately) linear in wavelength, the long synthetic apertures required at low frequency will be more susceptible to the quadratic instrument positional errors than at high frequencies (for a given R_0, δx_{res} and K_{az_win}).

Note that, if the positional output drift of the inertial unit could be restricted to be linear over the length of the synthetic aperture, then there is no wavelength dependence on the linear positional drift rate accuracy requirement of the inertial sensor (to a reasonable approximation).

As an example of a low frequency system, consider the following: For a 141 MHz system with K_{az_win} of 1.30, R_0 of 20 km, and single look azimuth resolution δx_{res} of 3 m, the synthetic aperture length (from Equation 5.1) is 14.229 km. For a ground speed of 90 metres per second, the time taken to fly the synthetic aperture is 158 seconds (2.6 minutes). Thus, for the above scenario, to maintain positional accuracy to better than about $\lambda/10$ (of the order of 20 centimetres) over the synthetic aperture, we require that the positional error of the IMU output be better than 20 centimetres in 2.6 minutes, not easily achievable.

5.4 Narrow Beam Implementation - Motion Compensation to a Line

In most airborne, stripmap SAR systems, the strategy employed for motion compensation is to correct the data to a line at mid swath. This line is referred to here as the ground reference track and is defined here as the line parallel to the nominal flight track and positioned on the ground at mid range of the nominal swath. The ground reference track is shown in a top view of the motion compensation geometry in Figure 5.1. Motion compensation to a line is applicable to systems with relatively narrow processed azimuth beamwidths where the angular dependence of the motion compensation correction is small. A strategy for dealing with the wide beam case is discussed in Section 5.5.1. All the candidate's practical experience of implementing motion compensation has used motion compensation to a line. This includes processing of the SASAR VHF data to modest azimuth resolution, and processing of the P- and C-band ESAR data.

A reasonable choice for the nominal flight track for an airborne system (using the flat earth approximation) is the line at the average aircraft altitude for the scene and joining the start and end latitude and longitude positions of the data take. This nominal flight track has been used in the SASAR processing.

If the flight deviation from the nominal flight track results in a range error for a particular range line of ΔR, the range line data require a correctional range shift of ΔR. In addition, and more important, is the phase correction required for the range line, given in radians by (from Equation 2.22)

$$\Delta\varphi = \frac{4\pi}{\lambda}\Delta R \tag{5.2}$$

For range-Doppler processing, the motion compensation is conveniently performed immediately after the range compression stage (as in Figure 2.7). In this case, the range shift ΔR is easily accomplished using an interpolator (an 8-pt Shannon interpolation was used for the imagery presented in this thesis). The phase shift $\Delta\varphi$ is simply implemented as a complex multiply.

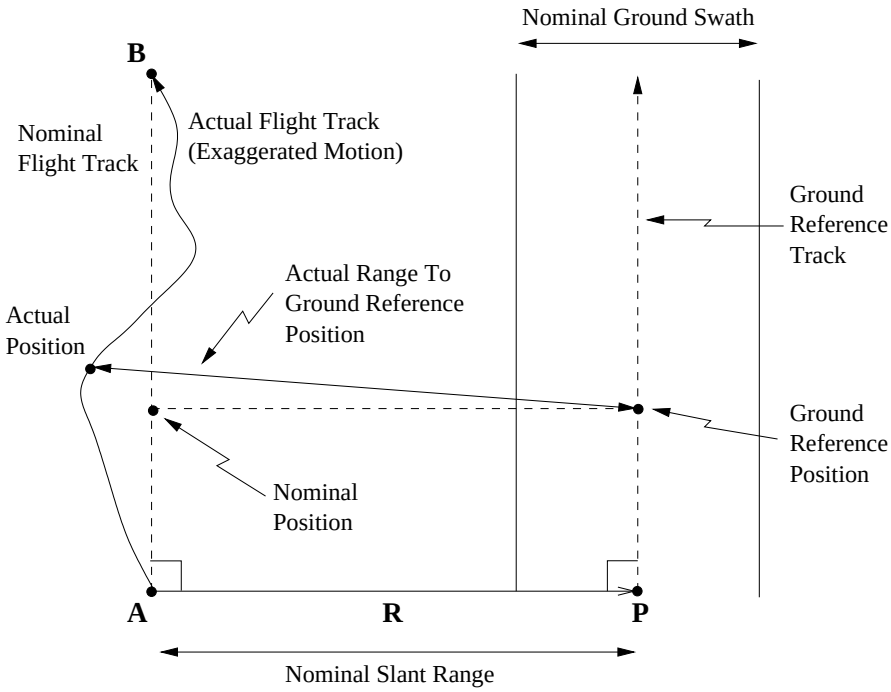

Figure 5.1: Geometry for motion compensation to a line (the ground reference track) commonly used in airborne stripmap SAR systems.

5.4.1 A Note on Motion Compensation Range Updates

The motion compensation correction required is not only a function of slow-time and azimuth angular position, but is also a function of range. For systems with small swath widths or with the distance to start of swath large relative to the aircraft height, the range dependence is small and is often neglected.

If the motion compensation is to be updated with range by blocking the data, the practical experience of the candidate is that care must be exercised as the phase discontinuities at the update ranges can interfere with the azimuth focusing. This becomes particularly noticeable where interpolation operations such as used in range curvature correction are performed. The interpolation across the phase discontinuities results in incorrect phase information and shows up as dark azimuth lines across the focused image, spaced by the update interval of the range dependent motion compensation.

5.4.2 A Note on Motion Compensation Frequency Dependence

Although this thesis is restricted to modest relative range bandwidths, it is instructive to consider the origin of the motion compensation phase term (Equation 5.2). This

analysis assists in understanding whether frequency dependent motion compensation is required.

Consider a transmitted waveform $s_{tx}(t)$, a baseband pulse modulation $p(t)$ and carrier (centre) frequency f_0.

$$s_{tx}(t) = p(t) \exp(j2\pi f_0 t) \tag{5.3}$$

The received signal $s_{rx}(t)$ from a single point target is simply a time delayed version of the transmitted signal.

$$s_{rx}(t) = p(t - t_0) \exp(j2\pi f_0 (t - t_0)) \tag{5.4}$$

After IQ demodulation, the baseband returned signal $s_{bb}(t)$ is simply given by

$$\begin{aligned} s_{bb}(t) &= s_{rx}(t) \exp(-j2\pi f_0 t) \\ &= p(t - t_0) \exp(-j2\pi f_0 t_0) \end{aligned} \tag{5.5}$$

From Equation 5.5, it is clear that for some displacement of the aircraft from its nominal position, the returned signal at baseband will simply include an additional time shift of the baseband transmit pulse modulation and an additional phase shift matched to the carrier frequency. Thus, no motion compensation frequency dependence is required. Note that motion compensation frequency dependence would be required for a wideband, stepped frequency system, where different frequencies are used in the mixing to baseband for each stepped pulse.

5.4.3 A Note on the Flat Earth Approximation

Figure 5.2 shows how the flat earth approximation results in a height error Δh over the synthetic aperture length L. In this figure R_e is the radius of the earth and h is the height of the aircraft above the ground. Note that both L and h have been exaggerated in this figure. From the geometry on the left side of Figure 5.2, the height error may be shown to be

$$\Delta h = (R_e + h) \left(1 - \cos\left(\frac{L/2}{R_e + h}\right)\right) \tag{5.6}$$

From the geometry on the right side of Figure 5.2, the range error ΔR resulting from the height error Δh may be shown to be (with angle γ as shown)

$$\Delta R \approx \Delta h \sin\gamma \tag{5.7}$$

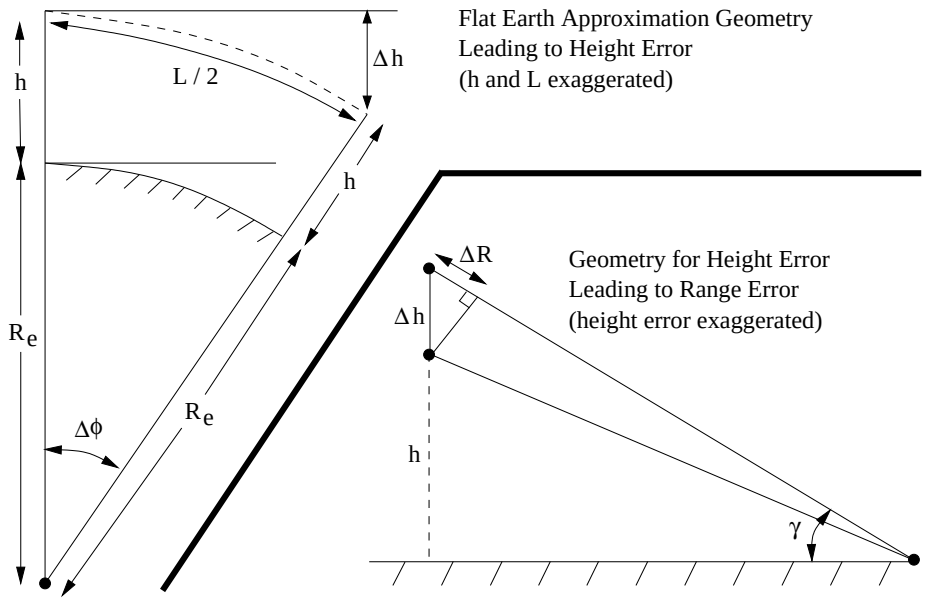

Figure 5.2: The flat earth approximation resulting in a height error over the synthetic aperture.

For the SASAR system, with a target at 10 km slant range, and processed to 4 m in azimuth, the synthetic aperture length is approximately 2.7 km. From Equation 5.6, the height error from the flat earth approximation is approximately 14 cm. For targets at 5 km and 20 km slant range, the height error is approximately 4 cm and 57 cm, respectively.

From Equation 5.7, the range error is more severe for near range targets than for targets at far range for a given height error. However, from Equation 5.6, the height error is larger for the longer synthetic apertures required at far range. Taken together, Equations 5.6 and 5.7 show that for the SASAR parameters above, the range error for the 20 km target is approximately 9 cm while that for the 5 km target is approximately 2 cm. Thus, for the SASAR parameters mentioned above, the flat earth approximation error is not significant.

Note that it is relatively straightforward to implement a correction factor for the flat earth approximation should this be necessary for a given set of system parameters.

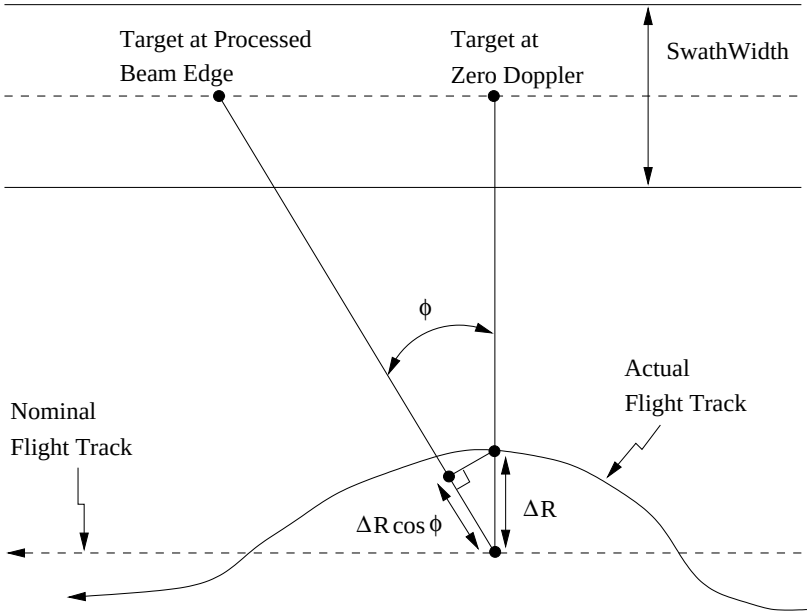

Figure 5.3: The geometry leading to motion compensation angular dependence.

5.5 Wide Beam Implementation

The figures and mathematical analysis presented in this section, taken from Carrara *et al.* [18], assume that the PRF has been slaved to the component of the ground speed along the nominal flight direction. Note that the "spotlike" motion compensation technique described in Section 5.5.1 does not, however, require that slaving of the PRF be applied.

For systems with wide processed azimuth beamwidths, the angular dependence of the motion compensation correction should not be neglected. The geometry leading to the angular dependence is shown in Figure 5.3.

As shown, a target at the centre of the beam requires a motion correction ΔR, but a target at an azimuth angle ϕ the processed beam requires a correction of $\Delta R \cos\phi$. Thus, after the conventional approach of motion compensation to a line, the average residual phase error is comparable for all targets in the scene, and the residual phase error is given in radians [18] as

$$\Delta\varphi_e = \frac{4\pi\Delta R}{\lambda}(1 - \cos\phi) \tag{5.8}$$

Rearranging the azimuth resolution expression (Equation 2.16), we obtain an equa-

tion for calculating the processed half angular beamwidth as

$$\phi = \arcsin\left(\frac{\lambda}{4\delta x_{res}} K_{az\_win}\right) \tag{5.9}$$

As an example, for a 141 MHz system with K_{az_win} of 1.30 and single look azimuth resolution δx_{res} of 3 metres, the processed half angular beamwidth required is calculated from Equation 5.9 as $\phi = 13.3$ degrees. Thus, for a ΔR of 10 metres, the residual phase error at the edges of the processed beam is given by Equation 5.8 as $\Delta\varphi_e = 91$ degrees. This is an appreciable error. Increasing the azimuth resolution requirement to $\delta x_{res} = 1$ metre for the same system results in a processed half beamwidth required of $\phi = 43.8$ degrees and a residual phase error of $\Delta\varphi_e = 941$ degrees! Decreasing the resolution requirement to $\delta x_{res} = 5$ metres, yields $\phi = 8.0$ degrees and $\Delta\varphi_e = 33$ degrees, an acceptable error using the $\lambda/10$ positional error motion compensation requirement (which translates to a phase error of 72 degrees from Equation 5.2). Note, however, that $\Delta\varphi_e$ is linear in ΔR, and, at parts of a long synthetic aperture, ΔR may well exceed 10 metres in practice.

5.5.1 "Spotlike" Motion Compensation

Now that an expression has been presented for the residual phase error with the motion compensation to a line technique and the relevance established for a wide beam VHF system, it is appropriate to introduce a motion compensation strategy for reducing this error. One might be tempted to consider implementing such a residual correction in the range-Doppler domain, after applying motion compensation to a line (to ensure along track coherence, to first order). However, this approach is flawed in that the motion compensation angular dependence also varies with slow-time, not available in the range-Doppler domain (Goodman [4]).

Carrara, Tummala and Goodman at ERIM [27][18], one of the organizations involved in the DARPA/ERIM/NAWC P3 ultra-wideband SAR, which operates from $215 - 900$ MHz with a processed azimuth beamwidth of up to 33 degrees, have developed a strategy for dealing with the wide beam case which they term "spotlike" motion compensation as it is based on motion compensation for spotlight SAR systems. The spotlike motion compensation technique is discussed here as it is relevant to SAR processing with wide azimuth beamwidths. This technique has not been implemented by the candidate to date.

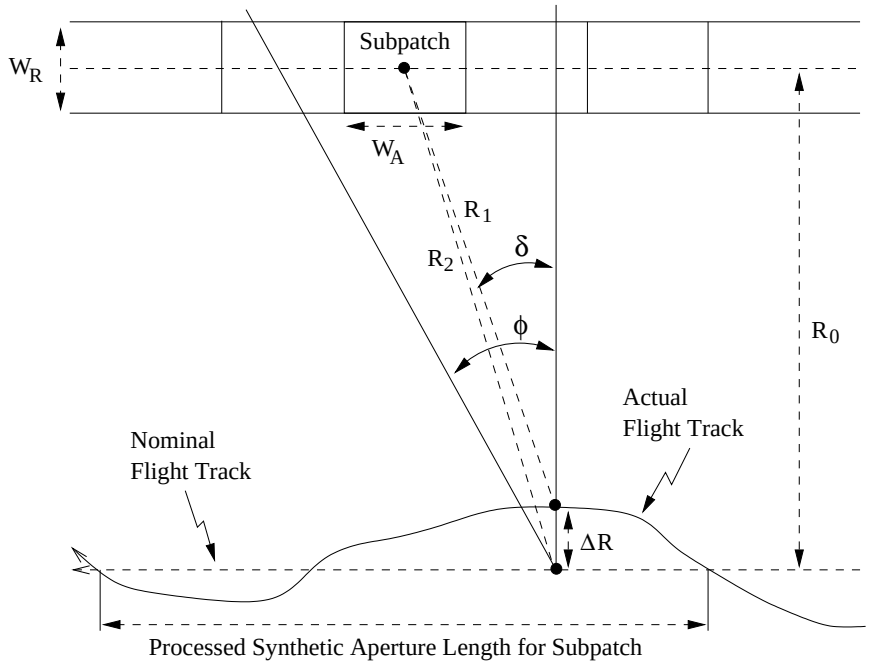

Figure 5.4: The ERIM "spotlike" motion compensation approach by dividing the imaged swath into subpatches and processing each separately using motion compensation to a point.

The basic idea is to divide the imaged swath into azimuth subpatches as shown in Figure 5.4 and to apply motion compensation to a point at the centre of each subpatch, rather than to a line. The process is less efficient than motion compensation to a line as each subpatch requires a different set of motion compensation corrections and the processed synthetic aperture length (shown at the bottom of Figure 5.4) is longer than the subpatch azimuth extent.

As shown in Figure 5.4, if the motion compensation makes use of the range R_1 to the centre point of the subpatch, this point will be corrected to have constant phase with points away from the centre point with some residual time-varying phase. If a stripmap SAR processing algorithm such as the range migration (or extended range-Doppler) approach is to be used to focus the image, an azimuth chirp is expected of the input data. Thus, this chirp must be reinstated before processing. However, as pointed out by Carrara *et al.* [18], if $(R_1 - R_2)$ is used as the correction, then motion compensation to a point is achieved without removing the azimuth chirp.

Carrara *et al.* [18] state that the maximum residual phase $\Delta\varphi_e$ for the spotlike

motion compensation varies over the scene from zero at the centre of the subpatch to a maximum value approximately given by

$$\Delta\varphi_e \approx \frac{\pi}{2\lambda} \frac{\Delta R \cdot W_A^2}{\left(R_0 - \frac{1}{2}W_R\right)^2} (\cos\delta)^3 \tag{5.10}$$

for a target at near range and an azimuth edge of the swath. W_A, W_R, R_0, ΔR and δ are as shown in Figure 5.4 with $-\phi \leq \delta \leq \phi$. Note that the maximum residual phase error is largest when $\delta = 0$ (i.e. when the subpatch centre is at zero Doppler). Note also that the maximum residual phase error is approximately dependent on the square of the subpatch azimuth extent W_A. Thus, the error may be reduced by reducing W_A.

As an example, consider once again the 141 MHz system with K_{az_win} of 1.30 and single look azimuth resolution δx_{res} of 3 metres for the case where $R_0 = 10$ km, $\Delta R = 10$ m, and $\delta = 0$ deg. In this case, if $W_R = 7$ km and $W_A = 2$ km, 4 km, and 8 km, Equation 5.10 yields $\Delta\varphi_e = 40$ deg, 160 deg, and 640 deg, respectively.

As mentioned, the spotlike motion compensation has not been implemented by the candidate to date. In the following sections, motion compensation techniques developed for the candidate's processing of the SASAR VHF and E-SAR data are presented.

5.6 Motion Compensation Calculation using Latitude, Longitude and Ellipsoidal Height Measurements

The objective of this section is to calculate the equations of the nominal flight track and the ground reference track in 3-D Cartesian coordinates given inertial data in the form of (ψ, η, h) where ψ is the latitude, η is the longitude and h is the ellipsoidal height (the height above the WGS 84 ellipsoid model of the earth). The nominal flight track and ground reference track are as shown in Figure 5.1. The technique described in this section has been developed by the candidate for the SASAR VHF processing.

The equations derived in this section are of general applicability to airborne SAR with a flat earth approximation and with inertial data in the form of (ψ, η, h). Although not true in practice, it may be assumed for the purposes of this derivation that the (ψ, η, h) output from the inertial sensor is perfectly accurate. In addition, it is convenient to assume that a (ψ, η, h) triple exists for each range line processed. In practice, interpolation is required between IMU output data points.

5.6.1 Conversion to Earth-Centred 3-D Cartesian Coordinates

To start, it is necessary to convert the (ψ, η, h) values to 3-D Cartesian coordinates. For a 3-D Cartesian system with the origin at the centre of the ellipsoid, the x axis emerging at the intersection of the Greenwich Meridian and the Equator (note x not azimuth distance in this section), the z axis emerging at the North pole, and the y axis orthogonal to the x- and z axes in a right-handed coordinate system, the following conversion applies (Merry [47]):

$$\begin{bmatrix} x \\ y \\ z \end{bmatrix} = \begin{bmatrix} (N+h)\cos\psi\cos\eta \\ (N+h)\cos\psi\sin\eta \\ \left(N\cdot\left(1-e^2\right)+h\right)\sin\psi \end{bmatrix} \tag{5.11}$$

where

$$N = \frac{a}{\sqrt{1-e^2\sin^2\psi}} \tag{5.12}$$

and

$$e^2 = \frac{a^2-b^2}{a^2} \tag{5.13}$$

with:

- a as the semi-major axis length (6378137.000 m for the WGS 84 ellipsoid)
- b as the semi-minor axis length (6356752.314 m for the WGS 84 ellipsoid)

5.6.2 Calculation of the Start Point of the Ground Reference Track

With the conversion to a 3-D earth-centred Cartesian system given by Equation 5.11, the following are known in the Cartesian system:

- The start and end points of the nominal flight track and hence the equation of the straight line joining these two points. In this analysis, the start point of the nominal track is taken as the first data point processed. The last point of the reference track is taken as the point with the same ellipsoidal height as the first point, but with the latitude and longitude of the last data point processed.
- The gradient of the line in three dimensions marking out the ground reference track. This is the same as the gradient of the nominal flight track, since the two are parallel.

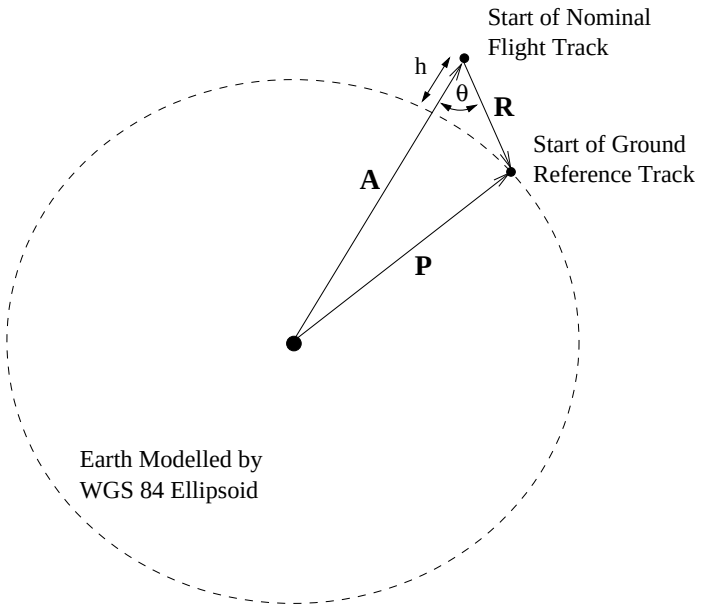

Figure 5.5: The vector geometry for finding the start point of the ground reference track in earth-centred 3-D cartesian coordinates.

- The actual position of the radar antenna for each range line in the 3-D Cartesian coordinates.
- The average ground speed along the nominal flight track.

Thus, the only remaining difficult part of the motion compensation calculation is to find the start of the ground reference track in the 3-D Cartesian system. Once this is known, then the positional error for each range line may be calculated easily as the difference in slant range from the actual- and nominal positions to the ground track reference point as shown in Figure 5.1. To find the start of the ground reference track we proceed with the vector definitions below. In this section the vector quantities are shown in bold type (refer to Figures 5.1 and 5.5).

- **A** - the vector from the origin to the start of the reference flight track (known)
- **B** - the vector from the origin to the end of the reference flight track (known)
- **P** - the vector from the origin to the start of the ground reference track (unknown - this is what we want to find)
- **R** - the vector from the start of the reference flight track to the start of the reference ground track (unknown, but $|\mathbf{R}|$ is known)

- **V** - a vector in the direction of the nominal flight track (known since $\mathbf{V} = (\mathbf{B} - \mathbf{A})$ and **B** and **A** are known)

Using the above vector definitions and knowledge of the side-looking geometry, the following vector equations are valid (with angle θ as shown in Figure 5.5):

$$\begin{aligned} \mathbf{P} &= \mathbf{A} + \mathbf{R} && (5.14) \\ \mathbf{R} \cdot \mathbf{V} &= \mathbf{0} && (5.15) \\ \mathbf{R} \cdot \mathbf{A} &= |\mathbf{R}|\,|\mathbf{A}| \cos(\pi - \theta) && (5.16) \end{aligned}$$

In addition, the following vector relations involving the cross- and dot vector products are valid:

$$\begin{aligned} &(\mathbf{A} \times \mathbf{R}) \cdot \mathbf{V} > \mathbf{0} \text{ (for right-looking antenna)} \\ &(\mathbf{A} \times \mathbf{R}) \cdot \mathbf{V} < \mathbf{0} \text{ (for left-looking antenna)} \end{aligned} \tag{5.17}$$

If we denote the known constants $|\mathbf{R}|$ as t (t not time here) and $|\mathbf{R}|\,|\mathbf{A}| \cos(\pi - \theta)$ as u, and in addition, make the following definitions

$$\begin{aligned} \mathbf{P} &= (d, e, f) \\ \mathbf{A} &= (h, k, m) \\ \mathbf{R} &= (n, o, p) \\ \mathbf{V} &= (q, r, s) \end{aligned} \tag{5.18}$$

then, using the Maple symbolic manipulation software to solve the following vector equations (based on the known magnitude of **R**, Equations 5.15 and 5.16)

$$\begin{aligned} \sqrt{\mathbf{R} \cdot \mathbf{R}} &= t \\ \mathbf{R} \cdot \mathbf{V} &= 0 \\ \mathbf{R} \cdot \mathbf{A} &= u \end{aligned} \tag{5.19}$$

the solution is:

$$\begin{aligned} p &= \rho \\ o &= -\tfrac{h\rho s - \rho m q + u q}{h r - q k} \\ n &= -\tfrac{r\rho m - r u - \rho s k}{h r - q k} \end{aligned} \tag{5.20}$$

where ρ is a root of the quadratic $aX^2 + bX + c$ where the coefficients are given by

$$\begin{aligned} a &= s^2k^2 + m^2q^2 + q^2k^2 - 2rsmk + r^2m^2 + h^2s^2 - 2hsmq + h^2r^2 - 2hrqk \\ b &= 2rsuk + 2hsuq - 2umr^2 - 2uq^2m \\ c &= r^2u^2 + u^2q^2 - t^2h^2r^2 + 2t^2qhrk - t^2q^2k^2 \end{aligned} \tag{5.21}$$

Thus, solving for the roots of the quadratic with coefficients given by Equation 5.21, and then evaluating which root gives the expected antenna direction from Equation 5.17, yields $\mathbf{R}$ and, since $\mathbf{A}$ is known, we can find $\mathbf{P}$ from $\mathbf{P} = \mathbf{A} + \mathbf{R}$ (Equation 5.14). This is what we set out to achieve.

5.7 Practical Experience with the FIN3110 IMU and SASAR VHF Data

The analysis presented in Section 5.6 originates from the candidate's motion compensation processing for the SASAR VHF sensor. The inertial measurement unit (IMU) used for the first radiating flights was a FIN 3110 unit made by GEC-Marconi Defence Systems [62] and on loan to the project from Kentron, part of the South African Denel Group. The output data from this inertial unit is in the form of latitude ψ, longitude η and ellipsoidal height h so the techniques described in Section 5.6 apply.

Excluding angular motion data sets, three main data sets available from the FIN 3110 unit (with associated problems listed below for SAR motion compensation) were:

- **GPS latitude, longitude and height** - suffers from the usual selective availability accuracy limitation of about 100 metres and thus is not suitable for SAR motion compensation.

- **Inertial latitude, longitude and height -** derived directly from the accelerometers and angular measurements and is thus smooth, but suffers from quadratic drift effects (from the double integration of the acceleration data).

- **Integrated latitude, longitude and height -** a combination of the inertial data and smoothed GPS data which looked initially to be the most useful of the data sets. However, on close inspection, it was found that the integrated data contained fluctuations of the order of a metre every second. This is too large for the $\lambda/10$ motion compensation accuracy requirement for the SASAR VHF sensor. The cause of the metre fluctuations in the integrated data is thought to be attempts by the IMU software to track the smoothed GPS data in order to maintain good absolute positional accuracy. Discussions with personnel at Kentron revealed that the metre fluctuations in the integrated data had not been noticed in their use of the FIN 3110. The reason for this is that Kentron

use had been restricted to applications where absolute accuracy of the order of a few tens of metres had been the requirement, not high relative accuracy over periods of a few minutes, as is required for low frequency SAR.

Use of the (smooth) inertial latitude, longitude, and height data set using the techniques described in Section 5.6 did result in a small, but visually noticeable, improvement in the SASAR VHF processing results. However, it soon became apparent that the bias and drift effects in this data set will themselves require correction for accurate focusing. Work is progressing in this area at the University of Cape Town through making use of a combination of the available data sets. Failure to find a satisfactory solution to the inertial data drift problem may result in the use of the technique of differential GPS for helping to remove these effects. Differential GPS does, however, pose practical difficulties in that it requires a ground fixed GPS unit within range for accurate positional measurements.

Due to these other, more pressing, motion data concerns, the motion compensation applied to the SASAR VHF data to date has not made use of the "spotlike" motion compensation technique discussed in Section 5.5.1 and only a single range update has been used.

5.8 Motion Compensation Calculation using Body-Axis Acceleration Measurements

In this section, the motion compensation technique applied by the candidate in the processing of ESAR P- and C-band data is discussed. This is of interest in that the inertial unit used in the ESAR system yields output data in the form of body axis accelerations, rather than the latitude, longitude and ellipsoidal height output of the sensor used for the SASAR system. The difference in the form of the output data leads to a different motion compensation strategy. As for the SASAR VHF sensor, the ESAR system has a sufficiently wide azimuth beamwidth such that range walk correction is not required in the standard processing modes.

The IMU motion data used in this section:

- The ground speed (forward velocity) of the aircraft.
- The height of the aircraft above the terrain.

- The positional deviations of the antenna phase centre in three dimensions at all points along the flight track. This also implies some choice for the nominal track (important for geocoding).

5.8.1 Motion Compensation Calculation

For the ESAR data, two inertial sensors were available: the Litef LTR-81 unit and the Honeywell YG1779 LASEREF unit. The LASEREF sensor provides parameters such as the instantaneous ground speed and drift angles. Initial attempts at motion compensation using data from this sensor did not improve the image. The biases and drifts in the data were not known and, after several unsuccessful attempts using this data, Stefan Buckreuss of the DLR [14], responsible for the ESAR motion compensation, was approached for assistance. Buckreuss confirmed that the LASEREF data was unreliable and suggested using the LTR-81 acceleration and heading data.

Heeding this advice, the biases and drifts were removed from the LTR-81 acceleration data by high-pass filtering before and after each integration (Buckreuss [15]). The high-pass filtering was implemented as a simple subtraction of the average value of the parameter. This approach removes the long term drifts, leaving only small amplitude, higher frequency motion. Differential GPS data must be used to correct for longer term motion, but this was not performed for the image presented (Section 5.8.2) due to the absence of corresponding GPS data for the available raw ESAR data. This high pass filtering technique has not been attempted to date with the SASAR data (the acceleration data was not recorded on the first SASAR flights). At SASAR frequencies, the improvement obtained by applying the high pass filtering technique is not expected to be as impressive as for the higher frequency ESAR data.

Figure 5.6 shows the motion compensation geometry used.

In the mathematical treatment of the motion compensation calculation given in this section, the following conventions and assumptions are used:

- The nominal track is taken as the straight path between the start and end latitude and longitude positions of the aircraft for the scene and with a constant altitude equal to the average aircraft altitude for the scene (calculated from inertial altitude measurements).

- The origin of the earth-fixed coordinate system is the point on the ground directly below the aircraft at the start of the track.

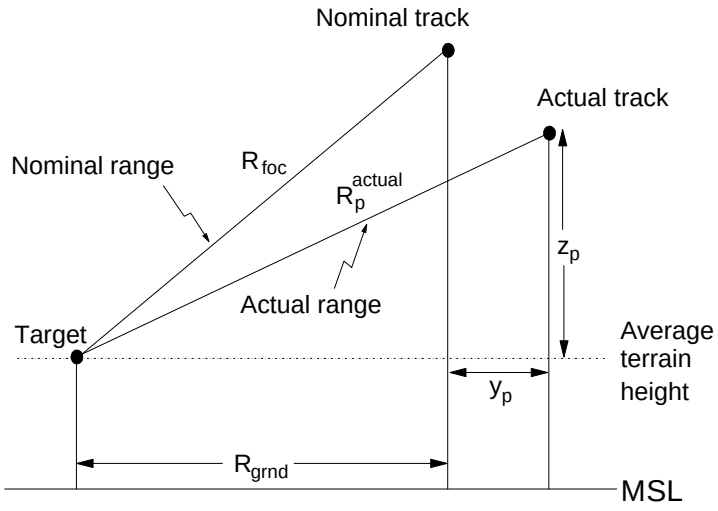

Figure 5.6: Off-track motion results in range deviations to the target.

- The x-axis of the earth-fixed coordinate system is oriented along the nominal flight path, positive y to the left of the nominal flight path and the z-axis vertically up.
- The antenna is left pointing.
- The terrain is assumed flat.
- The x, y and z accelerations used are assumed to be for the earth-fixed coordinate system as described. These earth-fixed accelerations may be derived from body-fixed accelerations by correcting for roll, pitch and yaw.

The steps involved in the motion error calculation are:

1. Calculation of the average height $\bar{h}$ above terrain from the average inertial altitude and terrain altitude.
2. Calculation of the average accelerations ($\bar{x}_{accel}$, $\bar{y}_{accel}$, $\bar{z}_{accel}$) for the scene.
3. Subtraction of the average accelerations and integration to find the x, y, and z velocities. The integration constants are removed in the next high-pass filtering operation and so may be taken as zero. Note that a very simple integration scheme is used. This proves sufficient, but a more sophisticated scheme may

easily be employed, if necessary. The velocity at PRI p is determined from the velocity at PRI $(p-1)$ and the acceleration at PRI p by

$$\begin{pmatrix} x_p^{vel} \\ y_p^{vel} \\ z_p^{vel} \end{pmatrix} = \begin{pmatrix} x_{p-1}^{vel} \\ y_{p-1}^{vel} \\ z_{p-1}^{vel} \end{pmatrix} + \frac{1}{f_{prf}} \left[\begin{pmatrix} x_p^{accel} \\ y_p^{accel} \\ z_p^{accel} \end{pmatrix} - \begin{pmatrix} \bar{x}_{accel} \\ \bar{y}_{accel} \\ \bar{z}_{accel} \end{pmatrix} \right] \tag{5.22}$$

4. Calculation of the average velocity values ($\bar{x}_{vel}$, $\bar{y}_{vel}$, $\bar{z}_{vel}$) for the scene.

5. Subtraction of the average velocities and integration to find the x, y and z positional deviations. Once again, the integration constants are assumed zero.

$$\begin{pmatrix} x_p^{posn} \\ y_p^{posn} \\ z_p^{posn} \end{pmatrix} = \begin{pmatrix} x_{p-1}^{posn} \\ y_{p-1}^{posn} \\ z_{p-1}^{posn} \end{pmatrix} + \frac{1}{f_{prf}} \left[\begin{pmatrix} x_p^{vel} \\ y_p^{vel} \\ z_p^{vel} \end{pmatrix} - \begin{pmatrix} \bar{x}_{vel} \\ \bar{y}_{vel} \\ \bar{z}_{vel} \end{pmatrix} \right] \tag{5.23}$$

6. Calculation of the average positional deviation values ($\bar{x}_{posn}$, $\bar{y}_{posn}$, $\bar{z}_{posn}$) for the scene.

7. The position of the aircraft used for the calculation of the range deviation from the nominal focusing range is given by

$$\begin{pmatrix} x_p \\ y_p \\ z_p \end{pmatrix} = \begin{pmatrix} x_p^{posn} \\ y_p^{posn} \\ z_p^{posn} \end{pmatrix} - \begin{pmatrix} \bar{x}_{posn} \\ \bar{y}_{posn} \\ \bar{z}_{posn} \end{pmatrix} + \begin{pmatrix} 0 \\ 0 \\ \bar{h} \end{pmatrix} \tag{5.24}$$

   Note that the average height $\overline{h}$ above terrain is included in the z_p term as the coordinate system origin is at ground level.

8. The nominal ground range R_{grnd} to the focusing position in the swath (with slant range R_{foc}) is given by

$$R_{grnd} = \sqrt{(R_{foc})^2 - (\overline{h})^2} \tag{5.25}$$

9. The focusing position in the swath is taken to be constant for all PRIs since the nominal motion in the x direction is omitted as it cancels out of range correction calculations. The focusing position coordinates are therefore

$$\begin{pmatrix} x_{foc} \\ y_{foc} \\ z_{foc} \end{pmatrix} = \begin{pmatrix} 0 \\ R_{grnd} \\ 0 \end{pmatrix} \tag{5.26}$$

10. The actual range to the focusing position is given by

$$R_p^{actual} = \sqrt{(x_p - x_{foc})^2 + (y_p - y_{foc})^2 + (z_p - z_{foc})^2} \tag{5.27}$$

$$= \sqrt{(x_p)^2 + (y_p - R_{grnd})^2 + (z_p)^2} \tag{5.28}$$

11. Finally, the motion compensation range correction ΔR needed for PRI p (where a positive value of ΔR implies that the data should be shifted away) is

$$\Delta R = R_{foc} - R_p^{actual} \tag{5.29}$$

The corresponding phase correction required is given by Equation 5.2.

5.8.2 Motion Compensation Improvement in Imagery

In this section, the effects on an ESAR C-band image are shown for the high pass motion compensation technique, as described in Section 5.8.1. The imagery was processed by the candidate using the standard range-Doppler approach with motion compensation to a line and without range updates.

Figure 5.7 shows the improvement in a C-band image of the Lechveld area. For example, the road showing up as the dark vertical feature on the right of the image, almost disappears in the uncorrected image. For the motion compensated image both a phase shift and a range shift have been applied. Due to the high-pass filtering operations employed in the calculation of range corrections, the actual motion compensation range shifts for this image are small (typically less than 3 m) and as a result, the off-track range shifts are difficult to observe in the image. The phase correction is responsible for most of the improvement observed.

5.9 Summary

In this chapter, a number of issues relating to SAR motion compensation have been addressed. Two strategies for reconstruction of the flight path from inertial sensor data have been presented with the approach to be used dependent on the form of the available inertial data and the motion compensation requirements of the particular system under consideration. In addition to the more conventional stripmap motion compensation to a line, the "spotlike" approach developed by researchers at ERIM for dealing with angular motion compensation dependence for systems with wide processed azimuth beams has been discussed in the context of the SASAR VHF system.

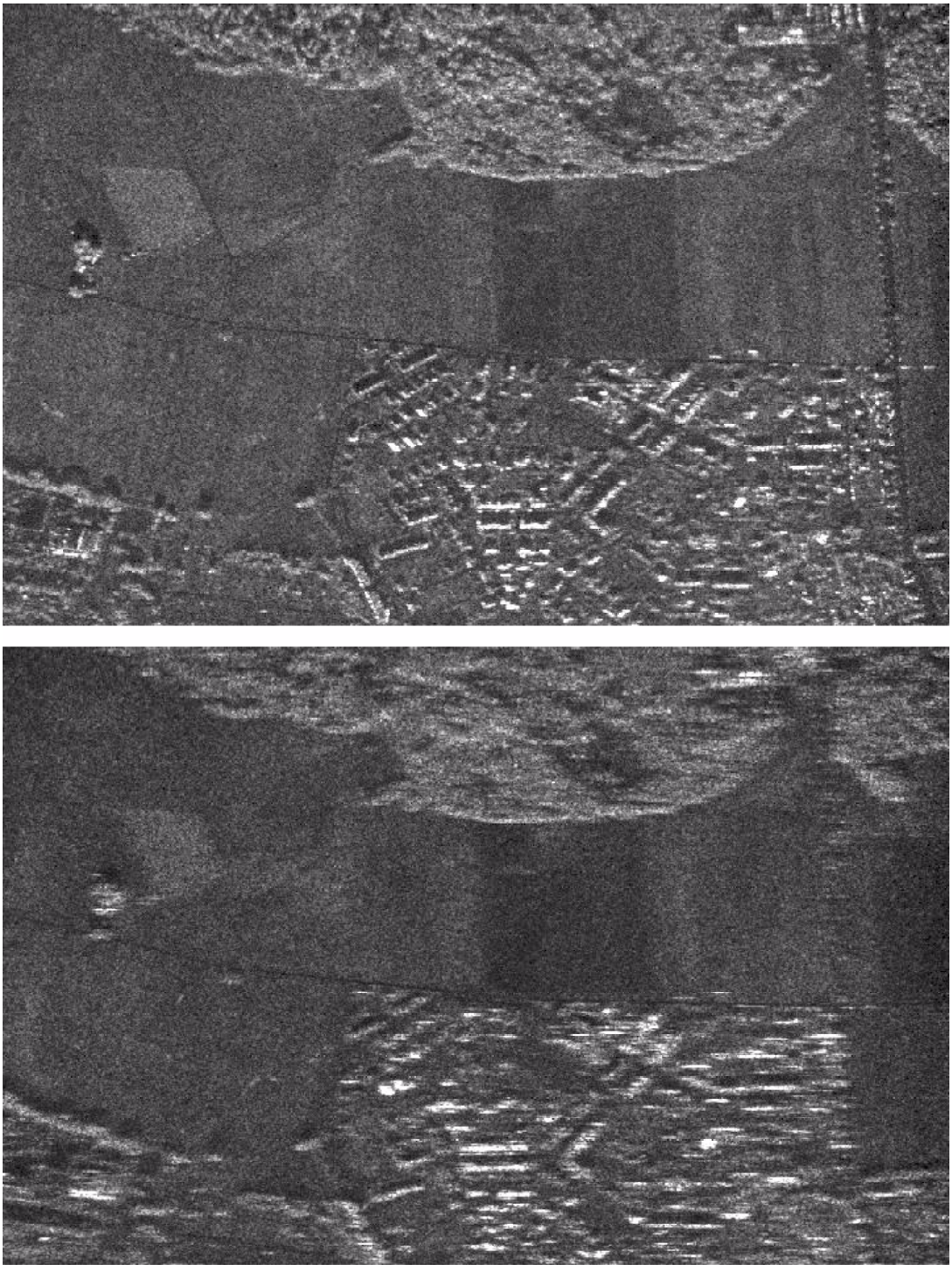

Figure 5.7: An ESAR multilook C-band image of the Lechfeld area with motion compensation (top) and without motion compensation (bottom). Flight direction from left to right with slant range increasing vertically. Processing parameters are the same for both images.

Chapter 6

SASAR VHF System

6.1 Introduction

The South African SAR System (SASAR) is the initiative of Prof. Mike Inggs of the University of Cape Town Radar Remote Sensing Group. The project has been funded since its inception by Armscor, the South African military procurement agency. The full system was envisaged to be fully polarimetric and operate in multiple frequency bands (VHF and L-band), but only the fully polarimetric VHF radar has been implemented to date. The VHF sensor was seen as an important research tool for ground penetration studies for geological and hydrological applications in dry regions of Southern Africa. In addition, the foliage penetration and sensitivity to man-made structures of the order of the wavelength was seen as being of clear interest for military surveillance. A recent overview of the project is given by Inggs [38].

The system started as an initiative (Inggs *et al.* [39]) to develop a low cost, digital recording system for the Russian 2.5 m SAR system (part of the iMARK system). This lesser known SAR was operated by the Moscow Scientific Research Institute of Instrument Engineering and the All-Union Scientific Research Institute of Kosmoaerological Methods. This sensor was flown on a Tupulev-134 aircraft and, in 1994, imagery was stored and processed optically.

The intention was to bring the Russian aircraft out to South Africa to demonstrate VHF SAR capabilities in local conditions to the mining industry. However, it transpired that the Russian aircraft required a major overhaul which far exceeded the South African budget for the project and the South African flights were cancelled.

During this period, the UCT RRSG designed and built a low cost, prototype digital

recording system which underwent an end-to-end test in the laboratory in 1993. As a result of this successful test, it was decided to construct the RF hardware required to complete a VHF SAR locally. At this point, the system integration and management of the project was given to the Aerotek division of the CSIR and the construction of the hardware was contracted out to industry. All signal processing for the system remained the responsibility of the UCT RRSG.

The platform to be used for the system was a South African Air Force (SAAF) Boeing 707 aircraft. This is a large, stable, high speed, pressurized platform. An antenna mounting structure in the form of a "cheek", fitted near the nose of the aircraft, was constructed, as the Boeing had already been modified to carry other instruments on such a cheek. The antenna elements for the Boeing aircraft were South African designed as an array of six (three by two), dual polarization inclined monopoles. Modelling of the Boeing antenna structure showed that the azimuth bandwidth was of the order of 45 degrees with a 60 degree elevation beamwidth.

However, the SAAF Boeing 707 aircraft to be used for the SAR became less and less available to due to increased use for diplomatic missions in this period. Thus, the decision was taken to move the system to an SAAF turboprop DC3 (Dakota) without ever flying the system on the Boeing 707. This was successfully completed in 1997. The DC3 is not as stable a platform as the Boeing, making the motion compensation more challenging. However, the slower DC3 does allow recording of the data at a lower rate, for a given azimuth beamwidth and transmitted frequency.

The low budget, low priority status of the project has resulted in the initial development period extending well beyond what was envisaged. However, the first radiating flights of the system occurred in January 1999. Results from these first flights are presented in the sections below.

The main objectives of this chapter are to present a short overview of the SASAR VHF project and to present some of the processing results and experience gained from the first radiating flights.

The candidate has been involved with the SASAR system from its inception with a major contribution to the top level system design issues particularly as relating to the SAR processing (including, for example, the choice of operating parameters). In addition, the candidate is responsible for all the SAR processing for the system. With the exception of the interference suppression routines which are the work of Richard

Lord of the UCT RRSG [42][43], the entire development, coding, implementation, and integration of the SAR processor (with motion compensation) is the candidate's own work (based on the standard range-Doppler algorithm).

6.2 System Parameters

The system has been designed with a modular, programmable approach. The number of data channels is variable (up to six currently) and each data channel is recorded on a removable IDE hard disk. All system timing is programmable in steps of 83.3 nanoseconds (including the pulse lengths, delay to start of sampling, etc.). Table 6.1 gives some of the main system parameters used for the first radiating flights of the SASAR VHF system on the DC3 aircraft.

6.2.1 Antenna

For the DC3, the inclined monopole antenna elements are mounted directly to the skin of the aircraft towards the tail and, due to space constraints, the antenna structure has been reduced to a two by two element array (from the three by two element array planned for the Boeing). The azimuth beamwidth of the antenna array on the DC3 has been modelled to be of the order of 60 degrees. The antenna structure, mounted on the DC3, is shown in Figure 6.1.

6.2.2 Doppler Bandwidth and Presumming

From Equation 2.12 of Chapter 2, for an azimuth beamwidth of 60 degrees with zero Doppler centroid and a ground speed of 90 m/s, the Doppler bandwidth is 84.5 Hz. The PRF used during the flights was 545 Hz with a presum of 4. Thus, the data were recorded at a rate of 136 Hz, well above the Doppler bandwidth and no azimuth ambiguity effects have been observed in the imagery. Note that, for the current SASAR recording system, a PRF of 136 Hz is close to the maximum sustainable recording rate.

Although not required for the current system, a study has been performed by Yann Tremeac of the UCT RRSG [63] on the reduction of the data rate for the VHF Boeing system through the two-stage implementation of a presum operation by 3, followed by a low pass FIR filter operation with 31 taps. After the prefilter, the data are subsampled in azimuth by 4 for a total data rate reduction factor of 12. Analysis of a simulated VHF wide beam signal (13 metres range resolution, 45 degree azimuth

Parameter	**Value**
Centre frequency	141 MHz
Polarization	HH, VV
Max system bandwidth	12 MHz (originally 6 MHz)
Best slant range resolution	12 m
Pulse modulation	monochromatic
Pulse length	increments of 83.3 nsec
PRF	programmable (545 Hz used in first flights)
Ground speed	90 m/s
Max height above sea level	4000 m
Transmit peak power	1 kW
Gain control	manual
STC	switchable (not applied for these flights)
Delay to start of sampling	20 usec
Receiver noise factor	8 dB
Presum Ratio	4
A/D frequency	up to 24 MHz
Range samples	2048 / 4096
Data format	8-bit unsigned char I and Q
Azimuth beamwidth	60 degrees
Elevation beamwidth	60 degrees

Table 6.1: SASAR VHF parameters for the first radiating flights.

Figure 6.1: The SASAR VHF antenna array structure as mounted on the DC3 aircraft.

beamwidth, target at 14 km closest approach, PRF 625 Hz, signal Doppler bandwidth 177 Hz) has shown that the peak azimuth signal ambiguity levels in the azimuth focused image (with 52 Hz azimuth sampling) are below −60 dB. This indicates that a two-dimensional prefilter would not have been required for the Boeing system despite the severe range curvature.

If a prefilter is applied to SASAR without first applying motion compensation, some consideration should be given to the along track coherence requirements. The tenth of a wavelength motion compensation positional accuracy requirement translates into requiring that the aircraft not deviate from the nominal track by more than 21 cm over a period of approximately 150 msec (the time extent spanned by the prefilter). This is easily achievable.

6.2.3 Gain Settings

For the flight tests, the gain settings were set such that the noise was sampled by a few levels of the 8-bit A/D range. The backscattered signal was, in general, below the noise level before SAR processing. It was found that, given these gain settings,

even the largest signals received (from the interference) did not saturate. This allowed for more accurate interference suppression since clipped interference would introduce higher harmonics.

6.2.4 Processor Choice

The maximum target slant range used for the test flights was 27 km. From the analysis of Chapter 3 (Figure 3.19), for a perfectly motion compensated point target at 30 km closest approach range to suffer from less than 10 percent range broadening where the slant range resolution is 12 metres, the target may be processed to about 4 metre resolution in azimuth with the standard range-Doppler processor. Thus, using the ten percent broadening criterion, the use of the standard range-Doppler processor allows processing to an azimuth resolution of about 12 metres (to match the range resolution) with three independent looks. This was deemed sufficient for the initial system evaluation purposes, especially given the many other system unknowns such as the motion compensation accuracy.

For more stringent processing requirements, an alternate processing algorithm such as the extended range-Doppler processor of Chapter 4, or the range migration approach of Cafforio *et al.* [16], should be used.

6.3 Results of First Flights

6.3.1 Interference Suppression

It became clear from the first system ground tests that interference in the frequency band of the VHF radar would require suppression to avoid serious contamination in the focused images. This has indeed been the case for the first radiating flights with the interference showing up as bright vertical lines in the focused images.

Two interference suppression techniques have been developed for the radar by Richard Lord of the UCT RRSG. Details of these may be found in [42] and [43]. One technique applies a least mean square adaptive filter and the other a simple notch filtering in the range frequency domain. The use of either technique results in a large visual improvement in the processed VHF images. The success of the interference suppression is attributed to the narrow band nature of the interfering signals encountered at these frequencies during these flights.

An efficient method of implementing the interference suppression routines has been found by incorporating the interference suppression with the range compression stage of the range-Doppler processor (as shown in Figure 2.7 in Chapter 2).

An improvement in the image contrast was obtained by sampling the data at a high rate (24 MHz was used for some of the data takes) and then restricting the bandwidth to the bandwidth of the transmitted signal. In practice, this was achieved by applying range compression (with a zero phase range reference function) to the data. The system as currently implemented does not use a receive filter matched to the transmitted pulse bandwidth. Thus, for the longer pulses used to date, the range compression step results in significant improvements in the images as the range compression stage acts as the filter matched to the transmitted signal bandwidth, resulting in better interference and noise suppression.

6.3.2 Image Signal to Noise Ratio

It is clear from the imagery processed thus far that the SASAR VHF images are suffering from a low signal to noise ratio, particularly at far range. The images showing more far range structure are those where longer pulses have been used. There are a number of reasons for the poor image SNR:

- The beam former, shown in Figure 6.2, was designed for the 6-element array on the Boeing. Thus, it was necessary to make use of dummy loads on two of the unused ports. The result of this is that only two thirds of the available power is actually transferred to the antenna. Thus the 1 kW figure in Table 6.1 is larger than is actually the case.

- The wider beam of the two by two array reduces the antenna gain and hence the SNR in the processed images.

- More work is required to improve the motion compensation which will increase the SAR processing gain.

The image SNR should be greatly improved by the incorporation of a pulse expander for the next flights (scheduled for 1999) where pulses of the order of 15 microseconds will be used (Section 6.4).

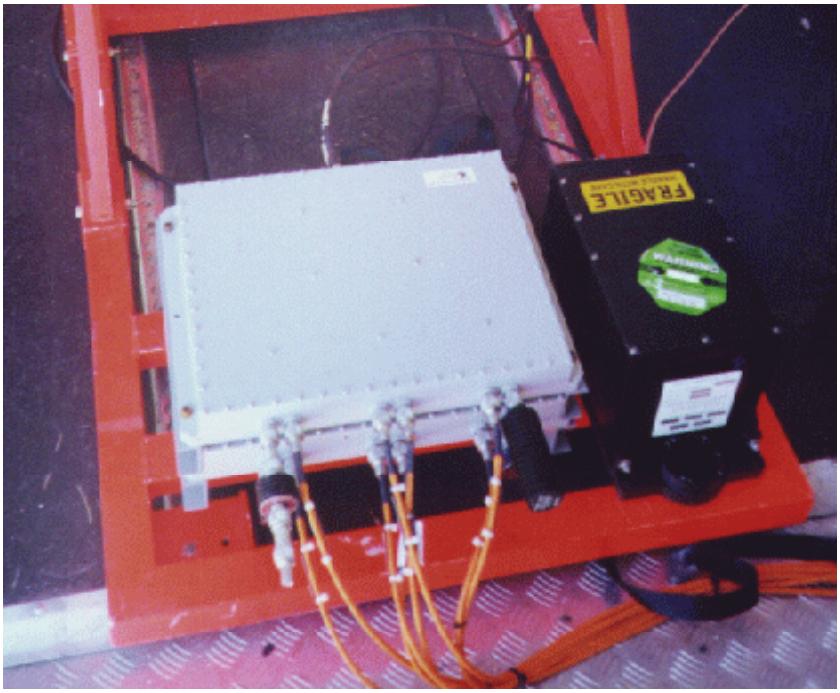

Figure 6.2: The SASAR VHF beamformer on left (note the two dummy loads) and inertial unit (on right).

6.3.3 Drifts in A/D Converters

After the A/D conversion, the data for the I and Q channels are stored as 8-bit unsigned characters. An effect which requires correction for SASAR is that the DC offsets for the I and Q channels tend to drift by a few levels over the period of a few minutes. Compounded with the already low signal level for these first tests, the uncorrected drift can in some cases result in all ground features disappearing from the focused image. To compensate for this, the average value of each channel was calculated for the block of data to be processed. The average value is used as the DC offset for the processing.

6.3.4 Motion Compensation

The motion compensation implementation for the first flight tests has been discussed in Chapter 5. The motion compensation applied to the VHF data has yielded a small visual improvement thus far, but more work is needed in this area to correct for the drifts of the inertial data over the synthetic aperture lengths. Work is proceeding in this area (Section 6.4).

Note that, to date, the "spotlike" motion compensation approach has not been

attempted and the motion compensation has not been updated with range. The more serious drift effects are being addressed as the first priority.

6.3.5 Detection of Man-made Structures

One of the notable features of the processed imagery from the first flights has been that man-made structures of the order of the wavelength (such as dwellings) show up very brightly. In addition, there are a number of cases of bright linear structures oriented parallel to the flight path which show up very brightly. Investigation has shown that these linear features are not the azimuth sidelobe structure of very bright targets. The linear features are thought to be man-made linear structures such as fences (or wires) whose orientation is such that it happens to lie parallel to the flight track, yielding a large, extended backscattered return. Interestingly, these features show up in both the HH and VV images (possibly indicating coupling between polarization channels). Recent discussions with members of the Swedish CARABAS group have indicated that similar features are visible in the CARABAS imagery and do correspond to fences. Further system characterization and ground truth work will be performed here.

6.3.6 SASAR VHF Imagery

Despite the low SNR, encouraging results were obtained from the first radiating flights of the SASAR VHF sensor in January 1999, particularly for the detection of man-made objects of the scale of the wavelength. Note that, for these flights, only one pass was made of each scene and both HH and VV polarizations were recorded.

Figure 6.3 shows an HH polarization VHF image of the Gansbaai area near Cape Town, South Africa. The long transmitted pulse used for this data set (75 m range resolution) resulted in features visible across the whole 24 km range swath (only 12 km shown). There are a number of features of interest in this image. The nadir return is the bright horizontal line towards the bottom. Some residual interference (vertical lines) is visible in the dark region at the very bottom before any backscattered signal was received. The horizontal scalloping effect above the nadir return is an artifact of the LMS interference filter when processing the bright nadir return. The bright regions towards the lower left are buildings and the coastline is visible. The flight for this data take was largely over the ocean with a small part over the land, as witnessed by the small deviation in the start of the nadir return towards the left of the image.

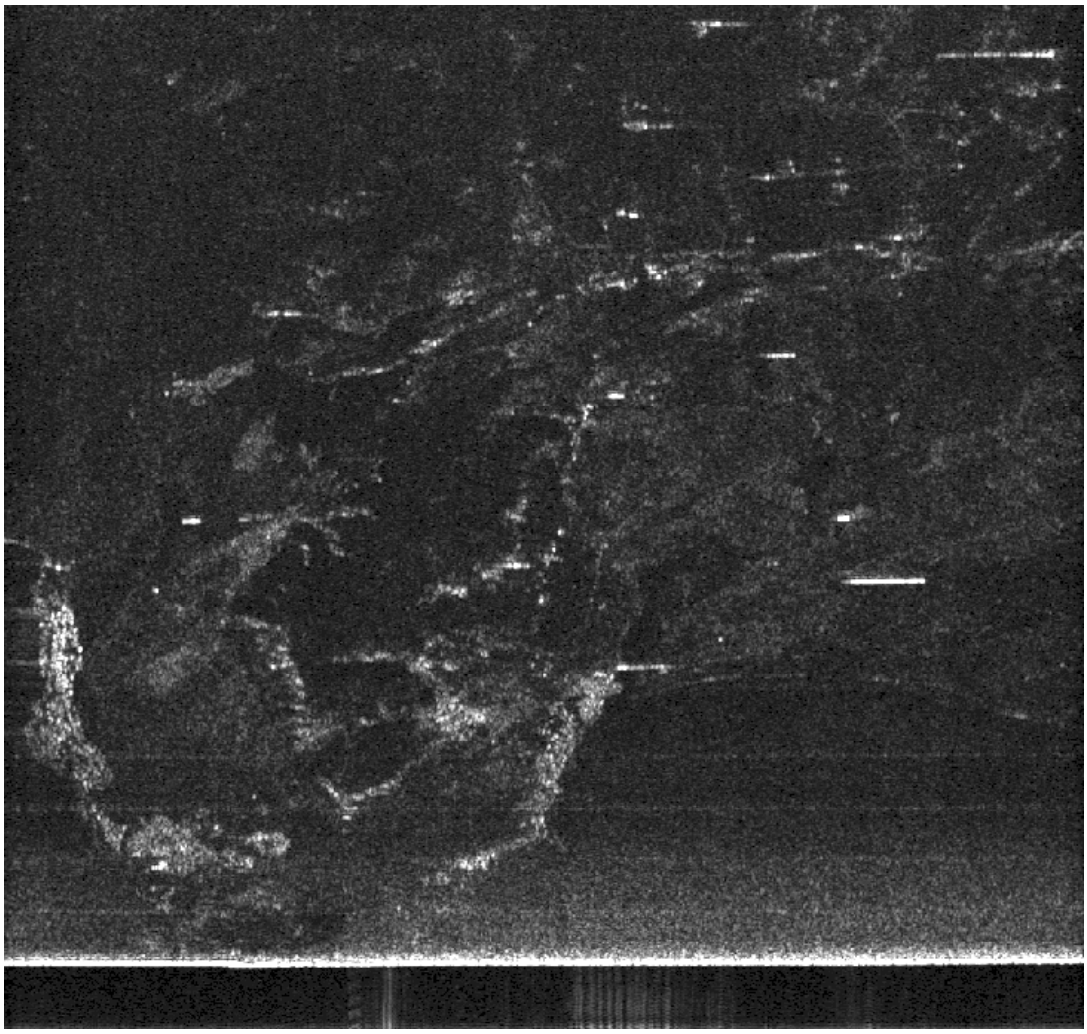

Figure 6.3: The Gansbaai area near Cape Town. The image extent is 13 km in azimuth (horizontal) by 12 km in slant range (increasing vertical). HH polarization, 22 m nominal azimuth resolution, 4 looks (2.5 independent), 75 m range resolution, LMS adaptive interference filter, first order motion compensation, range compression.

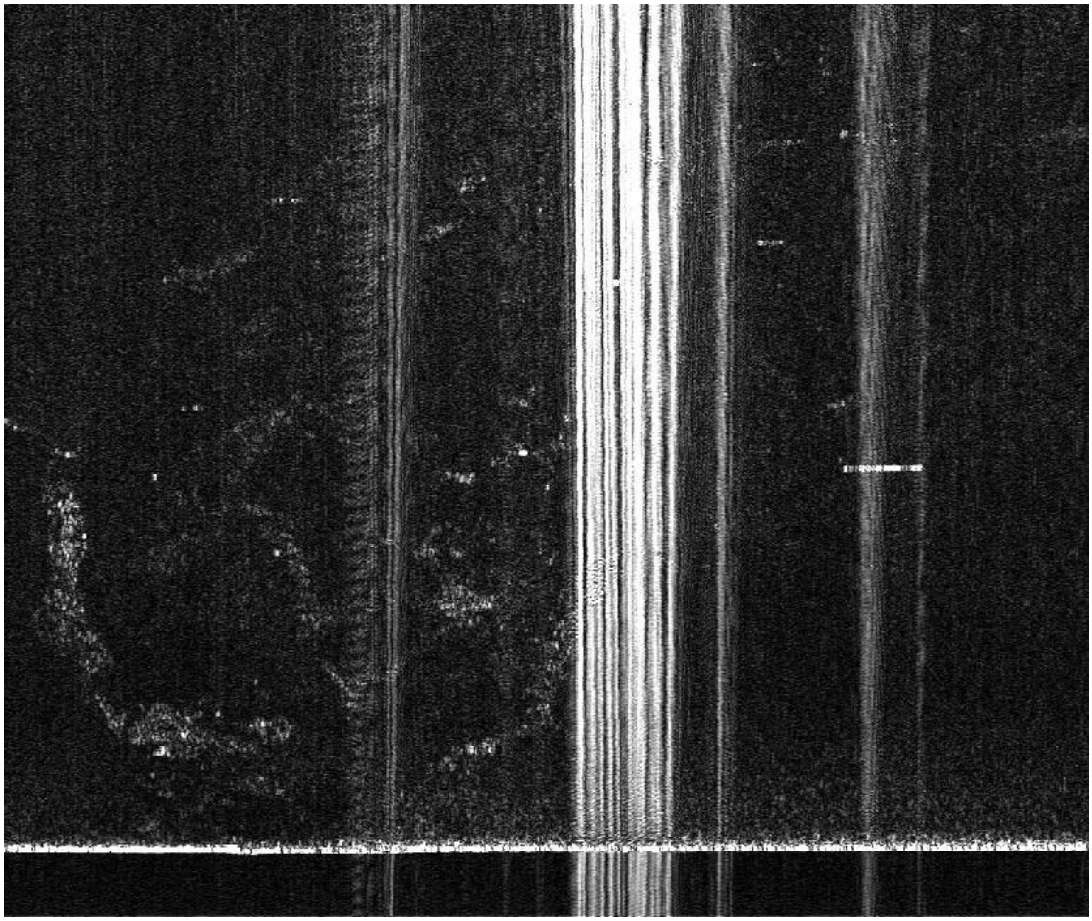

Figure 6.4: SASAR VHF HH image of the Gansbaai area. The image extent is 13 km in azimuth (horizontal) by about 12 km in slant range (increasing vertical). 22 m nominal azimuth resolution, 4 looks (2.5 independent), 75 m range resolution, no interference suppression, no range compression.

Figure 6.4 shows the same area as Figure 6.3, but the image is single look, without range compression, interference suppression and motion compensation. The severe degrading effect of the interference is clearly visible as the bright vertical lines. The bright linear features parallel to the flight track are discussed in Section 6.3.5.

Figure 6.5 shows the most southern part of Africa, Cape Agulhas. The dark region at the bottom is ocean. The bright regions are the town areas with an interference suppression filter artifact visible as the smearing above the very bright feature at mid right.

As a comparison between the VV and HH channels, Figures 6.6 and 6.7 are single look VV and HH images, respectively, without motion compensation of the Cape

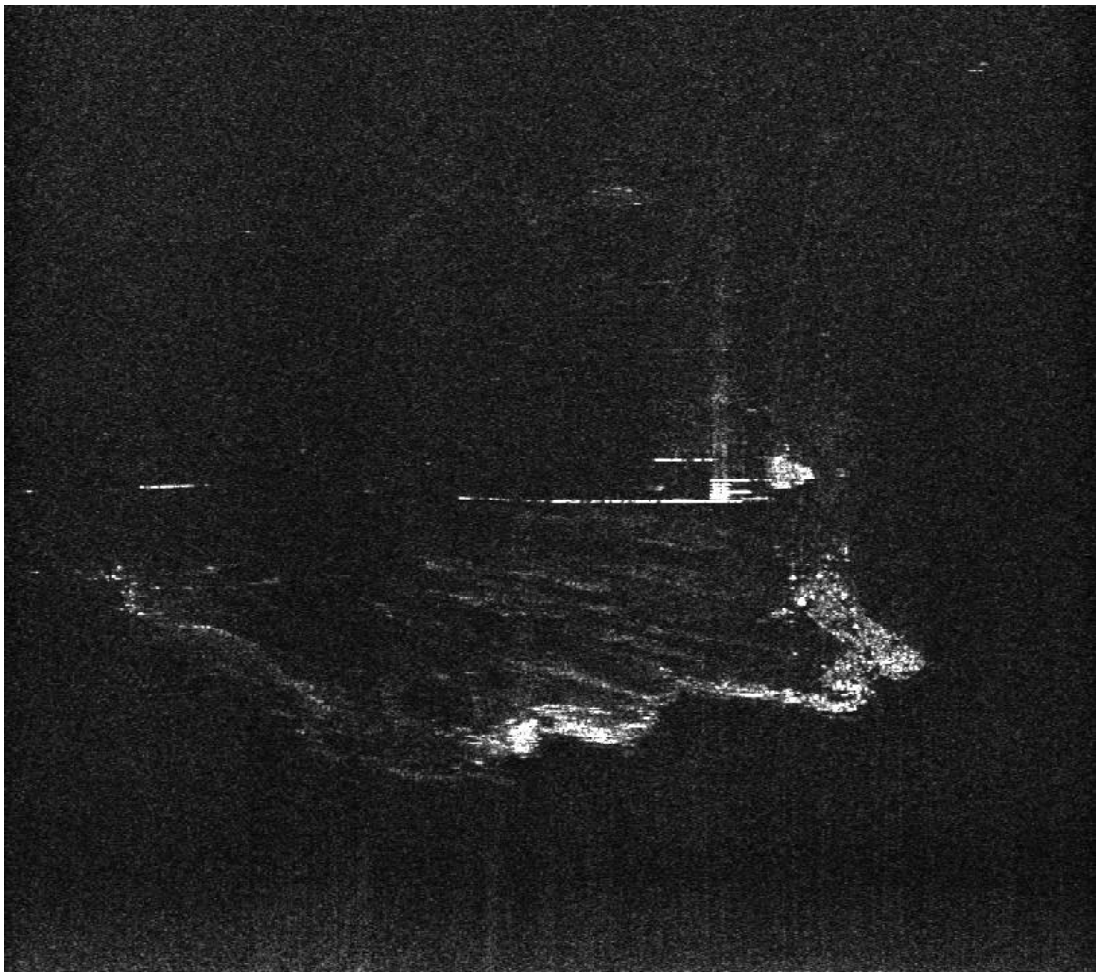

Figure 6.5: SASAR VHF HH image of the Cape Agulhas area. The image extent is 13 km on a side with slant range increasing vertically. 25 m range resolution, LMS adaptive intereference suppression, range compression, 22 m nominal azimuth resolution, 4 looks (2.5 independent), range compression.

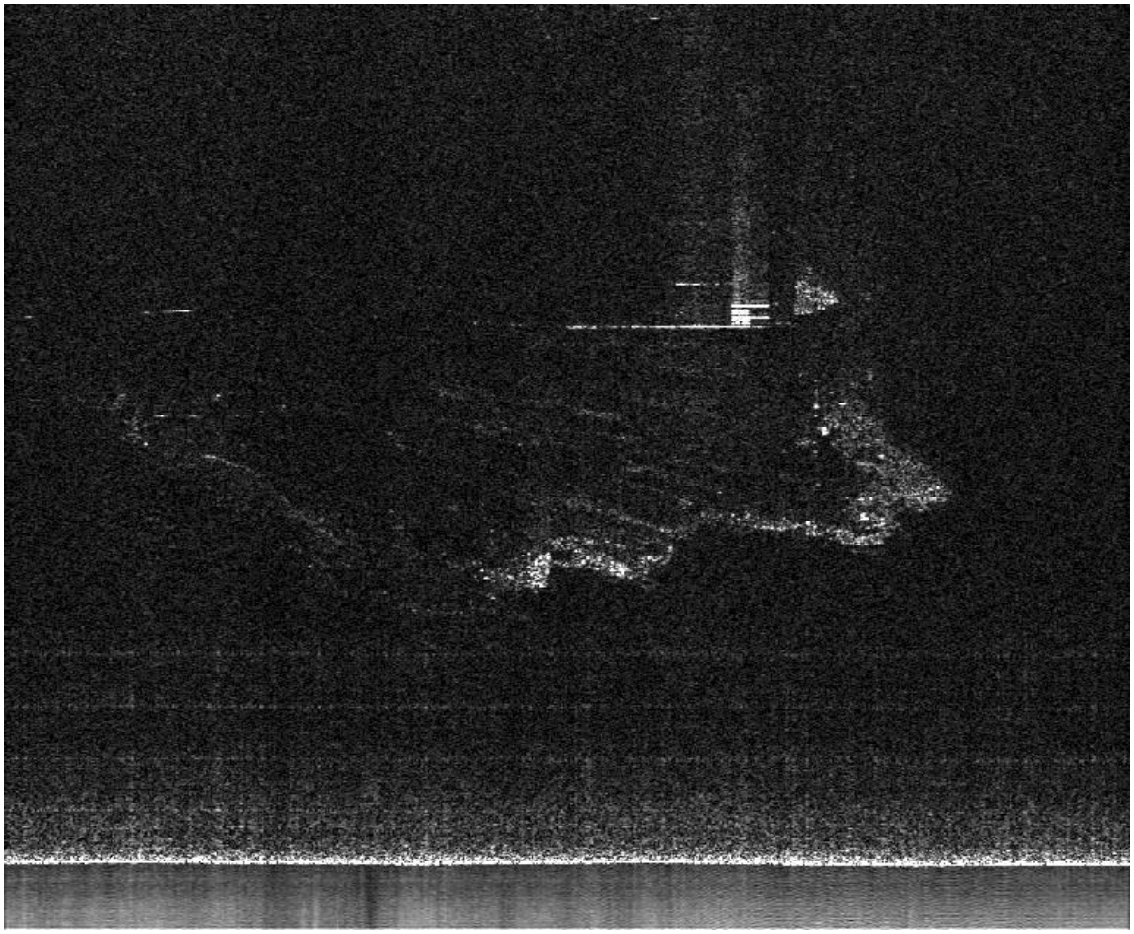

Figure 6.6: SASAR VHF VV single look image of the Cape Agulhas area. Azimuth and range extent is 13 km with slant range increasing vertically. Nominal azimuth resolution 22 m, 25 m range resolution, range compression, LMS adaptive interference suppression, no motion compensation.

Agulhas area. Aside from the IQ channel DC offsets, the same processing parameters have been used for these two images. In general, more interference was observed in the VV images than the HH images processed. Scalloping due to the LMS intereference filter processing of the bright nadir return is visible.

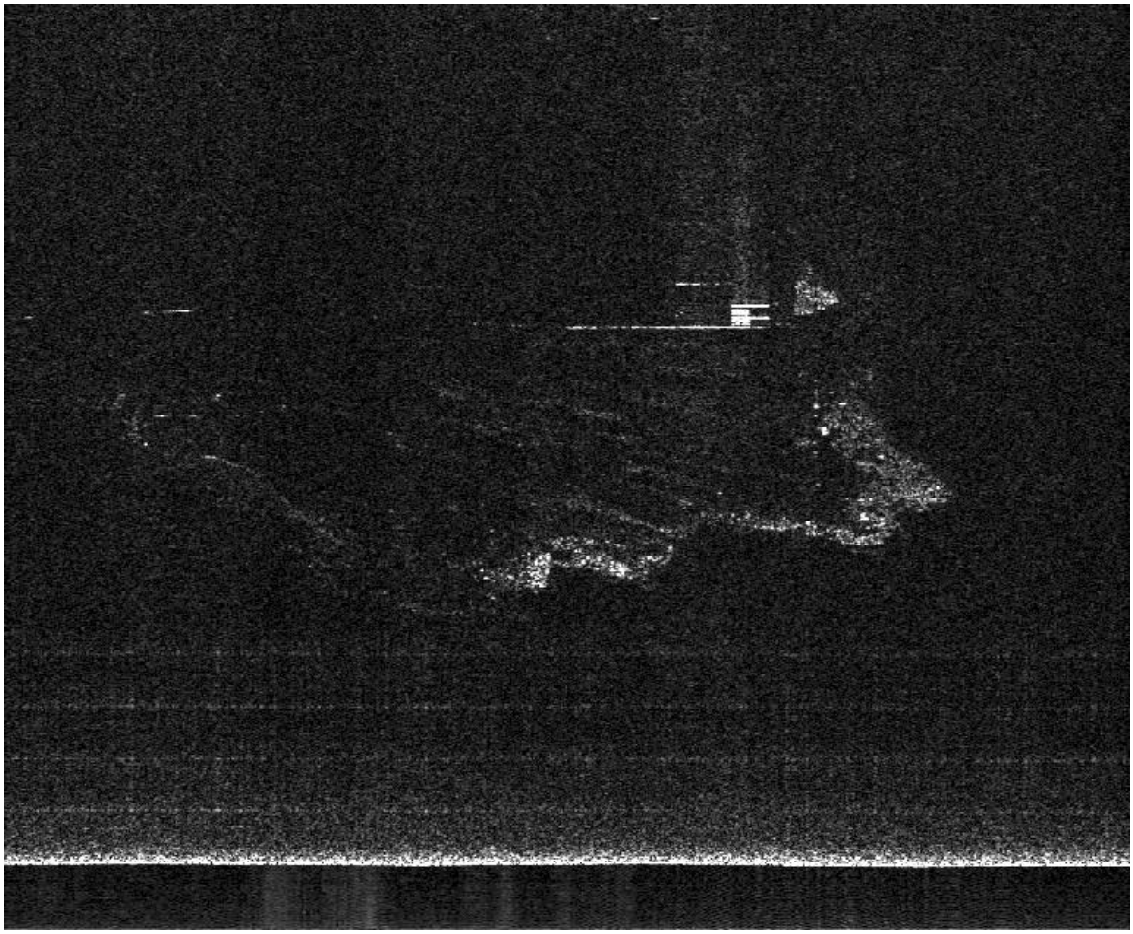

Figure 6.7: SASAR VHF HH single look image of the Cape Agulhas area. Azimuth and range extent is 13 km with slant range increasing vertically. Nominal azimuth resolution 22 m, 25 m range resolution, range compression, LMS adaptive interference suppression, no motion compensation.

Figure 6.8: A mosiac of video frames of the Cape Agulhas area recorded at the same time as the radar data.

During the SASAR flights, a corresponding video image was obtained through a window of the aircraft. For reference, a video mosaic of the Cape Agulhas area is shown in Figure 6.8.

6.4 Future Activities

The first radiating flights have yielded encouraging results, but there is much work to be done to improve the system. The following are seen as being of high priority:

- Incorporation of the pulse expander. This should be complete by June 1999. A linear FM pulse modulation will be used with a bandwidth of 12 MHz and a pulse length of the order of 15 microseconds. This pulse length is a factor of 180 longer than the shortest pulse currently used of 83.3 nanoseconds (yielding 12 m resolution). The use of the pulse expander will require that the range compression is performed in software. However, this will not affect the processing time significantly as the interference suppression already makes use of the range compression routine.

- Work to improve the motion compensation by removing long term drift effects. Use is planned of differential GPS for the next flights to assist in this regard. In addition, the timing latencies in the motion compensation data have yet to be determined.

- More work on characterizing all aspects of system performance and system calibration. This would include flights over a well known site equipped with calibration reflectors (or transponders).
- Work on establishing ground truth for the scenes imaged and VHF image interpretation.

Chapter 7

Conclusions and Scope for Future Research

7.1 Conclusions

This thesis has focused on the application of range-Doppler processing at VHF frequencies for wide beam, airborne, stripmap SAR systems with zero Doppler centroid and modest relative pulse bandwidths. The theory of such SAR operation has been addressed, particularly as pertaining to range-Doppler processing.

The regions of applicability of standard range-Doppler processing, when applied without Doppler frequency dependent SRC, have been investigated for a range of processing parameters in the frequency range of 100 MHz to 200 MHz, but with emphasis on the SASAR VHF frequency of 141 MHz. Using simulated SAR signals, the effects of centre frequency, target closest approach range and nominal range resolution have been investigated, each for a range of processed azimuth resolutions. Plots have been produced showing these dependencies, with the intention that these may serve as useful references as to the limits of standard range-Doppler processors at these frequencies. The analysis of processor performance includes the azimuth resolution, but has focused on the degradation of the range impulse response and quantified in terms of resolution measurements, the peak- and integrated sidelobe levels, and the non-linear phase error in the Fourier domain.

A extension to range-Doppler processing, with basic idea first published by Raney and Vachon, has been demonstrated to cater for the severe range curvature case. The extended processor, suggested in this context by Jin, makes use of an initial correction

to a reference range through a multiplication with a reference function in the 2-D frequency domain. This is followed by a residual range curvature and azimuth focusing operation in the range-Doppler domain. Through processing of range compressed simulated SAR signals with severe range curvature, the extended processor has been shown to provide significantly improved performance over the standard range-Doppler processor. The extended processor has been demonstrated for two reference ranges: one matched to one of the simulated targets and the other to a range outside of the range of the simulated data set. As would be expected, the processing performance degrades with mismatch between target range and reference range, but the results are still vastly better than for the standard range-Doppler processor. Once again, the analysis has focused on the range impulse response and quantified in terms of resolution, peak- and integrated sidelobe levels, and non-linear Fourier phase.

Airborne motion compensation strategies as currently implemented for the SASAR VHF sensor and the ESAR system have been discussed. A technique for calculation of the flight path in Cartesian coordinates given latitude, longitude and ellipsoidal height measurements, has been presented. In addition, an ERIM-developed approach for including an azimuth dependence for wide beam motion compensation has been discussed in the context of the SASAR system.

A brief overview of the SASAR VHF project, as well as results and experience gained from the signal processing of the data from the first radiating flights, has been presented. The results from the first flights are encouraging, with man-made objects of the scale of the wavelength showing up very brightly in the imagery. The further development and testing of this sensor for a range of applications should help fill a significant gap in the general SAR knowledge about what useful information can be obtained from an airborne system at these frequencies.

7.2 Future Work

Scope for future work includes:

- An expansion of the work of the investigation into the processing performance of the standard range-Doppler algorithm when applied to signals with severe range curvature. While much effort was expended in obtaining the results of Chapter 3, the VHF simulation parameters used only span a small subset of possible regions of interest (higher frequencies with finer range resolutions are an example). Such

an investigation would be aided by a thorough mathematical analysis, if this proves tractable.

- A processor performance comparison between the extended range-Doppler processor and other approaches such as chirp scaling and the range migration algorithms.

- An investigation into the application and performance benefits of using multiple 2-D reference functions with the extended algorithm.

- The application of the extended algorithm to real data sets with severe range curvature. For example, application to the P3 SAR data would allow for a comparison, both in efficiency and performance with the range migration approach currently in use.

- Work on improving the motion compensation for the SASAR VHF sensor, given the inaccuracies of the inertial measurements. The use of differential GPS is under consideration to assist in this regard for the next flights. In addition, given the bright nature of certain scatterers relative to the background, it may well be possible to make use of autofocus techniques with the SASAR VHF imagery. The application of such techniques as prominent point processing (Carrara *et al.* [17] pg. 326) requires investigation for SASAR.

- Much work is required on characterization of the performance of the elements making up the SASAR VHF sensor. This includes investigation into phase errors, channel imbalances, and all aspects of system calibration. In addition, the on-board quicklook processor requires an upgrade if it is to be useful for the VHF sensor. An activity is planned at the UCT RRSG to create a parallel version of the current range-Doppler SAR processor which will run on a cluster of PCs. Once operational, this will allow for a very high speed, but low cost ground processor. In addition, the same code may be run (with less demanding parameters) on board the aircraft as the quicklook processor.

- With the first images from the SASAR VHF sensor comes the task of image interpretation and extraction of features of interest. This task has only just begun.

Bibliography

[1] Private discussion with Michael Jin at JPL, Pasadena, California. April 1998.

[2] Private e-mail correspondance with Richard Bamler of DLR/DFD, Germany. April 1999.

[3] Private discussion with Richard Bamler at DLR/DFD, Germany. August 1997.

[4] Private e-mail correspondance with Ron Goodman of ERIM, USA. March 1997.

[5] Dale A. Ausherman, Adam Kozma, Jack L. Walker, Harrison M. Jones, and Enrico C. Poggio. Developments in Radar Imaging. *IEEE Transactions on Aerospace and Electronic Systems*, AES-20(4):363–400, July 1984.

[6] Sune R.J. Axelsson. Frequency and Azimuthal Variations of Radar Cross Section and Their Influence Upon Low-Frequency SAR Imaging. *IEEE Transactions on Geoscience and Remote Sensing*, 33(5):1258–1265, September 1995.

[7] Richard Bamler. A Comparison of Range-Doppler and Wavenumber Domain SAR Focussing Algorithms. *IEEE Transactions on Geoscience and Remote Sensing*, 30(4):706–713, July 1992.

[8] Richard Bamler. SAR Processing Theory - Lecture Notes. Deutche Forschungsanstalt fur Luft- un Raumfahrt (DLR), 1996.

[9] B.C. Barber. Theory of Digital Imaging from Orbital Synthetic-Aperture Radar. *International Journal of Remote Sensing*, 6(7):1009–1057, 1985.

[10] Graydon L. Berlin, Mohammed A. Tarabzouni, Abdullah H. Al-Naser, Kamel M. Sheikho, and Richard W. Larson. SIR-B Subsurface Imaging of a Sand-Buried Landscape: Al Labbah Plateau, Saudi Arabia. *IEEE Transactions on Geoscience and Remote Sensing*, GE-24(4):595–602, July 1986.

[11] Björn Larsson, Per-Olov Frölind, Anders Gustavsson, Hans Hellsten, Tommy Jonsson, Gunnar Stenström, and Lars Ulander. Some Results from the New CARABAS II SAR System. In *Proceedings of Third International Airborne Remote Sensing Conference and Exhibition*, Copenhagen, Denmark, 1997.

[12] Ron Bracewell. *The Fourier Transform and Its Applications*. McGraw-Hill, New York, 1965.

[13] William M. Brown. Synthetic Aperture Radar. *IEEE Transactions on Aerospace and Electronic Systems*, AES-3(2):217–229, March 1967.

[14] Stefan Buckreuss. Motion Errors in an Airborne Synthetic Aperture Radar System. *ETT Journal*, 2(6):655–664, November 1991.

[15] Stefan Buckreuss. Motion Compensation for Airborne SAR Based on Inertial Data, RDM and GPS. In *Proceedings of the 1994 International Geoscience and Remote Sensing Symposium (IGARSS '94)*, volume 4, pages 1971 – 1973, Pasadena, USA, August 94.

[16] C. Cafforio, C. Prati, and E. Rocca. SAR Data Focusing Using Seismic Migration Techniques. *IEEE Transactions on Aerospace and Electronic Systems*, 27(2):194–207, March 1991.

[17] Walt G. Carrara, Ron S. Goodman, and Ronald M. Majewski. *Spotlight Synthetic Aperture Radar - Signal Processing Algorithms*. Artech House, Boston, 1995.

[18] Walter Carrara, Sreenidhi Tummala, and Ron Goodman. Motion Compensation Algorithm for Widebeam Stripmap SAR. *Proceedings of the SPIE*, 2487:13–23, 1995.

[19] Charles E. Cook and Marvin Bernfeld. *Radar Signals - An Introduction to Theory and Application*. Artech House, MA, 1993.

[20] John C. Curlander and Robert N. McDonough. *Synthetic Aperture Radar*. Wiley, Canada, 1991.

[21] Mark R. Drinkwater, Ronald Kwok, and Eric Rignot. Synthetic Aperture Radar Polarimetry of Sea Ice. In *Proceedings of the 1990 International Geoscience and Remote Sensing Symposium (IGARSS '90)*, volume 2, pages 1525 – 1528, Washinton D.C., USA, May 1990.

[22] Charles Elachi. *Introduction to the Physics and Techniques of Remote Sensing*. John Wiley and Sons, New York, 1987.

[23] Charles Elachi. *Spaceborne Radar: Remote Sensing Applications and Techniques*. IEEE Press, 345 East 47th Street, New York, 1988.

[24] Charles Elachi, Ladislav E. Roth, and Gerald G. Schaber. Spaceborne Radar Subsurface Imaging in Hyperarid Regions. *IEEE Transactions on Geoscience and Remote Sensing*, GE-22(4):383–387, July 1984.

[25] Diane Evans. Multisensor Classification of Sedimentary Rocks. *Remote Sensing of Environment*, 25:129–144, 1988.

[26] Diane L. Evans, Tom G. Farr, Jakob J. van Zyl, and Howard A. Zebker. Radar Polarimetry: Analysis Tools and Applications . *IEEE Transactions on Geoscience and Remote Sensing*, 26(6):774–789, November 1988.

[27] Ron Goodman, Sreenidhi Tummala, and Walter Carrara. Issues in Ultra-Wideband, Widebeam SAR Image Formation. In *Proceedings of the 1995 IEEE International Radar Conference*, pages 479–485, Alexandria, VA, USA, May 1995.

[28] Anders Gustavsson, Hans Hellsten, and Björn Larsson. Realization of an Airborne Low Frequency SAR. In *Proceedings of the Microwave Signature 92 conference*, pages 1C23 – 1C27, 1992.

[29] Anders Gustavsson, P.O. Frölind, Hans Hellsten, T. Jönsson, Björn Larsson, and G. Stenström. The Airborne VHF SAR System CARABAS. In *Proceedings of the 1993 International Geoscience and Remote Sensing Symposium (IGARSS '93)*, volume 2, pages 558–562, Tokyo, Japan, August 1993.

[30] Frederic J. Harris. On the Use of Windows for Harmonic Analysis with the Discrete Fourier Transform. *Proceedings of the IEEE*, 66(1):51–83, January 1978.

[31] Hans Hellsten and Lars Erik Andersson. An Inverse Method for the Processing of Synthetic Aperture Radar Data. *Inverse Problems*, 3:111–124, 1987.

[32] Floyd M. Henderson and Anthony J. Lewis (editors). *Principles and Applications of Imaging Radar - Manual of Remote Sensing - Third Edition*, volume 2. John Wiley and Sons, New York, 1998.

[33] Ralf Horn. DLR Airborne SAR Project, Objectives and Status. In *Proceedings of 1st Airborne Remote Sensing Conference and Exhibition*, Strasbourg, France, 1994.

[34] Jasper Horrell and Mike Inggs. Range Curvature Limitation of the Range-Doppler Algorithm Stripmap SAR Processing. In *Proceedings of 1998 European Conference on Synthetic Aperture Radar (EUSAR '98)*, pages 99–102, Friedrichshafen, Germany, 25-27 May 1998.

[35] Jasper M. Horrell. An Extension to Range-Doppler SAR Processing to Accommodate Severe Range Curvature. In *Proceedings of 1999 International Geoscience and Remote Sensing Symposium (IGARSS '99) - to be published*, Hamburg, Germany, June 1999.

[36] J.M. Horrell and M. R. Inggs. Low Frequency Range-Doppler SAR Processing without Secondary Range Compression. In *Proceedings of 1998 IEEE South African Symposium on Communications and Signal Processing (COMSIG '98)*, pages 109–114, University of Cape Town, South Africa, September 1998.

[37] Heidi A. Hovland, Johnny A. Johannessen, and Gunnar Digranes. Slick Detection in SAR Images. In *Proceedings of the 1994 International Geoscience and Remote Sensing Symposium (IGARSS '94)*, pages 2038–2040, Pasadena, USA, 1994.

[38] M.R. Inggs. First Results from the South African VHF Imaging Radar. In *Proceedings of 3rd IMACS / IEEE International Multiconference on Circuits, Systems, Communications and Computers (CSCC '99) - to be published*, Athens, Greece, July 1999.

[39] M.R. Inggs, J.M. Horrell, A. Knight, and P.G. Koeppen. iSAR: A Multispectral, Polarimetric Airborne SAR System . In *Proceedings of the 1994 International Geoscience and Remote Sensing Symposium*, volume 4, pages 2237–2239, Pasadena, USA, August 1994. IGARSS '94.

[40] John C. Kirk. A Discussion of Digital Processing in Synthetic Aperture Radar. *IEEE Transactions on Aerospace and Electronic Systems*, AES-11(3):326–337, May 1975.

[41] R Lengenfelder. The Design and Implementation of a Radar Simulator. Master's thesis, Dept. Electrical Engineering, University of Cape Town, South Africa, September 1998.

[42] R.T. Lord and M.R. Inggs. Approaches to RF Interference Suppression for VHF/UHF Synthetic Aperture Radar. In *Proceedings of 1998 South African Symposium on Communications and Signal Processing (COMSIG '98)*, pages 95–100, University of Cape Town, South Africa, September 1998. IEEE.

[43] R.T. Lord and M.R. Inggs. Efficient RFI Suppression in SAR Using a LMS Adaptive Filter with Sidelobe Suppression Integrated with the Range/Doppler Algorithm. In *Proceedings of the 1999 International Geoscience and Remote Sensing Symposium (IGARSS '99) - to be published*, Hamburg, Germany, June 1999.

[44] Geoffrey J. Lynne and Geoffrey R. Taylor. Geological Assessment of SIR-B Imagery of the Amadeus Basin, N.T., Australia. *IEEE Trans on Geosc. and Remote Sensing*, GE-24(4):575–581, July 1986.

[45] Soren N. Madsen, Howard A. Zebker, and Jan Martin. Topographic Mapping Using Radar Interferometry: Processing Techniques. *IEEE Transactions on Geoscience and Remote Sensing*, 31(1):246–256, January 1993.

[46] John F. McCauley, Carol S. Breed, Gerald G. Schaber, William P. McHugh, Bahay Issawi, C. Vance Haynes, Maurice J. Grolier, and Ali El Kilani. Paleodrainages of the Eastern Sahara - The Radar Rivers Revisited. *IEEE Transactions on Geoscience and Remote Sensing*, GE-24(4):624–648, July 1986.

[47] Charles Merry. Lecture Notes on Coordinate Systems. University of Cape Town, 1998.

[48] Michael Y. Jin and Chialin Wu. A SAR Correlation Algorithm which Accommodates Large Range Migration. *IEEE Transactions on Geoscience and Remote Sensing*, 22(6):592–597, November 1984.

[49] David C. Munson and R.L. Visentin. A Signal Processing View of Strip-Mapping Synthetic Aperture Radar. *IEEE Transactions on Acoustics, Speech, and Signal Processing*, 37, No. 12:2131–2147, December 1989.

[50] Chris Oliver and Shaun Quegan. *Understanding Synthetic Aperture Radar Images*. Artech House, Boston, 1998.

[51] R. Keith Raney, H. Runge, Richard Bamler, Ian G. Cumming, and Frank H. Wong. Precision SAR Processing Using Chirp Scaling. *IEEE Transactions on Geoscience and Remote Sensing*, 32(4):786–799, July 1994.

[52] R. Keith Raney and Paris W. Vachon. A Phase Preserving SAR Processor. In *Proceedings of the 1989 International Geoscience and Remote Sensing Symposium (IGARSS '89)*, pages 2588–2591, Vancouver, Canada, 1989.

[53] R.K. Raney. A New and Fundamental Fourier Transform Pair. In *Proceedings of the 1992 International Geoscience and Remote Sensing Symposium (IGARSS '92)*, pages 106–107, May 1992.

[54] F. Rocca, C. Cafforio, and C. Prati. Synthetic Aperture Radar: A New Application for Wave Equation Techniques. *Geophysical Prospecting*, 37(2):809–830, 1989.

[55] M. Sack, M.R. Ito, and I.G. Cumming. Application of Efficient Linear FM Matched Filtering Algorithms to Synthetic Aperture Radar Processing. *IEE Proceedings*, 132(1):45–57, February 1985.

[56] Gerald G. Schaber, John F. McCauley, Carol S. Breed, and Gary R. Olhoeft. Shuttle Imaging Radar: Physical Controls on Signal Penetration and Subsurface Scattering in the Eastern Sahara. *IEEE Transactions on Geoscience and Remote Sensing*, GE-24(4):603–623, July 1986.

[57] Gerald G. Schaber, Gary R. Olhoeft, and John F. McCauley. The "Radar Rivers" of the Eastern Sahara: Signal Penetration and Subsurface Scattering Observed by the Shuttle Imaging Radar. In *Proceedings of 3rd International Conference on GPR*, page 61, 1990.

[58] Merrill I. Skolnik. *Introduction to Radar Systems*. McGraw-Hill, Singapore, 1981.

[59] A.M. Smith. A New Approach to Range-Doppler SAR Processing. *International Journal of Remote Sensing*, 12(2):235–251, 1991.

[60] D.R. Stevens, I.G. Cumming, and A.L. Gray. Motion Compensation for Airborne Interferometric SAR. In *Proceedings of the 1994 International Geoscience and*

Remote Sensing Symposium (IGARSS '94), pages 1967–1970, Pasadena, USA, August 94.

[61] G.W. Stimson. *Introduction to Airborne Radar*. Hughes Aircraft Co., 1983.

[62] GEC-Marconi Defence Systems. Interface Control Document for the FIN3110 Master Instrumentation Port. Technical report, GEC-Marconi, Scotland, 1996.

[63] Yann Tremeac. An Example of Rapid Prototyping on the TMS320C80 - thesis under preparation. Master's thesis, Dept. Electrical Engineering, University of Cape Town, South Africa, 1999.

[64] F.T. Ulaby, R.K. Moore, and A.K. Fung. *Microwave Remote Sensing*, volume 2. Addison-Wesley, USA, 1982.

[65] M. R. Vant. Synthetic Aperture Radar Signal Processing. In *Proceedings of the 1989 International Conference on Radar*, April 1989.

[66] Terje Wahl and Age Skoelv. ERS-1 SAR Imaging of Ocean Features in the Vestfjorden Area. In *Proceedings of the 1994 International Geoscience and Remote Sensing Symposium (IGARSS '94)*, pages 2035–2037, Pasadena, USA, 1994.

[67] JoBea Way and Elizabeth Atwood Smith. The Evolution of Synthetic Aperture Radar Systems and their Progression to the EOS SAR. *IEEE Transactions on Geoscience and Remote Sensing*, 29(6):962–985, November 1991.

[68] C.A. Wiley. Pulse Doppler Radar Methods and Apparatus. Technical report, US Patent No. 3,196,436, 1954.

[69] Howard A. Zebker and Paul Rosen. On the Derivation of Coseismic Displacement Fields using Differential Radar Interferometry: the Landers Earthquake. In *Proceedings of the 1994 International Geoscience and Remote Sensing Symposium (IGARSS '94)*, pages 286–287, 1994.